Electronic Theses and Dissertations

Theses, Dissertations, and Major Papers

2005

Wear and scuffing resistances of eutectic aluminum-silicon alloys and aluminum-silicon based composites

Hongbo Wang
University of Windsor

NOTE TO USERS

This reproduction is the best copy available.

UMI®

WEAR AND SCUFFING RESISTANCES OF EUTECTIC Al-Si ALLOYS AND Al-Si BASED COMPOSITES

By

Hongbo Wang

A Thesis

Submitted to the Faculty of Graduate Studies and Research

through Engineering Materials

in Partial Fulfillment of the Requirements for

the Degree of Master of Applied Science at the

University of Windsor

Windsor, Ontario, Canada

2005

© 2005 Hongbo Wang

Canada

ABSTRACT

The existing information in the open literature suggests that the eutectic Al-Si alloy may be one of the best candidate materials for the sleeveless automotive engine block application. Dry sliding wear tests have been conducted using the block-on-ring wear machine on the near eutectic Al-Si alloys (13.2% Si) with the same chemical compositions, in which two were as-cast alloys had needle-shape Si particles, and the other two T6 heat treated alloys had round-shape Si particles. The T6 heat treatment has efficiently improved the hardness of the Al matrix, refined the Si particles in comparison to the as-cast alloys. The reciprocating wear tests were performed on the as-cast alloys and the T6 heat treated alloys at engine operating temperatures and lubricated conditions.

An systematic investigation of the effect of Si particle morphology and strength of Al matrix on the wear behaviour of the near eutectic alloys has been carried out using single pass scratch test supported by microhardness measurements, optical microscopy (OM), scanning electron microscopy (SEM), EDS and optical surface profilomety (Wyko) investigations.

The volume loss vs. sliding distance curves from the block-on-ring tests showed that the two T6 heat treated materials exhibited lower volume losses than the two as-cast alloys. Based on these initial tests, one material from each of these two groups (as-cast and heat treated) was selected as candidates for the further tests. Wear rate tests demonstrated that the T6 heat treated alloys had higher wear resistances than the as-cast alloys when tested against the AISI 52100 steel and the A40 cast iron ring counterfaces at all load levels and sliding velocities varying from 0.3 to 10 N and 0.2-2 m/s.

III

Results of experiments suggested that at low load levels (<2N), the hardness of the Al matrix was the main factor that controlled the sliding wear. Over 2 N load (2-10N), the Si particle morphology played an important role in terms of wear resistance. Si particle morphology controlled wear through counterface ploughing and different fracture behaviour. Needle-shaped particles ploughed counterface more severely than round-shaped Si particles. Round-shaped Si particles had higher fracture resistance than needle-shaped particles.

Reciprocating wear tests at the engine operating temperature and boundary lubrication condition have proven that the T6 heat treated alloys were superior to the as-cast alloy in terms of scuffing resistance.

IV

TO MY WIFE

XIULI GAO

AND

TO MY SON

MAX T.S. WANG

V

ACKNOWLEDGEMENTS

I would like to express my sincere gratitude to Dr. A. T. Alpas, (NSERC/General Motors of Canada Industrial Research Chair), for his excellent supervision, interests in these projects, encouragement for the research and friendship.

Dr. T. Perry is acknowledged for his comments, suggestions and most valuable technical support in the past two years. Dr. Y.T. Cheng is also acknowledged for his valuable suggestions and his efforts of making the facilities of General Motors Research and Development Center (Warren, Michigan) available for the tests.

I would like to extend my thanks to the group members, Dr. A. Edrisy, X. Nie, Mr. M. Elmadagli, , Mr. E. Konca, Mr. S. Akarca, Ms X. Song and Ms H. Yu in our group for their help and encouragement; Mr. J. Robinson's technical assistance and Ms. Q. Tu and Mrs. B. L. Denomey's administrative assistance during my graduate studies are also gratefully acknowledged.

The financial support from NSERC and the General Motors of Canada, and the recipence of an Ontario Graduate Scholarship was very much appreciated.

TABLE OF CONTENTS

VIII

IX

X

LIST OF TABLES

XI

LIST OF FIGURES

XII

XIII

XIV

XV

Average Si count number in one field in the alloys.

Aspect ration distribution of Si particles in the alloys.

Average aspect ratio of Si particles in the alloys.

A Vickers indentation impression on the surface of the A13-S sample.

A Vickers indentation impression on the surface of the A13-C-T6 sample

measured the bulk hardness at 1kg load.

A Knoop indentation impression on the surface of the A13-C-T6 sample

measured the matrix hardness at 10g load.

Bulk hardness of the alloys.

Al matrix hardness of the alloys.

Volume loss of the four materials vs. sliding distance at 1N load and 1m/s.

Wear rates vs. load at different sliding velocities.

XX

XXII

XXIII

XXV

CHAPTER 1

INTRODUCTION

Four-stroke compression-ignition and spark-ignition internal combustion engines are used in most automotive applications. Because engines must have compact, rigid structures, the engine blocks have been traditionally made from grey cast iron, and the pistons were made from aluminum alloys. In recent years, in order to reduce the weight and increase the efficiency of the engines, various Aluminum-Silicon alloys and their composites have been developed to replace the heavy cast iron engine block.

Previous research suggested that aluminum alloys and their composites are promising lightweight tribological materials for sliding wear resistant applications in automotive engines [1-3]. Because silicon improves castability and strength-to-weight ratio and corrosion resistance, it also reduces the coefficient of thermal expansion, aluminum-silicon alloys are widely used as bearing and piston materials in the automotive industry [3]. In 1970, General Motors introduced a Chevrolet 2.3 1 l-4 Vega engine, with a die cast hypereutectic aluminum-silicon alloy cylinder block without cylinder sleeves [2]. Similar sleeveless aluminum engine blocks have also been used by European and Japanese automakers [2]. Si content in tribological materials may vary from 6% to as high as 20%. However, this effort did not cease the common use of cast-in cast iron liners due to the concern of premature wear, scuffing

1

and seizure problems that may occur during lubricant starvation periods [4]. Hence studying of dry sliding wear of Al-Si alloys is important.

Aluminum matrix composites incorporating ceramic particles or/and graphite phase into the alloys can further increase the wear and scuffing resistance under dry sliding conditions [5]. A metal matrix composite (MMC) may be defined as a material consisting of a metal phase into a second phase [5]. The second phase material is often a ceramic such as a metal carbide (SiC) or oxide (Al_2O_3). The reinforcing phase may take the form of particles, whiskers, short fibres or continuous fibres. Graphite particles are sometimes used as second phase particles to provide solid lubrication.

The automotive industry has been very interested in the aluminum-silicon alloys as by far they are still the most reliable lightweight engine grade materials that can replace cast iron liners. Many researchers have been working on these difficulties. A few years ago INCO Canada developed a new serial of Al-Si composites reinforced by low content of aluminum oxide particles and graphite particles as engine bore materials. General Motors recently developed a novel group of near eutectic Al-Si alloys (13% Si).

This thesis is divided into four main chapters. Firstly the relative literature regarding sliding wear and materials for applications is reviewed. It is followed by the experimental procedures and the two parts of experimental sections. The two experimental sections include experimental results and discussions. Chapter 4 reports results of the investigation on a near eutectic aluminum-silicon alloys developed by

2

General Motors. It is mainly aimed at three points: i) to characterize the properties and microstructures of the new material systems; ii) to evaluate wear resistances of the Al-Si alloys and to optimize potential material(s) for engine bore application; and iii) to reveal role of Si particle morphology and strength of Al matrix in wear. Chapter 5 is to examine scuffing resistances of a group of new hybrid composite materials consisting of an A356 Al alloy matrix reinforced with various vol.% Al_2O_3 and graphite particles, and different particles morphologies using a reciprocating wear machine under boundary lubrication, automotive engine operating temperatures and stepwise loading conditions. Scuffing tests on the Al-Si eutectic alloys are also discussed in this chapter in comparison with the composites.

3

CHAPTER 2

LITERATURE REVIEW

2.1 Sliding Wear

Tribology (wear, friction and lubrication) is a one of the main branches of science and technology associated with the failure of mechanical systems. Wear may be appropriately defined as "damage to a solid surface, generally involving progressive loss of material, which is due to relative motion between that surface and a contacting substance or substances" [8]. Interest in the materials aspects of tribology has grown drastically in the last two decades, and this has been accompanied by many new ideas and observations in order to reveal and rationalize the wear mechanism and the factors that control the wear processes at the microstructural level. Researchers have attempted to classify the various types of wear into different categories.

Abrasive wear is the removal or displacement of material from one surface by loose hard particles or by the asperities of another surface [9]. The mechanisms may involve microcutting or plastic deformation accompanied by frictional heating of surfaces of ductile materials or brittle fracture of ceramics or hard surfaces [10].

During sliding contact, repeated application of stress resulting in accumulation of damage in the subsurface can lead to delamination wear [11]. In ductile materials

4

delamination may become a dominant wear mechanism in materials containing second phase particles.

Corrosion processes, including oxidational wear, involve the synergistic effect of mechanical wear and chemical reaction [12]. References 13 and 14 reviewed the theory of oxidational wear. Corrosion processes are found in many instances of wear under normal service conditions.

Adhesion involves the interaction of asperities on the sliding surface. The asperities meet and briefly weld together forming a junction, which is subsequently fractured. A critical review of the adhesive wear process can be found in reference15. This process often leads to material transfer from soft to hard counterface.

There are other processes including fretting, erosion, polishing wear and impact wear. In fact these processes occur simultaneously in almost every operating tribological system [9].

Whenever there is a relative motion between two contacting solid bodies, there is a potential for sliding wear to occur [11]. Sliding wear can be classified into two categories: dry sliding wear and lubricated wear. If liquid or solid lubricant is present in the sliding interfaces, it is termed as lubricated sliding wear. Dry sliding wear refers to the absence of lubricants in the sliding interfaces, such as the case of cold scuffing in the automotive engines. Mild wear and severe wear are frequently used to describe the extent of the sliding wear. When the sliding surface damage is less extensive and tribological layers cover the worn surfaces, it is called mild wear [15]. Severe wear

5

involves massive surface damage and large scale materials flake away or transfer to the counterface [15]. Wear maps are effective tools for the wear investigation. Wear map is a calculated or experimentally determined diagram that identifies regions where the wear mechanism or wear rate remains substantially the same [8]. The regions are separated by transition lines or bands that are functions of two or more parameters such as load, speed, temperature or environment. The commonly used wear maps are of two types: *wear mechanism maps* or *wear rate maps* [8]. The first identifies specific regions within which a particular wear mechanism controls the wear rates (such as oxidation or delamination). The transition region to another wear regime may or may not involve a step change in wear rate. The second type of wear map identifies regions of constant wear rate, wherein it is to be understood that transition should involve a change in wear rate of generally at least a factor of ten.

Various wear set-ups have been developed for tribology research purposes. Pin-on-disk (Fig 2.1a), block-on-ring (Fig 2.1b), and reciprocating wear machine (Fig 2.1c) are commonly used in laboratory [16].

2.2 Friction and Coefficient of Friction

As mentioned in Section 2.1, when two surfaces in contact slide over each other, one or both of the surfaces are likely to suffer from wear. The contact between the two surfaces occurs through the asperities touching rather than the two bulk surfaces touching (Fig.2.2) [17]. Friction is the resistance to relative motion of contacting

6

bodies. The degree of the resistance to motion is expressed as a "coefficient of friction" (COF), μ,

$$\mu = F_N / F_T \hspace{6cm} 2.1$$

where F_N is the normal applied load and F_T is the tangential force required to sustain sliding.

The value of the coefficient of friction is determined by the sum of the individual contributions of the principle friction components [18, 19], namely, adhesion (μ_a), ploughing (μ_p) and deformation (μ_d). Hence,

$$\mu = f_a\, \mu_a + f_p\, \mu_p + f_d\, \mu_d \hspace{5cm} 2.2$$

where the coefficients f_a, f_p, and f_d indicate the relative contribution of each component. The actual values of the contributions are determined by the characteristics of the wear mechanisms that take place, which are a function of material properties, environment and testing conditions.

An increase in the COF is the most direct indicator to the occurrence of wear. In the beginning of a sliding motion, significant friction occurs between the two contacting surfaces if the surfaces do not conform with each other. The high rate of wear rapidly lead to smooth contacting geometry by removing (hard) and/or

7

deforming (soft) sliding motion blocks, i.e. asperities. When the good conformation of the two sliding surfaces is obtained, mild wear occurs accompanyed by a low wear rate and a low COF. Eventually, the combined effects of the sliding shear, temperature, and material properties lead to the occurrence of the transition to severe wear, where COF drastically increases.

2.3 Factors That Influence on Wear Rates

2.3.1 Applied Load: Archard Wear Equation

The wear process involves very many variables. The wear rate, W, of a sliding surface is a function of the applied normal force, P, which acts across the two contact surfaces, the relative velocity, v, the initial, T_o, and the thermal, mechanical and chemical properties of the contacting materials. Such wear rates can be described as follows [20]:

$$W_i = f_i\{P, v, T_o, \text{thermal, mechanical props.}\} \qquad\qquad 2.3$$

Load is usually regarded as the most dominant factor to govern the wear process. Wear equations that can be found in the literature attempt to model the effect of normal applied force on wear, but none has general application [21]. The most widely cited equation is the Archard Equation, in which the rate of wear, V, is:

8

$$V = K\frac{P}{H}$$
2.4

V is the volume removed per unit sliding distance. P is the applied load in Newtons, H is the hardness of the softer surface in Newtons per unit area. K is the dimensionless wear coefficient, and always less than unity. Hutchings [22] pointed out that K could be defined in terms of the probability of each asperity interaction resulting in the production of a wear particle. P/H may represent the real area of contact for fully plastic asperities. At this point, K can be interpreted as the ratio between the apparent area and the real contact area.

From this equation, the wear rate is independent of the apparent contact area, and is applied to both mild and severe wear regimes. However, this assumption was not supported in practice [22]. This is explained by the effect of the load-dependent temperature generated by friction. When the wear rate is plotted against the load, the speed for each load being chosen to give the same surface temperature, then proportionality is obtained. A further qualification was given by Archard: "with the same surface condition, the wear rate is proportional to the load". Clearly, load can not solely govern the real wearing process. Other factors must be considered.

2.3.2 Temperature

In a sliding wear system, most of the work done is turned into heat. The rise in temperature may modify the mechanical and metallurgical properties of the sliding surfaces. Generally, strength decreases and ductility increases with increasing the test

9

temperature. This general behaviour, however, can be altered by structural changes resulting from such as precipitation, strain aging, or recrystallization that may occur in certain temperature ranges [23]. According to Deter [23], for the bcc metals the yield stress increases rapidly with decreasing temperature, whereas for fcc metals the yield stress and the flow stress are not strongly temperature-dependent but the strain-hardening exponent (m) decreases with increasing temperature. On the other hand, the tensile strength is more temperature-dependent than the yield strength.

More than 90% of the energy expended in plastic deformation is converted to heat. In localized deformation the temperature rises within this local region. Further deformation is concentrated preferentially in this zone and may continue until fracture occurs. At high rates of deformation there is no time for appreciable heat to flow to occur and a near adiabatic condition results. Surfaces become severely deformed or oxidized or even melt; all these factors influence the rate of wear, and control the transition to severe wear through the frictional heat [24-28].

The increase of the surface temperature affects the flow properties of the two contacting surfaces. Consequently, the wear process is influenced by the surface temperature. Zhang and Alpas [22] studied the effect of surface temperature on wear mechanisms by investigating a wrought aluminium alloy 6061Al with SAE 52100 steel as its counterface. Experimental results in Fig.2.3 showed the change in the bulk surface temperature of 6061Al with the sliding time, and distance under different applied loads. In the mild wear regime at a combination of low loads and velocities,

10

an initial temperature increase followed by a settling down to a steady value for the rest of the experiment. At the combination of high test speeds and loads, the surface temperature continuously increases at a high rate up to seizure. These suggested that attainment of a critical transition temperature triggered the occurrence of the wear transition. It was also found the transition to severe wear could be delayed or even eliminated by depressing the temperature of the wear couple under the transition temperature (Fig. 2.4) [22]. Similar results were obtained by Hirst and Lancaster [17].

2.3.3 Sliding Speed

The sliding speed is another variable that influences the wear rate. In the mild wear regime, the wear rate decreased with increasing speed and reached a minimum at a certain speed. Thereafter, wear rate started to increase again [22]. Hirst and Lancaster found that the mechanism of the severe wear is not affected by speed [29]. The down- and up- trend is caused by a competition of frictional heat softening and strain hardening. The up-trend can be suppressed by force-cooling the surface [22, 29]. The tendency to decrease wear rate with speed is limited by the attainment of a critical temperature rather than a critical speed [22, 29].

2.3.4 Formation of Tribo-layers

Testing in air is very different than testing in vacuum [30]. In vacuum, the COF is usually much higher than it is in air [31]. In air, the surfaces are normally contaminated with a layer of absorbed gases, hydrocarbons and moisture [31]. Below this layer, in metals, there is a reaction zone, typical elements from the two mating

11

materials, their metal oxidants or sulfide and/or intermetallic, whose thickness is only of the order of 10 nm thick [11, 22-29]. In lubricated condition, certain organic elements may be involved in the mixture, which will be reviewed later. These layers could be termed as tribo-layers. Below the tribo-layer there is a layer of deformed material generated during wear. The thickness of this layer depends on the load, speed and temperature. Underlying this is the bulk material. When the two sliding surfaces contact together, the tribo-layer prevent metal to metal contact [9]. One of the factors affecting the properties of this tribo layer is the atmospheric humidity in sliding wear. A critical review of the influence of environmental humidity on the friction, lubrication and wear of materials can be found in [30].

In a tribo-system, the tribo-layer cannot be produced until at least one performance of a sliding motion. After an initial sliding, the tribo-layers first appear at the contacting asperities, and continue to grow and expand to the whole real contact areas up to the occurrence of seizure [35]. A negative aspect of the tribo-layers was the scuffing damage on the counterface. The hard fractured debris detached from the layers could act as two- or three – body abrasives and micro-cut the counterface [35].

2.3.5 Lubrication Regimes

When a wear process occurs in a lubricated condition, either in liquid state (oil), or solid state (graphite), it is called lubricated wear. The presence of lubrication film reduces the frictional coefficient. As a result, it significantly affects the magnitude and

12

the distribution of shear stress, the frictional heating process, and the formation of tribo-layers.

According to Cheng [36], there are three kinds of lubrication films: (1) Thick films. A thick film refers to the total separation of asperities by a film which thickness is much larger than the size of the asperities; (2) Thin films. They refer to the situation in which part of the load is carried by the fluid pressure and the rest is carried by contacting asperities; (3) Boundary films. In the most severe form of thin-film lubrication, the entire load is carried by asperities lubricated by molecularly thin lubricant films.

Hydrodynamic lubrication refers to a pressurized film generated by high surface sliding velocity. The effectiveness of such thick film lubrication depends directly on relative speed and lubricant viscosity. Lubricant film thickness is important in hydrodynamic lubrication for designing against possible solid-to-solid contact. Temperature significantly affects hydrodynamic lubrication by reducing lubricant viscosity and film thickness.

Boundary lubrication results from low sliding speed, low viscosity, and very high load, the frication coefficient solely depends on the extreme contacting surface profile, the load is totally carried by the asperities lubricated by molecularly film [36]. In boundary lubrication regime, the tribo-layer consists of three films: physically adsorbed, chemically adsorbed, and chemically reacted surface films. Adsorbed films are monomolecular and the thicknesses are in the range of manometers. Reactive

13

films are usually stable and durable thick films. They are enhanced by the sulphides, chlorides, or phosphates generated by the reaction of lubricant additives and surface materials. These films provide effective protection for the sliding asperities under extreme conditions.

2.3.6 Material Variables

Material variables are very important in wear. Microstructural properties such as compositions, grain size, number of phases, phase distribution, anisotropy as well as mechanical properties such as strength, hardness and ductility of both mating pairs affects the wear behaviour [37]. For instance, the presence of a second phase particle may lead to a reduction in the real area of contact, an increase in the load carrying ability or change the operating mechanism all together [38]. This also led to a new group of tribological materials- metal-base particle or fibre reinforced composites. The distribution of the phases and any anisotropy in the material will affect the response of the material to the applied load. A change in any one factor may result in a change in a related factor. For example, decreasing the grain size increases the strength and hardness of a metal which suggests an increase in the wear [39-43].

2.4 Scuffing

At the present of lubrication film, scuffing is the main surface-damage behavior. Liquid lubricants serve three functions: (a) distribute some or the entire contact load over the entire nominal area; (b) reduce asperity heating; (c) remove heat from the deformed or heated regions. When the thickness of the fluid film is greater than the

14

height if the asperities, the system is in hydro-elastic sliding motion. No scuffing occurs. However, when the lubricant film is broken up, and two solid surfaces directly slid against each other, scuffing occurs [44].

The scuffing is defined as "a roughening of surfaces by plastic flow whether or not there is material loss or transfer" [8]. Scuffing is not limited to high severity of damage or severe wear loss. It is a gradually progressing process starting with the scale of one single asperity then extending to any point of macroscopic manifestation up to seizure occurring [44]. The scuffing does not initiate from adhering but is assumed to begin by the plastic flow of one asperity. The plastic flow of asperities is induced by a combination of normal and tractive stresses. Scuffing then progresses by continuous and repeatable plastic flow of some asperities. The small debris agglomerate and grow to larger particles accompanying a repeated deformation and work hardening. Eventually, a mature particle suffers most of the applied load so it produces enough high contact stress to break up the fluid film lubrication. Temperature abruptly rises up to chemically alter any remained oil film between the interfaces, and welding or adhesion occurs. The above process self-amplifies with the sliding motion progression up to seizure [35, 44].

Scuffing and its prevention depends on the duration of the wear system, the materials, the surface preparation and the lubricants used in the system [44]. Surface roughness is not the only factor to affect the scuffing in surface profile aspects. The three-dimensional topography, residual stress and phase distribution also play

15

important roles in scuffing process. And the last one maybe attributes as important as the roughness [35]. Prevention of scuffing in automotive engines made of aluminum-silicon alloys is one of the aims of this thesis.

2.5 Lubricated Wear in Engine Bore System

Lubricated wear typically takes place in engine bore, piston and ring system. There are three important wear mechanisms in this system: corrosion, abrasion, and adhesion [45]. Corrosion has been successfully reduced by the use of thermostats and by the addition of corrosion inhibitors to engine oils. Abrasion results from the cutting and ploughing action of hard particles, and it has been solved by regular replacement of oil filters and air filters. Adhesion is usually results from metal-to metal contact when the oil film between the ring and bore is too thin. Once run-in is completed, adhesion should only happen where oil film thickness is less than the roughness of the surfaces. This only occurs near the top-dead-center and the bottom-dead-center, where ring velocity reaches zero [45, 46]. Hence it is important that the two contacting piston ring and liner materials are compatible in terms of adhesive wear. Differences in hardness between the two materials also need to be carefully watched in order to minimize the abrasive wear.

Piston rings are mechanical devices for sealing pistons, piston plungers, reciprocating rods, and so forth. Piston rings are usually made of gray cast iron rings, with a hardness ranging from 300 to 400 HB and higher levels of chromium and

16

molybdenum (1%) to give more ductility. Steel rings with chromium coating are also used for heavy duty automotive engine [47].

The cylinder walls are stressed mechanically by high gas pressure and the side thrust of the piston at high velocity, as well as thermally by the high gas temperature. For instance, in the Saturn engine, the peak cylinder pressure is 6200kPa. If this pressure is assumed to be acting on the inner diameter of the top compression ring, the force per unit length of the ring against the cylinder can be estimated at 7.4N/mm. In an engine idling at 900rpm, the average speed of the ring is around 2.4m/s, and at 4800 rpm, the speed is 12.8m/s. However, the speed at the ends of each stroke, where contact condition are the most severe, is zero [2]. Thus, the cylinder liner materials must have good mechanical and fatigue strengths and wear and scuffing resistance. Otherwise, cylinder bore distortion or early material fatigue failure may result [47].

Traditionally, cylinder liners are made of grey cast iron, which is heavy and has a low power-to-weight ratio. To increase their mechanical strength, additions of nickel, chromium, copper, and molybdenum are required. Steel cylinder liners also have been used, offering the advantage of much thinner walls. However, they must be hardened to at least 400 HB for satisfactory resistance to wear and scuffing, or else chromium plating has to be applied [45].

Aluminium-based alloys and composites are clearly attractive alternatives to iron-based ones as they provide high strength-weight ratio. Moreover, they can eliminate

17

the thermal expansion-induced separating problem between cast iron liners and Al-Si engine blocks [48].

2.6 Wear of Al-Si Alloys

2.6.1 Wear regimes of Al-Si Alloys

Al-Si alloys typically demonstrated two wear regimes: mild and severe [3, 49]. In each regime the wear rate increases with load. Oxidation and delamination occurred in mild wear [3, 51-53]. In the oxidative wear, the worn surface is covered with a layer of aluminum oxide or mixed oxide and metal [3]. Wear limits to the oxide layer only through a spallation process. In the delamination wear approach subsurface cracks nucleate at the Al-Si interfaces and propagate parallel to the worn surface at a depth of 10 to 20 μm [51]. With increasing the load, and therefore, the hydrostatic pressure, the rate of void growth decreases but the depth of crack initiation increases resulting in thicker debris.

Severe wear occurs at high load levels and is accompanied by gross plastic deformation, substantial material transfer and flake-like debris. The transition load to severe wear increases with increasing silicon content [3, 54]. At this stage, transfer from the aluminum sample has resulted in a system in which aluminum slide upon aluminum, consequently, leading to very high wear rates.

2.6.2 Subsurface Zones in Worn Al-Si Alloys

Three subsurface zones were observed during sliding wear [54, 55]. At the worn surface there is a mechanically mixed layer of finely fractured Si particles, Al, Fe,

18

intermetallic particles and oxide exists [55, 56]. Underneath is a region of plastically deformed zone where silicon fracture decreases with the increase of the depth. Below this is the unaffected bulk material.

2.6.3 Effect of Si Particle Volume Fraction on Wear of Al-Si Alloys

The Al-Si alloy system has a eutectic point at 12.6% (weight) Si. Hypoeutectic, eutectic, and hypereutectic of these alloys (Fig. 2.6) within the Si ranging from 6 to 24% have been extensively studied and yielded very different results. The lowest wear rate (Fig. 2.7) has been observed by many researchers at eutectic composition [57-59]. Other investigations [3] showed that eutectic Si composition yielded higher wear rate (Figure 2.8). Another investigation [60] concluded that the Si content ranging from 4 to 24% did not influence the wear rate in any detectable trend. However, wear resistance is improved in mild wear conditions with increasing the Si content (Fig. 2.9) is commonly accepted regardless of the above contradictory results [61]. As high silicon content may increase the wear of counterface materials, a compromised Si range from eutectic to lower hypereutectic compositions may be beneficial to the tribological system.

2.6.4 Effect of Si particle Size on Wear of Al-Si Alloys

Effects of Si particle size on wear have also been studied. The results showed that considerable differences in Si particle size do not significantly influence the wear rates [3] as the Si content, while influences of other factors such as Si particle morphology and Al matrix hardness on wear are hardly found in any literatures.

19

2.7 Wear of Al Matrix Based Composites

Aluminum matrix composites exhibit the ability to withstand high tensile and compressive stresses by the transfer and distribution of the applied load from the matrix materials to the hard reinforcement phase [51, 62]. Al-base composites are fabricated by the addition of a reinforcement phase to the Al matrix using powder metallurgy, liquid metallurgy and squeeze-casting [51]. The reinforcement phase is generally either continuous boron or graphite fibres, or hard particles such as SiC and Al_2O_3, or soft particle such as graphite particle severing as solid lubricant. The volume fraction of reinforced phase is generally within the range 10-30%. Considering the cost and difficulties in manufacturing processes, particle-reinforced composites are becoming increasingly utilized.

Aluminum alloys such as 2000, 5000, 6000 and 7000 alloy series are the most commonly used materials in composite fabrication. Aluminum composites are widely employed in the aerospace industry [63, 64]. Hypoeutectic Al-Si based composites such as A356 that contain Al_2O_3, ZrO_2 or SiC particles have been used in automotive application [65, 66].

When load increases, the composites appeared three wear behaviors [65, 67]. At low loads, the particles are able to support the load and machine the counterface resulting in a decrease in wear in comparison with the unreinforced alloy [62, 65, 67]. As load increases the particles fracture and lose their load bearing ability. Subsurface crack nucleation and growth occurs through a damage accumulation process leading

20

to wear rates similar to the unreinforced alloy. The transition load to severe wear is increased to higher level by reinforcements [67.68]. Like unreinforced Al-Si alloys, Transitions in wear rates or wear mechanism may be caused by changes in velocity [69]. Severe wear is terminated by seizure.

When the soft graphite particles are sheared and form a graphite film on the contacting surfaces, the coefficient of friction decreases [70]. When the graphite content is less than 20%, the coefficient of friction depends on the matrix composition [70]. Too high content of graphite particles, on the other hand, may overshadow the beneficial of lubricating film formation. A reduction in wear resistance due to the less strength and ductility has been reported [71]. High content of graphite addition yields porosity in metallurgical manufacturing, which also increases wear rates [72].

2.8 Summary of the Review and Objectives of The Thesis

Based on the above review, we may conclude that the wear and scuffing resistance of the Al-Si alloys is a function of the applied load, the sliding speed, the surface temperature and the ambient conditions. The silicon content plays key role in wear of Al-Si alloys. However, investigations on the effect of silicon particle morphology on wear are very limited. The effect of the Al matrix hardness was not found in the opening literature.

The objective of this work is mainly in two fold: 1) to reveal the effect of the silicon particle morphology on wear of Al-Si alloys; 2) to investigate the effect of aluminum matrix hardness on wear of Al-Si alloys

21

CHAPTER 3

MATERIALS AND EXPERIMENTAL METHODS

In this chapter, the experimental procedures used for the investigations of the relationships between the microstructures and wear resistances of the cast Al-Si alloys (with near eutectic compositions) are described. In addition to the cast Al-Si alloys, the Al-Si based ceramic particle reinforced composites were also tested. To measure their scuffing resistance, lubricated reciprocating wear tests were performed on both of the Al-Si alloys and the composites. To determine the wear resistance of the Al-Si alloys, unlubricated sliding wear tests and single pass scratch tests were conducted on the Al-Si alloys. Details of sliding wear tests (reciprocating and unindirectional block-on-ring), and single pass scratch tests are explained in this chapter. Analytical methods that were employed to characterize microstructures, morphologies and compositions of the worn surfaces and the loose debris are also described. These methods included scanning electron microscopy (SEM) with energy dispersive spectroscopy (EDS), optical microscope (OM), and optical surface profilomety (Wyko). As the aluminum alloys encompass a wide range of chemical compositions and second phase particles and thus a wide range of hardnesses, good care had to be taken in the metallographic preparation of samples. These methods are discribed in the last section of this chapter.

22

The cast Al-Si alloys used in the experiments were provided by General Motors Research & Development Center, Warren Michigan. The Al-Si based composites were provided by INCO. Ltd., Mississauga, Canada. The Al-Si samples were cut from the engine blocks in to 120 mm x 12mm x 5mm specimens using EDM in the companies that supplied them.

3.1 Experimental Methods Used for Al-Si Alloys

3.1.1 Description of Wear Tests and Test Samples

The samples for sliding wear tests consisted of four types of near eutectic Al-Si alloys with the same nominal chemical composition in weight percent of 13.2 Si, 2.3 Cu, 0.34 Mg, 0.13 Fe, 0.01 Ni, 0.32 Mn, 0.01 Zn, 0.017 Sr, 0.01 Ti and the balance Al. The samples were fabricated in the General Motors Research and Development Foundry (Warren, Michigan) using a sand casting process in three different moulds. These alloys are designated as GM 396 Al-Si alloys. The casting methods consisted of silica-sand mould, zircon-sand mould and chilled mould. One set of silica-sand cast samples and one set of chilled cast samples were then solution treated and artificially aged in order to modify the Si particle morphology and strengthen the Al matrix through the precipitation hardening. The GM 396 alloys produced in different ways were designated by General Motors as follows: 1758-S (silica-sand cast), 1758-Z (Zircon-sand cast), 39-7 (Chilled cast + T6 heat treated) and 40-7 (silica-sand cast + T6 heat treated). In this thesis, they are referred as Al 13-S (silica-sand cast), Al 13-Z (zircon-sand cast), Al 13-S-T6 (silica-sand cast + T6 heat treated) and Al 13-C-T6

23

(chilled cast + T6 heat treated). The aluminum blocks were cut in the form of 120mm

x 12mm x 5 mm coupons using a wire electric discharge machine (EDM).

To study the role of Al matrix hardness on the wear resistance, the T6 heat treated

alloy coupons were annealed at 350 °C for 10 minutes and furnace cooled to room

temperature to reduce the matrix hardness. This created an alloy with similar matrix

hardness to that of the as silica-sand-cast alloy (A13-S), but with similar Si particle

size and morphology. In this thesis this alloy was referred as Al 13-S-T6-AN.

Detailed characterization of the microstructures of the Al-Si alloys will be given in

Chapter 4. The chemical compositions and the processing methods of the Al-Si alloys

are summarized in Table 3.1 and Table 3.2, respectively.

To make a comparison with the cast alloys, a wrought aluminum alloy namely

6061 Al with chemical compositions in weight percent of 0.4-0.8 Si, 0.2-0.4 Cu, 0.8-

1.2 Mg (and the balance Al) was used. To reduce the hardness of the samples and to

eliminate the grain orientation due to extrusion, the 6061 Al samples were annealed at

415 °C for 1 hour then furnace cooled to the room temperature. The microstructural

characteristics of 6061 Al are shown in Chapter 4.

To measure the wear rates of the Al-Si alloys, dry sliding wear tests were

conducted using a block-on-ring wear machine (Figure 3.1a). The machine consists of

a sample holder above a rotating ring, on which the counterface was inserted (Figure

3.1b). The loads were applied using dead weights placed over the sample holder. A

one horsepower DC motor (1750 rpm max) was used to drive the shaft connected to

24

the rotating ring. The applied normal load varied between 0.3 N and 10 N. In most tests, the sliding speed was kept constant at 1m/s. To study the effect of the test speed on the wear rate, two other test speeds of 0.2m/s and 2m/s were also used. For all the tests, the sliding distance was fixed at 6×10^6 m. This distance was calculated using the sliding speed and the duration of each test. Tests were conducted under ambient conditions with a relative humidity of 30-35%.

The counterface steel ring was made of AISI 52100 steel with a composition of 1% C, 0.35% Mn, 1.45% Cr, 0.25% Si, 0.04% (max) S, 0.035% (max) P, and the balance Fe. The outside diameter of the ring was 30 mm and its width was 12mm. The ring was treated to have a surface hardness of 60 HRC (900 HV). To study the effect of counterface materials on the wear of the samples, A40 grey cast iron rings (microhardness 300 HV) with the same configuration and dimension as the 52100 steel rings were also used. Prior to each test, the ring surfaces were polished with 180 and 400 grit SiC grinding papers. The microstructures of the 52100 steel and A40 cast iron are shown in Chapter 4.

The wear test samples were cut into rectangular blocks of 10 x 10 x 4 mm in size using a low speed saw (Buehler ISOMET). The specimen and saw blade were kept at room temperature during cutting using a liquid coolant (Varsol dilute solution). The narrow face of each sample was then polished with 400 and 600 grit SiC grinding paper along the direction, which was vertical to the sliding direction. The samples and the counterface rings were then ultrasonically washed in acetone and dried using hot

25

air. The weight of each sample was measured using an electronic balance (Scientch SA120) with a sensitivity of ±0.0001g before and after each test. The wear rate was determined as volume loss per unit sliding distance (mm^3/m). The volume loss was calculated using the mass difference of each sample before and after the wear test divided by its density.

3.1.2 Single Pass Scratch Tests

To study the fracture behaviour of Si particles and the role of the matrix material on the wear of Al-Si alloys, single-pass scratch tests were conducted using a scratch tester (Figure 3.2). The sample holder freely moves in one direction on the rail track. The sliding motion is generated using a motor driven cart, on which the sample holder track is mounted. Load is applied on the indenter by the loading mechanism of the microhardness tester. The tangential resistance force generated during scratching was measured using a piezo electric load cell (Omegadyne LCKD-5 with accuracy of 0.25%,) mounted in front of the freely movable sample holder. The data is recorded by a Lab View Software. The friction force is then plotted as a function of distance.

The specimens were cut into rectangular blocks of 10mm x 50mm x 4mm. One of the large faces (50 mm x 10 mm) of each sample was then polished by 180, 400, 600, 1200 grit silicon carbide grinding papers, and polished by clothes (LECO) impregnated with 1 and ¼ µm diamond suspension solution. After cleaning, the polished surface was etched by 10% (wt) NaOH solution for 2 minutes followed by immersing them in a 50% HNO_3 solution for 10 seconds. This procedure caused the

26

Si particles stand proud of the alloy's contact surface. In the open literature, it was reported that this etching technique successfully increased the wear resistance of the Al-Si alloys [76]. The etched surface was then rinsed by tap water and acetone. The scratch indenter was a 2 mm diameter ball made of AISI 52100 steel with a microhardness of 875 ± 50 HV. Prior to each test, the spherical indenter was polished by 600 and 1200 grit grinding paper and ultrasonically cleaned in acetone for 2 minutes. In lubricated scratch test, the sample surface was fully covered by the SAE 10W-30 engine oil. Dry scratch tests were conducted at 0.5N and lubricated tests were done at 5N load. After the load was fully applied on the sample through the counterface, the spherical indenter moved at a constant speed of 12mm/min for a total distance of 15 mm.

A wrought Al alloy, namely, 6061 (without Si particles) annealed at 415 °C for 10 minutes was also used in the scratch tests for comparison of the effect of Si particles in the cast Al-Si alloys. Etching was not applied to 6061 Al specimens due to the absence of the Si particles in the Al matrix. The annealed 6061 Al alloy had a hardness similar to the silica-sand cast Al-Si alloy (A13-S).

After testing, the dry test specimens were ultrasonically cleaned in acetone. The lubricated tested specimens were ultrasonically cleaned in 99.55% trichlorethylene for 10 minutes. Then samples were immersed into the fresh trichloroethylene for at least 2 hours to remove the oil penetrated inside the specimens.

27

3.1.3 Reciprocating Lubricated Wear Tests

To study the wear behaviour of the Al-Si alloys under lubricated condition, reciprocating wear tests were conducted on A13-S and A13-C-T6 alloys using a ball-on-flat configuration. To simulate the engine operating condition, a high temperature reciprocating sliding wear tester was utilized and shown in Fig 3.3. The counterface holder was attached to a balanced dual cam arrangement that was driven by a computer-controlled motor to provide the reciprocating motion with 108 mm stroke. The cylinder liner specimen holder was located on a vertically adjustable loading block. The specimen and the counterface were tightened to the corresponding holders. During tests, the sample was pressed against the counterface through a loading arm arrangement underneath the holder (Figure 3.3). The liner sample was heated using a cartridge heater inserted under the liner holder. The temperature was kept at 150 °C and was measured by a thermocouple in a hole that was drilled to the liner holder. The tip of the thermocouple was located 2 mm below the center of the samples. The lubricant oil was supplied at a constant rate of 0.1ml/min to the sample surface through a tube connected to a reservoir that was placed above the machine.

The samples were cut by EDM into 120 mm x 12mm x 4 mm test coupons. One of the largest faces of the coupons was polished and etched by 10% NaOH solution for 2 minutes and then immersed the samples into a 50% HNO_3 solution for 10 seconds. The counterface used in this test was 14.3mm diameter AISI 52100 steel ball.

28

The load used in the ball-on-flat test was 1.2N. The load was applied to the sample through a loading arm. A plastic tube was used to reduce the vibration of the load. The machine was run at a speed of 200 rpm. The sliding distance was 2160 m. The temperature of the specimen was kept at 150 °C during tests.

3.2 Determination of Scuffing of Al-Si Eutectic Alloys and Al-Si Based Graphitic Al_2O_3 Composites

Step loading tests were performed using the same reciprocating wear machine described in section 3.1.4. The test materials were A13-C-T6 alloy, A13-S alloy, and the composites made of an A356Al-Si alloy reinforced by 0, 3, 5 vol. % of Al_2O_3 and graphite particles. The compositions of the composites and the SEM microstructures are shown in Chapter 5. The contact of the aluminum-silicon alloy specimen and the counterface were roll-on flat configuration. The aluminum silicon alloy specimens were cut from the castings into flat blocks of 120 mm x 12 mm x 4 mm. The counterface of the alloys were 5 mm diameter M2 steel rollers with a length of 7 mm. The two sides of the rollers were flattened into 2.5 mm to make it fit on the width of the counterface holder (Figure 3.4) The composite specimens were cut longitudinally from the honed cylinder liners by approximately 120 mm (in length) x 12 mm (inside cord length) x 5 mm (thickness). The counterface rings were cut into 9 mm in outside cord diameter from a specific section of the CrN coated steel piston rings to achieve the conformable contact with liner specimens (Figure 3.5).

29

An approach consisting of stepwise increase of applied load was used to observe the onset of the scuffing at a certain load level, which depended on the material tested. During the test, SAE 10W-30 engine oil was supplied at a constant rate of 3 drops per minute (0.01ml/min) on the entire liner sample surface. An initial run-in period during which a sliding velocity of 100rpm (0.36m/s average linear speed) and 30N load was applied for 10 minutes. The purpose of this process was to obtain a conforming contact condition between the counterface and the specimen. After the run-in period, the sliding velocity was increased to 200 rpm, and the specimen temperature was kept at 150 °C. The load was increased by steps of 30N in 3-minute intervals up to 270N. Above 270N, each load step was decreased to 10 N until the onset of scuffing was observed. The scuffing was identified by the immediate change of the specimen surface such as excessive scratching and increase in the levels of vibration of the test machine.

After the scuffing test, the scuffed specimens were metallographically prepared using the same procedure described in section 3.1.2.

3.3 Metallographic Sample Preparation and Observations

All samples were sectioned using low speed saw (Buehler, ISOMET) at 90 rpm, then ultrasonically cleaned by acetone for 2 minutes. For cross sectional observations, an nickel coating was applied to protect the edge of the surface to be examined from polishing damage and edge rounding. The specimen was put into the electroless nickel coating solution (CASEWELL Inc.) for 1 hour at 85 ± 5 °C to obtain a layer of

30

30 μm. During polishing, care was taken to avoid polishing along the direction vertical to the surface to be examined. Epoxy (Technovit) was used to mount the specimens. Polishing procedure was used as in section 3.1.2.

Modified Keller's reagent (2 ml 48% HF, 3ml HCl, 20ml $HNO3$, 175ml H_2O) and gentle Graff Sargent (84ml H_2O, 0.5 ml HF, 15.5 ml $HNO3$, 3g $CrO3$) etching solutions were used. Mild etching (5 seconds) and slightly heavy etching (10 seconds) was applied to optical and SEM observation specimen, respectively.

An Optical digital image analyzer (Buehler Optical Microscope, max 1000 times) with an image analysis software (Figure 3.6), and a JEOL Scanning Electron Microscope (SEM) with Kevex 5100C X-ray Energy Dispersive Spectrometer (EDS) (Figure 3.7) were used to carry out the metallographic observation and elemental identification. A Buehler Hardness Tester (Figure 3.8) was utilized to measure Vickers and Knoop hardness values.

The surface roughness was measured using a stylus type surface profilometer (Mitutoya Mst-301). The surface topography of some specimens was examined using an Optical Surface Profilometer (WYKO NT 8000 System).

31

Chapter4

Part A - Experimental Results on the Al-Si Eutectic Alloys

4.1 Material Characterization

The optical micrographs showing general features of the two as-cast alloys (A13-S and A13-Z) and the two T6 heat-treated alloys (A13-C-T6 and A13-S-T6) are shown in Figures4.1-4.4. The optical image of the annealed A13-C-T6 (referred as A13-C-T6-AN) alloy, is shown in Figure 4.5. The microstructure of the annealed 6061 Al is shown in Figure 4.6. The two as-cast alloys A13-S and Al A13-Z exhibited needle-shaped Si particles in the Al matrix. The slight differences in Si particle size and matrix hardness between A13-S and A13-Z alloys resulted from their casting processes, in which the Zirconium-sand mold contributed faster cooling rate to the A13-Z alloy than the Silica-sand did. The Si particle aspect ratio, size and the bulk and matrix hardness of the alloys are summarized in Table 4.1.

The two T6 heat-treated alloys A13-C-T6 and A13-S-T6 were found to have round-shaped Si particles dominating their microstructures. SEM microstructures of the four alloys are shown in Figures 4.7-4.13. EDS spectrum of the phases in the four alloys are shown in Figures 4.14-4.17. Phases were determined by comparing their morphologies at high magnification to the phase identified in [77] on the base of their EDS spectra. Beside the Al matrix phase, the needle eutectic Si phase in the two as-cast alloys and the rounded eutectic Si phase in the two T6 heat treated alloys were

32

observed, large $Al_{15}(FeMn)_3Si_2$ (Chinese script) phase, Al_2Cu eutectic phase were observed in all the four alloys and the annealed A13-C-T6-AN alloy. Fine needle-shaped Cu-FE-Mn-Si phase was found in the tow as cast alloys. This unknown phases, however, was not observed in the T6 heat treated alloys. $Mg_8Si_6Cu_2$ phase was intermixed with the Al_2Cu (Figure 4.7b, Figure 4.8b, Figure 4.10b). The smaller and finer $Al_5Mg_8Si_6Cu_2$ needles in the T6 heat treated alloys than in the as-cast alloys may suggest this phase be dissolved during the heat treatment process.

The calculation of the average Si particle size (determined by average particle area) in Figure 4.16 demonstrated that there was a large differences in Si particle size between the as-cast alloys and the heat-treated alloys by 60%. The reduced Si particle length in the two T6 heat-treated alloys and the annealed A13-C-T6-AN alloy compared to the particle length in the two as-cast alloys indicates that the long Si needles became spheroidized during the heat treatment processes (Figure 4.17). It was found that the Si particle area fraction after heat treatment was slightly reduced (Figure 4.18). This was caused by the spheroidizing effect of the solution treatment. This heat treatment at elevated temperature resulted in an increase in the Si particle number (Figure 4.19). Aspect ratio distribution of Si particles in Figure 4.20 and average aspect ratio of the Si particles in Figure 4.21 revealed that the two T6 heat-treated Al-Si alloys had similarly small aspect ratios compared to the two as-cast alloys. At least 45% of the Si particles in the two heat treated alloys were roughly rounded to an average aspect ratio of 2. Whereas about 45% of the Si particles had

33

high aspect ratio which was larger than 4 in the as-cast alloys. Heat treatment did not significantly change the A13-C-T6-AN sample in terms of Si particle size and morphology compared to the A13-C-T6 alloy.

Figure 4.22 illustrates the measuring of the hardness methods for the Si particle concentrated area and the matrix (Si particle free area) microhardnesses on these alloys. The Vickers indenter was positioned at the typical area where the Si particles and aluminum matrix co-existed (Figure 22 a-b). A 1 kg load was used. To measure the matrix hardness, a shallow Knoop indenter was selected and located at a Si particle-free area under a minimum load of 10 g to avoid encountering Si particles at the subsurface (Figure 4.22c). It was found that the hardnesses of the silicon rich areas of the four alloys and the annealed A13-C-T6-AN alloy were similar (Figure 4.23a). This was contributed by the high hardness of Si phase (850-900 KHV). On the other hand, the two T6 heat-treated materials reached higher matrix hardness through the heat treatment processes compared with the two as-cast materials by 30%(Figure 4.23b), in which the A13-C-T6 achieved the highest Al matrix hardness (KHN 63). The A13-S had the lowest hardness (KHN46). The matrix hardness of A13-C-T6-AN sample was reduced to approximately the same as the A13-S alloy as a result of the annealing at 350°C.

4.2 Wear Rates of Al-Si Alloys Against 52100 Steel Rings

To understand the wear behaviour of the materials, dry sliding wear tests were initiated by investigating the volume loss of the Al-Si alloys as a function of the

34

sliding distance at 1N load level, and 1m/s sliding velocity. A linear relationship was observed between the volume loss and the sliding distance for all the alloys studied (Figure 4.24). It was found that the two heat treated alloys (A13-C-T6, A13-S-T6) showed lower volume losses at all sliding distances compared to the two as-cast materials, in which the silica-sand cast alloys (A13-S, A13-Z) resulted in the highest volume loss whereas the T6 heat treated A13-C-T6 material yielded the lowest volume loss.

The linear relationship between the volume loss and the sliding distance suggested that the volumetric wear rates can be computed from the slope of the volume loss-sliding distance curves as equilibrium wear rates. Therefore, for further tests the sliding distance at each load was fixed at 6×10^3 m for each test. The volumetric wear rate W (mm^3/m) was determined from:

$$W = \left(\frac{V}{D}\right) \qquad\qquad 4.1$$

Where V is the volume loss (mm^3) of the tested sample and D is the sliding distance (m).

It was recall that A13-S and A13-Z had similar needle-shaped Si particles, particle size and aluminum matrix hardness, and A13-C-T6 and A13-S-T6 had similar round-shaped Si particles, particle size and matrix hardness. Considering these factors and the wear data in Figure 4.24, A13-S and A13-C-T6 were selected as the representative

35

materials to represent each group of alloys (as cast and heat treated) for the further tests. The wear rates vs. load at 0.2, 1 and 2 m/s sliding velocities of the A13-S alloy and the A13-C-T6 alloy are plotted on the log-log axes in Figure 4.25.

It can be seen that both of the A13-S and A13-C-T6 alloys exhibited increasing wear rates with increasing the applied load at all sliding velocities. At 1m/s, wear rates of A13-C-T6 alloy increased from 4.46×10^{-5} mm^3/m at 0.3 N to 4.44×10^{-4} mm^3/m at 10 N, while the wear rates of A13-S increased from 1.01×10^{-4} mm^3/m at 0.3 N to 7.85×10^{-4} mm^3/m at 10 N. The largest difference in the wear rates between the two alloys was observed at 0.3 N. In general this difference became gradually smaller as the load increased.

Wear rates of A13-C-T6 and A13-S reduced with increasing the velocity at all load levels. For instance, wear rates of A13-C-T6 reduced from 8.11×10^{-4} mm^3/m at 0.2 m/s to 2.43×10^{-4} mm^3/m at 2 m/s at 0.3N load level, on the other hand wear rates of A13-S reduced from 1.30×10^{-4} mm^3/m at 0.2m/s to 3.24×10^{-5} mm^3/m at 2m/s at 0.3N. Wear rates of A13-C-T6 alloy were lower than wear rates of A13-S alloy at any load and any sliding velocity. This implies that round-shaped Si particles provided better wear resistance than acicular-shaped Si particles. Also the matrix hardness of the Al-13-C-T6 is 30% higher than that of the A13-S, which might be another factor responsible for better wear resistance. In addition to the wear rates, worn surface and debris demonstrated that these two alloys only underwent mild wear in the load range

36

of 0.3N to 10N. The worn surface and debris morphologies that are consistent with the features of the mild wear regime will be shown in the later section.

4.3 Counterface Wear

Wear rates of the AISI 52100 steel counterface shown in Figure 4.26 demonstrated that the counterface sliding against A13-C-T6 alloy exhibited lower wear rates than those sliding against A13-S samples, although A13-C-T6 alloy had higher matrix hardness than A13-S alloy by 30%. The change in the surface roughness of the rings will be discussed latter.

4.4 Wear Rates of Al-Si Alloys Against Cast Iron Rings

To study the effect of the counterface materials on the wear, AISI A40 type cast iron with a microhardness of 300 KHV (50gf) was selected as counterface ring. The microstructure of A40 cast iron is shown in Figure 4.27. Tests were conducted at a velocity of 1m/s and the results are plotted in Figure 4.28. To make a comparison, wear rates of A13-S and A13-C-T6 alloys sliding against the steel rings at 1m/s are also plotted.

It is well known that grey cast iron is an ideal tribological counterface material because the flake-like graphite particles it contains serve as solid lubricant to reduce the wear rate. In testing, two extreme wear behaviour, i.e. ultra mild wear and severe metallic wear occurred for both the A13-C-T6 and A13-S alloys in a relatively narrow load range of 1N to 5 N. At 5 N wear rates of A13-C-T6 and A13-S were both at 10^{-3}

37

magnitude. When the applied load was reduced to 2N, the wear rate of A13-S was slightly reduced to 8.21×10^{-4} mm^3/m. The significant reduction in the wear rate, which was 9.73×10^{-5} mm^3/m occurred at 1N. The wear rate of A13-C-T6, however, was drastically reduced to the ultra-mild wear region at a load of 2 N. This result suggested that the lubrication of graphitic solid was counterbalanced by another factor (ploughing of the counterface by Si particles) at higher load and as a result, wear rates were significant. This behavior was found closely related to the change of surface roughness of cast iron rings and will be discussed later.

4.5 Effect of the Al Matrix Hardness on Wear

To study the effect of Al matrix hardness on wear, the T6 heat-treated A13-C-T6 alloy was annealed at 350 °C. As a result, the Al matrix hardness was reduced to 47.2KHV from the original T6 hardness of 63.3KHV without causing any obvious change in Si particle size and morphology (Figures 4.16-4.21). This softened alloy was referred as A13-C-T6-AN. Wear tests were conducted at 1m/s constant speed and load levels that varied between 0.3 to 10N using the block-on-ring machine. The results are plotted in Figure 4.29. Wear rates of A13-C-T6 and A13-S were also plotted for comparison. It can be seen that at low load levels between 0.3 and 1 N wear rates of the A13-C-T6-AN specimens were almost the same as that of A13-S specimens, which has a comparable matrix hardness (48.7KHV). At loads higher than 2N, wear rates of the A13-C-T6-AN specimens became almost equal to those of the A13-C-T6 specimens. In conclusion, high Al matrix hardness reduced the wear at

38

low load levels. At higher loads, the morphology of the Si was the main factor to control wear. Rounded Si particles provided better wear resistance.

4.6 Characterization of the Worn Surfaces

Figure 4.30 (a) shows the general view of worn surfaces of A13-C-T6 worn against AISI 52100 steel rings at 5 N. Scoring or grooving of the surface occurred and the amount of the surface damage increased when the test load increased. The dark colored smooth regions and crater regions covered the entire worn surface. It can be seen that ploughing and scoring parallel to the sliding direction were the main characteristics of the smooth region. EDS analysis (Figure 4.30 (b)) showed that elemental iron transferred from the counterface was present in a considerably amount on the worn surface. The significant amount of elemental O suggested that oxidization occurred during sliding. Similar surface features were observed on the A13-S worn surfaces.

Figure 4.31 shows the worn surfaces of the A13-S and A13-C-T6 at 0.3N. Plastic deformation of the surface material resulted in the build up of aluminum at the exit edge of the wear scar. Compacted worn debris was frequently observed in the crater regions even after ultrasonically clean. More craters were found on A13-S worn surface than A13-C-T6 at 0.3 and 0.5 N.

Micro-cracks were frequently observed in smooth black areas in high magnification SEM micrograph, particularly when the load was increased (Figures 4.32a, b). The EDS spectrum (Figure 4.32 c) of the crater regions in Figure 4.32b also

39

showed significant amounts of Si and O element besides Al. Same results were found at all load levels in the two alloys. This suggested that mechanical mixing occurred in the crater region and eventually, formed parts of the tribo-layer. These are the typical features of mild wear regime in aluminum alloys.

When a cast iron ring counterface was used, two different wear behaviour were observed in both A13-S and A13-C-T6 alloys in a relatively narrow load range as described in section 4.4. The worn surface of A13-C-T6 at 2N was found to be of polished appearance (Figure 4.33a). Grooving and scoring were minimal. The worn surfaces of the A13-C-T6 at 5 N were ploughed (4.33b). Crater regions became aligned in the sliding direction. Similar worn surface morphology was found on the A13-S surfaces at 2N and 5N. Fe was transferred from the cast iron ring and smeared on the worn surface of the specimen (Figure 4.34).

The change of the surface roughness of AISI 52100 steel and A40 cast iron rings at different loads are showed in Figure 4.35. The surface roughnesses of the AISI 52100 rings against the A13-S were always slightly higher than those against A13-C-T6 at any load levels (Figure 4.35a), although A13-C-T6 had higher overall hardness than A13-S. Surface roughness of cast iron rings at 5N load was very high regardless of sliding against A13-C-T6 or A13-S samples (Figure 4.35b). When the load was reduced, the roughness of the cast iron ring against A13-C-T6 sample drastically reduced to about 0.1Ra at 2N. The roughness of the ring worn against A13-S samples, however, did not greatly reduce for tests lower than the load of 1N. The SEM

40

observation of the worn surfaces of the cast iron rings tested against A13-C-T6 samples showed that ring surface had a rather polished appearance at 2N (Figure 4.36a) but was severely roughened at 5 N (Figure 4.36b). The variations of surface roughness were induced by the different Si particle morphologies.

4.7 Characteristics of Debris

The morphology and composition of the debris generated by wear has been examined because they can often yield significant clues to identify the operating mechanism of wear. When AISI 52100 steel ring was used as the counterface, only mild wear was observed in the load range studied. Two wear mechanisms were observed in both of the alloys sliding against A40 cast iron rings based on the large differences in wear rates. Consequently the morphology and composition of debris were expected to be different in the two wear regimes.

In the mild wear regime the morphologies and compositions of debris obtained from the two alloys were similar. When the load was very low (0.3N), the debris mostly consisted of fine powder-like particles of diameter of less than 3 μm (Figure 4.38a). Increasing the load to 10N led to the growth of the fine particles to 5-6 μm in diameter (Figure 4.39a). A few flake-like particles of dimension of 15 – 25 μm length x 10 -15 μm wide were also found among the fine particles (Figure 4.38a, Figure 4.39a). EDS spectra from the marked areas in Figure 4.37-4.39 showed similar compositions, which suggested that the smaller particles may have initially been large flakes. When these flakes were released from the surface, deformation and fracture of

41

the flakes induced by the tribo-system likely broke up most of the large flakes into smaller particles.

When cast iron rings were used as counterface, severe wear was observed in A13-C-T6 at 5N, and in A13-S at 5 and 2N. For instance, huge flakes (>50 μm) dominated the A13-S debris at 5N (Figure 4.22a). White and dark coloured particles were found in the back-scattered SEM picture (Figure 4.22b). The white particles were Fe whereas the dark particles were the Al (due to the higher atomic number of Fe (56) than Al (27)). EDS of the debris showed no elemental oxygen in it (Figure 4.22c).

Besides the huge distinction in debris morphologies between the mild wear and the severe wear, the compositions of the debris generated in the two wear mechanisms were also different. Large amount of oxygen existed in debris from mild wear while severe wear yielded non-oxidized debris. In the mild wear, the formation of oxide film on the contacting surfaces was faster than delamination of the oxidized film. In severe wear, however, high rates of mechanical wear suppressed the oxidation, thus fresh metal was continuously deformed and extruded into debris.

4.8 Characterization of Subsurface Deformation

Cross sectional microstructures (Figures 4.41-4.42) showed that a compacted tribo-layer covered worn surfaces in the mild wear regime. The higher the applied load the thicker and more continuously the tribo-layer was. Underneath the tribo-layer layer was the deformed subsurface.

42

The depth of the subsurface deformation was depended on the test conditions and the alloys tested. Si particle fracture (particularly in A13-S alloy) indicated that the subsurface damage was a function of the depth from the worn surface, which is in turn determined by the applied load. Strains developed in the subsurface bended and broke the needle-shaped Si particles that became aligned in the sliding direction (Figure 4.41a, Figure 4.42a). Si particles extended nearby the tribo-layer underwent multiple fractures. Higher load levels yielded deeper damaged zones. At 10N, the depth at which the needle-shaped Si particles fractured extended to 40 μm below the surface (Figure 4.42), which was almost twice as that at 1N load (25 μm). The round-shaped Si particles, however, did not undergo much fracture at any load for tests between 1N and 10 N (Figure 4.41b, Figure 4.42b).

A statistical calculation of the Si particle fracture in the two alloys tested at 10 N is plotted in Figure 4.43. Almost all the needle-shaped Si particles fractured within the deep of 10 μm (Figure 4.43a). Each individual particle fragmented into at least 2 pieces (Figure 4.42a, Figure 4.43b). The number of fractured particles then gradually decreased with increasing the depth until 40 μm below which no particle fracture occurred. The round-shaped particles, on the other hand, had gone through minimal damage (Figure 4.43a-b). No fracture was observed when the depth was more than 20 μm.

To study the surface deformation better, a reference marker was introduced in a slit cut in the testing specimens (Figure 4.44a). The marker was machined from the

43

same alloy used to fabricate the test samples. After wear tests, bending of the interface between the marker and the bulk materials demonstrated significant subsurface deformation, although few Si particle fractures were observed (Figure 4.44b,c).

Medium size (50-70 µm) rounded Si particles hindered the matrix displacement in A13-C-T6 (Figure 4.44c) while small size (<15 µm) rounded Si particles did not seem to have an effect on the displacement gradients in the matrix (Figure 4.44b).

The plastic strain distribution (Figure 4.45) beneath the contact surface was obtained from the measurements of the displacements. The equivalent plastic strains ε have been evaluated from the shear angle of the interface, θ, [73], using the relationship

$$\varepsilon = \frac{\sqrt{3}}{3} \tan \theta \qquad\qquad 4.2$$

A large strain gradient was developed in the A13-C-T6 even at 1N in the subsurface areas, which generally consisted of small particles. For instance, at the depth of 5 µm from the surface the specimen underwent a strain of 2.5. Even at 25 µm depth the strain was 0.5. The strain of the areas with medium-sized particles (50-70 µm) was only 1.5 nearby the worn surface and reduced to almost 0 at the depth of 25 µm.

The subsurface deformation of the two tested alloys (A13-S, A13-C-T6) may be influenced by the Si particle morphologies and sizes. The needle-shaped Si particles underwent more fracture than the round-shaped Si particles in the same depth. The

44

medium size round-shaped silicon particles sufficiently hindered the strain gradient in the subsurface.

4.9. Single Pass Scratch Tests

To study the effect of Si particle morphology on the surface damage during wear, single-pass scratch tests were conducted at load varying from 0.25 to 5N in dry and lubricated condition. The contact pressure (Table 4.2) that the ball applied to the surface of the specimens calculated by

$$p_{max} = 0.981 \sqrt[3]{\frac{P}{R^2 a^2}}$$

4.3

$$a = \left(\frac{1-v_1^2}{E_1}\right) + \left(\frac{1-v_2^2}{E_2}\right)$$

4.4

Where P is the load, p_{max} is the maximum contact pressure, R is the radius, v is the Poison's ratio, E is Young's modulus and P is the load.

The variation of the coefficient of friction (COF) of A13-S and A13-C-T6 with distance at different applied loads is plotted in Figure 4.46. In both dry and lubricated conditions, the COF increased with the load. In dry tests (Figure 4.46a), the average values of the COF increased from 0.08 at 0.25N to 0.6 at 5N. At higher loads (2N-5N), the COF of A13-S was higher than A13-C-T6. In lubricated tests (Figure 4.46b), the lubricant layer eliminated the topographical differences in contact conditions between the indenter and the specimens during dry scratch test, leading to minimal

45

difference in COF at same load levels. Figure 4.47 shows that in dry scratch tests, COF of A13-C-T6-AN with lower matrix hardness was higher than A13-C-T6 (both had rounded Si particle morphology) at higher loads. Slightly lower COF of A13-C-T6-AN was observed in lubricated conditions compared to the A13-C-T6 sample. The COF of the three test alloys at dry and lubricated condition was plotted in Figure 4.48.

SEM observations showed that for the dry tests at 0.5N significant plastic deformation occurred on the surface of A13-S alloy (area A in Figure 4.49a). Deep scratches were developed (area marked B). The majority of micro-groves and plastic deformation ceased at the vicinity of the Si particles. The shear stress and/or normal stress caused particle fracture (C). About 56% of the exposed Si particles within the scratch track were fractured at 0.5 N. On the other hand, A13-C-T6 specimen underwent lesser amount of damage (Figure 4.49b). Large number of small spherical particles were pushed into the matrix. Only 37% of the particles within the scratch tracks were fractured.

Applying 1 ml of SAE 10W-30 engine oil on the test surfaces significantly reduced the amount of plastic deformation on the surfaces even at a high load of 5N (Figure 4.50a-b). Instead of surface scratching and grooving, aluminum smeared on the particles in the A13-S specimen (Figure 4.33a). Almost all (90%) of the needle-shaped Si particles were fractured and sunk down. This observation demonstrated that the normal stress, instead of the shear stress, dominated the material damage in lubricated scratch tests. Figure 4.50b shows that the majority of the medium size

46

round-shaped Si particles still stood out of the surface as load carriers. Only 16% of Si particles fractured in the surface of A13-C-T6 test samples.

Figure 4.51 demonstrated that in comparison with A13-C-T6 (Figure 4.50b), A13-C-T6-AN underwent more severe surface deformation at 0.5 N in dry scratch test. In lubricated tests (5N) the surface damage of A13-C-T6-AN in Figure 4.51b resulted in minimal deformation as A13-C-T6 (Figure 4.50b) under the same loading condition. These surface topographies agreed with the corresponding COF in Figure 4.48 and will be discussed in Section 4.15.

In the absence of Si particles, 6061 Al resulted in the catastrophic surface damage in both of the dry and lubricated conditions (Figure 4.52). Continuous and deep scratching and grooving damage marks extended to all the contact surfaces, which proved the value of the protective role of the Si particles in Al-Si alloys.

WYKO optical profilmoter showed more clearly the topographies of the scratch surfaces of A13-S and A13-C-T6 alloys (Figure 4.53). The A13-S specimens yielded a wider and deeper scratch track than A13-C-T6 specimens in both dry and lubricated tests. For instance, in dry tests (0.5N) the track of A13-S was 38 μm wide x 0.38 μm deep on the average, while in the A13-C-T6 the scratch track was 16.5 μm wide x 0.28 μm deep on the average (Figure 4.53a, b, Table 4.3). In lubricated tests (5N), plastic deformation along the sliding direction was greatly reduced although the dimension of the scratch tracks were significant (Figure 4.53c, d).

47

The single pass scratch tests have proven that the round-shaped silicon particles have higher fracture resistance than needle-shaped particles. The harder aluminum matrix protected the surface and silicon particles better than soft matrix under the same condition. The combination of round silicon particles and hard aluminum matrix contributed to lower COF.

4.10 Reciprocating Sliding Wear Tests

To further study the fracture behavior of the Si particles under the reciprocating motion similar to the automotive engine, reciprocating wear tests were conducted using the engine simulator at an engine operating temperature of 150 °C. The load was 1.2 N and the corresponding Hertzian contact pressure was 154 MPa, which was calculated using Equations 4.2 and 4.3. The worn topographies of A13-S and A13-C-T6 specimen are shown in Figures 4.54 and 4.55. The worn surface observations under the optical microscope at 500X showed that surface damage in A13-S was more severe than A13-C-T6 specimen. All the exposed needle-shaped Si particles were fractured (Figure 4.54a, b) and ground (Figure 4.56a). On the other hand, particle fracture was insignificant on the A13-C-T6 specimen. Worn debris formed "comets" along the sliding direction. More comets were found on the A13-S specimen surface. Optical Profilemeter image showed that the width and depth of the A13-S worn track (Figure 4.57a, Table 4.4) was much larger than A13-C-T6 (Figure 4.57b, Table 4.4).

48

Part B - Discussion of Experimental Results

4.11. Summary of Observations

1) Microstructures: Round-shaped Si particles and high Al matrix hardness were the characteristic features of the two T6 heat-treated alloys (A13-C-T6 and A13-S-T6), whereas needle-shaped Si particles dominated the softer Al matrix in the two as-cast alloys (A13-S and A13-Z). Among them the A13-C-T6 alloy had Si particles with the smallest aspect ratio (average 2.0) and the hardest Al matrix (63.3 KHN) whilst the A13-S alloy represented the other extreme with higher aspect ratio particles (average 4.2) in the softest Al matrix (48.7 KHN).

2) Wear Rates: For the block-on-ring dry sliding tests, wear rates of the A13-C-T6 and A13-S were all in the mild regime ($3 \times 10^{-5} - 9 \times 10^{-3}$ mm^3/m) in the load range between 0.3 and 10 N when tested against AISI 52100 steel. Wear rates of the two alloys increased with increasing the load and decreased with increasing sliding velocities. Wear rates of A13-C-T6 alloys were lower than those of A13-S at any load level and velocity.

It was interesting to see that the grey cast iron, the conventional tribological material, did not reduce the wear rates of the two alloys. On the contrary, it significantly increased the wear rates at higher loads. This significant increase occurred in the A13-C-T6 with a matrix hardness of 63.3 KHN at the load range of 2

49

to 5N and in the A13-S with a matrix hardness of 48.7 KHN at the load range of as low as of 1-2 N.

3) Worn Surfaces: Dark smooth and crater regions were the main features of the worn surfaces. Longitudinal scratches and grooves extended on the smooth areas. Oxidation and counterface material transfer also took place. In the severe wear regime (which occurred when a cast iron counterface was used), both the specimens and the counterface were severely ploughed without showing any evidence for oxidation.

4) Worn Debris: The morphology of the worn debris was typically in the form of fine size powder-like particles and the size increased with increasing the load from 0.3 to 2 N. At higher load range ($\geq$ 5 N), the debris was mostly in the form of large flake-like particles. Compositions of the debris at all loads were found similar to that of the corresponding worn surfaces, which was Fe, Al and O.

5) Si particle fracture: Significant Si particle fracture (about 99%) was observed in the A13-S subsurfaces while the number of the fractured particles in the A13-C-T6 subsurfaces was much smaller (about 25%). Subsurface deformation increased with increasing the load. Medium size ($50 - 70$ μm^2) round-shaped Si particles had higher fracture resistance and delayed the matrix deformation more efficiently compared to the small particles and the needle-shaped particles.

6) Scratch tests: Scratch tests were done to analyze the Si fracture and matrix hardness in more detail. During a single unidirectional pass of the indenter, it was found that the plastic deformation of A13-S specimens along the sliding direction was more

50

significant than that of the A13-C-T6 specimens at low loads ($\leq 0.5N$) in dry scratch test. Significant amount of deformed the Al matrix was found to have been piled-up at the back of the needle-shaped Si particles in the A13-S under dry scratch conditions (0.5N).

The number of the fractured Si particles, particularly the amount of the surface damage was increased in the A13-C-T6-AN specimens compared to those in the A13-C-T6 specimens at the same condition. This indicated the importance of the matrix hardness in the surface protection during wear. In the lubricated scratch testing condition (5N), aluminum smeared on the A13-S surface. Si particle fracture on the A13-S surface occurred at a higher frequency than those on the A13-C-T6 surface. Damage on the A13-C-T6 surface in the sliding direction was small but the majority of the small spherical particles were sunk down in the matrix. The COF of the A13-C-T6 was lower than that of the A13-S in dry scratch tests.

In dry scratch tests, A13-C-T6-AN specimen underwent more plastic deformation along the sliding direction than A13-C-T6 specimen due to the softer Al matrix. The damage in the A13-C-T6-AN was comparable to the matrix deformation occurred to A13-S alloy with the same matrix hardness. However, the COF of A13-C-T6-AN with spherical particles was lower than A13-S at higher load levels (from 1N).

7) Reciprocating wear tests showed that round-shaped Si particles suffered much less fracture than the needle-shaped Si particles under the engine operation temperature,

51

sliding motion, hydrostatic contact condition and high velocity. This was in agreement with the results of the single-pass scratch tests.

Based on the above summary, it is concluded that the T6 heat treated alloys, particularly the A13-C-T6 alloy has higher wear resistance than the as-cast alloys. High aluminum matrix hardness and fine spherical Si particles contributed to this high wear resistance.

4.12 Si Particle Fracture

Si phase particles embedded in a soft aluminum matrix serve as load bearing constituents in the Al-Si alloys. On the surfaces of these alloys tribolayers form during sliding wear. Fractured pieces of hard particles promote wear since they fail to support the surface tribo-layer (Figure 4.41-Figure 4.42). They may also facilitate scuffing by acting as third body abrasive particles [76]. This will be discussed in Chapter 5. The fracture behaviour of the second phases was investigated in detail by performing single pass scratch tests on the etched surfaces of A13-S and A13-C-T6 alloys and by examining the subsurface deformation of the worn specimens. Scratch test is considered to be a good approach to reveal the topography of the worn surface prior to being covered by the tribo-layers. Surface damage was caused by two types of stress: Shear stress that caused the surface plastic deformation of aluminum (Figure 4.49), and compressive stress which led to significant particle sink-down and fracture (Figure 4.50). It has been reported that two mechanisms were responsible for the fracture of the exposed Si particles [76]. The first type of fracture occurred as a result

52

of shear stress developed at the root of these particles, where they were embedded in the aluminum matrix. This led to the removal of relatively large fragments of material from the exposed portions of the particles (C in Figure 4.49a). A second mechanism was the fracture and fragmentation of the edges of the particles that came in contact with the counterface. This type of fracture resulted in removal of smaller pieces from the particle surfaces at each contact cycle. Likewise, after the formation of the tribo-layer, these two mechanisms were likely responsible for the further fragmentation of the fractured particles that had been involved into the tribo-layer.

As the Si particles blocked and/or retarded the substrate displacements of material adjacent to worn surface, stress may become accumulated along the particles. This cumulative tensile stress, when surpasses the fracture strength of the particles, fractures the Si particles.

Statistical calculations (Figure 4.41) showed that round-shaped Si particles have higher fracture resistance than needle-shaped Si particles. Three factors contributed to this difference. Firstly, stress gradients along the large needle-shaped Si particles were much larger than that along the round-shaped Si particles, particularly when the particles were aligned in the perpendicular to the sliding direction on the surface. Secondly, the matrix flow of the deformed aluminum was easier around the spherical particles than that of the needle-shaped particles. It was observed in scratch tests (Figure 4.49a and Figure 4.50a) that the matrix plastic deformation in the surface of the A13-S specimens was hindered at the vicinity of the Si particles. Surface energy

53

was another factor that is responsible for different fracture behaviour. For the same geometric volume, the spherical shape yields the smallest surface area, thus resulting in the most "stable-state" due to the lowest surface energy. These particles are more resistant to fracture.

4.13 Effects of Counterface Materials and Particle Morphologies on Wear Mechanisms

Aluminum-silicon alloys exhibit two forms of wear under dry sliding conditions. These are oxidative and metallic wear. Large amounts of oxide products were found using the EDS in both the worn debris and the worn surface of the as-cast alloy A13-S and heat-treated alloy A13-C-T6 worn against AISI 52100 steel ring counterface. Oxidative wear occurred in A13-S up to a load of 1N and in A13-C-T6 up to a load of 2N when worn against A40 grey cast iron rings (Figure 4.30, Figure 4.32). Above these load levels, i.e. A13-S at 2N and A13-C-T6 at 5N, metallic wear occurred at high wear rates. Oxidative wear and metallic wear have distinct characteristic metallographic features. Oxidative wear occurs when an oxide or mixed oxide metal from the specimen and the counterface surface forming a tribo-layer covers the wear specimens and the counterface surfaces (Figure 4.30, Figure 4.32). There is also plenty of evidence for localized deformation of substrate and fracture of the silicon particles (Figure 4.41, Figure 4.42). The oxide thickness and deformed substrate thickness varied considerably with the applied loads. Wear of the alloys occurred through a process of spoliation or delamination of the tribo-layers. The detached parts

54

of the layer then did not exit the tribo-system immediately. Debris examination (Figures 4.37-4.39) indicated that the detached particles were broken-up into smaller size by the interaction of the steel counterface and the sample surface. The entrapped Si particle fragmented in the surface layer may have acted as third body abrasives and increased the rate of wear. The aluminum specimens and the steel rings were always separated by this oxide rich layer. Wear rates were low because the amount of metal removed was confined to the thickness of the tribo-layer. The volume loss of the counterface was negligible (Figure 4.26) due to the high hardness of the steel rings (850-900 HV). The hard surface of the counterface minimized the ploughing of the counterface, thus, facilitated the survival of the tribo-layer at higher loads.

Metallic wear occurs when deformation of the surface occurs on a massive scale. In this case, fracture occurred with the separation of large fragments of metal, resulting in relatively large flake-like debris (Figure 4.40). Metallic wear was not been expected to occur at a load as low as 1 or 2N, particularly when the cast iron ring was used as the counterface, which is capable of providing solid graphitic lubricant. The premature metallic wear was due to the morphology of the Si particle and the hardness of the counterface.

Wear rates of A13-C-T6 and A13-S samples in Figure 4.28 corresponded to the roughness change of the cast iron rings in Figure 4.35b. The A13-C-T6 sample and its counterface were both severely roughened at 5 N. But at 2 N both components of the tribological couple was polished. This suggested that the change in the wear behavior

55

correlated with the change of the surface topography of the counterface: As the hardness of the cast iron rings (300HV) was much lower than that of the Si particles (900 HV), Si particles embedded in the Al-Si alloy surface layer roughened the rings easily at 2 N load. The ploughed counterface then accelerated the removal of the Al matrix. The Si particles eventually lost support and fractured and finally became detached from the surface. As the needle-shaped particles were much shaper than the round-shaped particles, and their fracture resistance was also lower than the round-shaped particles, wear of the A13-S alloy occurred at higher rates than the A13-C-T6 alloy (Figure 4.28). At 1N, the flake-like graphite particles sufficiently reduced the friction. Shear stress was not high enough to induce significant Si particle fracture. The build-up of the oxidative surface layer was faster than the delamination of the layer, thus, oxidative wear continued to occur at higher load. In the A13-C-T6 alloy, the round-shaped Si particles with higher anti-fracture ability were capable of keeping the oxidative wear until 2N.

4.14 Effect of Al Matrix Hardness and Particle Morphology on Wear

Figure 4.29 shows that wear rates of A13-C-T6-AN were almost the same as that of A13-S at loads varying from 0.5 to 1N and then were reduced to almost equal to A13-C-T6 from 2N to 10N. It was of interest to find that the A13-C-T6-AN had the same aluminum matrix hardness as the A13-S, but different Si particle morphology, whilst the A13-C-T6-AN had the same Si particle morphology as the A13-C-T6 but lower aluminum matrix hardness. The Al matrix hardness was thought to be

56

responsible for the difference in wear rates of A13-C-T6 and A13-C-T6-AN specimens at low load range (Figure 4.29). According to the Archard's law (Eq. 2.4), wear rates could be simplified to be a function of applied load (P) divided by the bulk hardness of the soft material (H). After the initial run-in period, all the protruded Si particles that higher than the Al asperities were ground to the same height level as the aluminum matrix asperities. Accordingly, the applied pressure was mainly shouldered by the contacting Al matrix asperities due to the low volume percentage of the Si phase. As a result, the A13-C-T6 specimen with harder aluminum matrix remained lower wear rates than the A13-C-T6-AN specimen.

When the applied stress was high enough ($\geq$ 2N) to surpass the yield stress of the Al matrix asperities, the contacting soft Al matrix asperities, rather than the hard particles, were plastically deformed, thus made the Si particle asperities act as the main constituents to carry the load. Under this circumstance, as it has been discussed earlier, the sharp-angle particles plough the counterface more severely than the rounded particles. The roughened counterface, in return, increased the wear rates of the specimen (Figure 4.28).

4.15 Effect of Al Matrix Hardness and Particle Morphology on COF

Figure 4.48a showed complex effects of aluminum matrix hardness and particle morphology on the COF. In dry scratch tests, the A13-S obtained the highest COF and the A13-C-T6-AN was higher than A13-C-T6. In lubricated single-pass scratch tests, although A13-S still remained the highest COF, the COF of the harder A13-C-T6

57

became higher than that of the softer A13-C-T6-AN. As soft Al matrix facilitated the metal transfer to the counterface when the applied stress was high enough to deform the matrix phase. In dry tests, the ball indenter picked more deformed aluminum matrix from the A13-S and the A13-C-T6-AN surfaces than from the A13-C-T6 surface. When the ball passed over the Si particles, the transferred Al were cut by the edge of the Si particles and piled-up at the root of the particles (Figure 4.49a,b, Figure 4.51a), resulting in an increase in COF. The highest COF of the A13-S specimen resulted from the higher amount of transferred Al due to the lowest matrix hardness and larger amount of detached Al due to the much sharper and larger needle-shaped Si particles.

With the application of lubricant, the Al transfer was effectively suppressed, leading to small differences between the COFs of the A13-S, the A13-C-T6 and the A13-C-T6-AN alloys (Figure 4.48b) although the COF of the A13-S with needle like particles was still the highest. The COF of the A13-C-T6-AN was lower than that of the A13-C-T6, which suggested that Al matrix deformation may be the reason for the lower COF.

58

Chapter 5

Part A - Experimental Results on Scuffing of Al-Si Based MMCs and Al-Si Eutectic Alloys

5.1 Scuffing of Al-Si Based Composites

5.1.1 The Onset of Scuffing

The Al-Si based composite materials used in the scuffing tests were A356Al-Si alloy reinforced by 0, 3, 5 vol. % of Al_2O_3 and graphite particles. The compositions of the composites tested are shown in Table 5.1. Two kinds of Al_2O_3 particles were utilized in these composites. The SEM microstructures of the composites materials are shown in Figure 5.1.

The onset of scuffing was determined using a stepwise loading test. Some visual observations during the tests were significant. After the run-in period, all the surface topographies of the composites were similar at the onset of scuffing. Figure 5.2 shows the scuffed surface of 5A3G(C) specimen. When the load was increased in the range of 150N and 180N, the surfaces became dark coloured (A in Figure 5.2). Light scratches appeared along the sliding direction but they soon disappeared. High magnification SEM micrographs (Figure 5.3) showed the plastic deformation locally parallel to the sliding direction. Alumina particles were fractured and became exposed on the surface. Some worn debris was attached on the surface. EDS (Figure 5.4) investigations showed that a tribological layer, which was a mixture of elemental Al, Si, Fe, Cr was likely formed. A compacted smeared layer developed in the dark zone (Figure 5.5). Prior to the scuffing

59

load-step, shiny-metal spots appeared in the darkened areas and eventually some of them advanced and formed a continuously metallic band structure (B in Figure 5.2). Figure 5.6 shows the shiny band structure at high magnification. Light grooving and scratching developed in the polished areas. Normal stresses compressed and flattened the contacting areas. The development of the fresh-metalic zone on one side of the specimen indicated that catastrophic wear would be initiated in this area.

5.1.2 Correlation of Reinforcement and Scuffing Load

Figure 5.7 shows the scuffing loads, and Figure 5.8 shows the sliding distance at scuffing for the composite materials. It is seen that 5A3G (C) and 5A5G samples scuffed at 350N, and 5A5G scuffed at the very beginning of the last loading step. 5A3G (F) and 3A5G scuffed at 320N, but the latter one scuffed at longer distance than 3A5G at the same load. 5A0G scuffed at 310N and 0A5G scuffed at a very early stage at 270N. It was apparent that the scuffing load was associated with the volume of the reinforcements in the Al composites. To further investigate the relationship, 5A5G, 3A5G, 0A5G and 5A5G, 5A3G (F), 5A0G were examined in the following way: Scuffing load vs. vol.% of Al_2O_3 particles and scuffing load vs. vol.% of graphite particles were plotted in Figure 5.9 and Figure 5.10, respectively. These plots suggested that scuffing load was a stronger function of volume percentage of the alumina particles, i.e., the ceramic particles significantly increased the scuffing resistance. Graphite particles generally increased the scuffing load too. However, when the graphite vol.% was lower than 3 it had almost no influence on the scuffing load. Higher vol.% of graphite delayed the onset of scuffing just as well as the ceramic particles: The scuffing load was increased by 40N by adding only

60

2vol.% of graphite particles. In summary, the load-induced scuffing resistance increased with the increase of content of alumina and graphite particles.

5.1.3 Topography of the Scuffed Surfaces

A visual inspection easily revealed the degree of the surface damage. The typical low magnification micrographs of the 6 types of A356 Al-graphite composites representing the characteristic features of the surfaces after scuffing are shown in Figure 5.11. SEM surface topographies are shown in Figure 5.12. The severity of the damaged surfaces was quantatively described in Figure 5.13 by the change of the surface roughness after scuffing. The 0A5G liner specimen which scuffed at the lowest load was also the most severely worn (Figure 5.11). The entire surface layer was torn away. The scratches and deformation caused fresh metal substrate layers to become completely exposed and flow in the sliding direction (Fig.5.12a). Worn surfaces of the 3A5G and 5A0G manifested themselves similarly with a massive deformation and surface damage (Fig.5.12b, c) with the remaining tribolayers occasionally existed over the surfaces. According to the SEM observations, Al_2O_3 particles were frequently observed to be protruding out of the surfaces as load bearing elements. The 5A3G (F) worn surface was observed by naked eyes and showed that the continuous tribo-layer still covered most of the scuffed surface. Microgrooves and ploughing can be observed with graphite particles being pulled out of the surface (Figure 5.12d). Significant improvements were observed on the 5A3G (C) and 5A5G worn surfaces: No large areas of fresh metal were exposed on the surfaces. The presence of the longitudinal shiny-metal band suggested that local welding occurred between the asperities in the samples and counterfaces. Further evidence proved that the banding on the two sliding surfaces occurred by Al transfer to the counterface (Figure

61

5.14). Figures 5.11-5.13 revealed that higher content of the reinforcements could reduce the intensity of the damage to the scuffed subsurfaces. Cracks along the sliding direction were found under the subsurface of scuffed composites (Figure 5.15).

5.1.4 Particle Size Factor

The effect of ceramic particle size on scuffing was studied by comparing scuffing of the 5A3G (F) and 5A3G (C), which consisted of the same concentrations of Al_2O_3 particles and graphite particles, but had different ceramic particle size (Table 5.1). It was the difference in the particle size that resulted in scuffing occurred at different loads (Figure 5.16). The initial higher surface roughness (1.35µm) of 5A3G (C) resulted from the coarse particles embedded on the surface. Coarse particles contributed to higher scuffing resistance and less scuffing damage than the finer particles did.

5.2 Scuffing of Al-Si Eutectic Alloys

To study the scuffing behaviour of the Al-Si eutectic GM 396 alloys, scuffing tests were done in roll-on-flat configuration using reciprocating wear machine as described in Chapter 3 (Figure 3.4). A13-S and A13-C-T6 alloys were selected as the specimens. The chemical compositions and microstructures are shown in Figures 4.1-4.10.

The surface of the specimen were prepared using 400 and 600 grinding papers. The same experimental procedure as the Al-Si based composites tests was used in the tests. Scuffing criteria for Al-Si alloys was the same as described in section 5.1.1.

Both of the alloys were found scuffed at the load of 270N. Significant scratches were observed on both of the surfaces of the test samples (Figure 5.17, Figure 5.20). Large areas of plastically deformed aluminum became aligned on the A13-S sample along the sliding direction. This indicated that local welding occurred between the counterface and

62

the specimen during sliding. Besides, no deep gallings, aluminum smear was observed on the surface of A13-C-T6 samples.

Counterface observations have shown that the top area of the M2 roller against A-13-S specimen was flattened. Large amount of aluminum transferred onto the counterface (Figure 5.18). On the surface of the M2 counterface against A13-C-T6 alloy, however, aluminum transfer was minimal (Figure 5.20), although ploughing marks were found on the surface.

Part B – Discussion

5.3 Scuffing of Al-Si Based Composites

During the running-in period, surface roughness was slightly reduced due to the removal of the asperities from the relatively high spots on the surfaces. Upon further sliding some wear debris plastically flowed into the valleys. Some wear debris may have smeared over the specimen surface under high pressure and high temperature. Smearing of this mechanical mixture from specimen, counterface and the oil additives continued until a thin compacted dark layer with a smooth surface continually covered the entire surface (Figure 5.2). The shearable graphite particles in the surface layers reduced the COF.

Under higher load aluminum transfer occurred to the counterface. The aluminum transfer could be initiated by two sources: (1) Large ceramic particle detached from the bulk materials could not be trapped by this layer and rolled freely as three-body micro-cutters, which resulted in the micro-scuffing (mild scratches) as in Figure 5.2 and Figure 5.6. This micro-scuffing can be self-healed during the subsequent sliding action. However, the two deformed edges of the scratches may weld on to the counterface; (2) The aluminum wear debris might become attached to the counterface. As a result, the contact stress was increased and resulted in more aluminum transfer. When these transferred aluminum particles smeared back to the specimen surface, they formed the compact layer as shown in Figure 5.5. Either the transferred layer (Figure 5.14) or the back-transferred layer could significantly increase the local contact stress, thus generated large amount of heat. Large areas of welded material then formed and tore off the thin

64

surface layer. With the exposure of large area of fresh metal to the counterface, the scuffing condition was reached.

Graphite particles or ceramic particles embedded in the metals both serve to safeguard the aluminum matrix. Graphite particles provided the solid lubricant on the surface thus reduce the generation of frictional heat. Load bearing ability of the ceramic particles protected samples from damage caused by the counterface after loosing the surface layer. Consequently, samples with higher amount of graphite and ceramic particles exhibited higher scuffing resistance.

Figure 5.16 schematically illustrated the effect of particle size on scuffing. When the ring surface contacted the fresh materials directly, the coarse particles protruded out of the surface more than the finer particles. Consequently, they prevented the asperities from banding more efficiently with the counterface.

5.4 Scuffing of Al-Si Eutectic Alloys

Based on the observation of the scuffed surface of the A13-S specimen and A13-C-T6 specimen, A13-C-T6 alloy has higher scuffing resistance than A13-S alloy. The scuffing was initialed by the three-body particle fragments rolling between the counterface and specimen under the high load level. These scratches may eventually develop into significant aluminum smear as a result of aluminum transfer.

65

Chapter 6

Conclusions and Suggestions for Future Work

6.1 Conclusions

6.1.1 Conclusions on the Al-Si Alloys

1) A13-C-T6 alloy demonstrated superior wear resistance compared to the as-cast alloy A13-S over the entire load range between 0.3N and 10N. Both of the alloys demonstrated mild wear regime when sliding against AISI 52100 steel rings. Severe wear was observed to both of the alloys (A13-C-T6 alloy above 5N, A13-S alloy above 2N) when A40 cast iron ring counterface was used.

2) Worn surfaces in mild wear were characterized by low wear rates, surface grooves, plastic deformation, and fine powder-like debris. Large amount of elemental oxygen was found on the worn surface and debris. (Severe wear featured with high wear rates, large flake-like metallic debris, counterface material transfer to the worn surface without identification of elemental oxygen neither on the worn surface nor in debris).

3) Si particle morphology controlled wear through the counterface-ploughing and the particle-fracture. Round-shaped particles are better than needle-shaped particles in terms of providing lesser amount of counterface ploughing.

4) More needle-shaped Si particles fractured in the A13-S alloy than round-shaped Si particles in the A13-C-T6 alloy in the subsurface. At the same load level subsurface of A13-S alloy underwent large displacement than that of A13-C-T6 alloy. Medium size (50-70 μm^2) round-shaped Si particles suppressed the subsurface displacement

66

more effectively than small particles. Spherical silicon particles provided better wear resistance at the same matrix hardness.

5) Aluminum matrix hardness was the dominant factor that control wear at low load levels, whilst at high load levels Si particle morphology played more important role in wear.

6) Subsurface observation of the wear samples and scratch tests have proven that round-shaped Si particles had higher fracture resistance than needle-shaped Si particles.

7) The coefficient of friction of A13-C-T6 alloy was lower than A13-S alloy in both dry and lubricated conditions. This was resulted from the complex contribution of aluminum matrix hardness and the Si particle morphology.

8) The high temperature reciprocating wear tests under lubricated condition have demonstrated that the A13-C-T6 alloy underwent minimal surface damage with respect to the A13-S alloy after etching; the A13-C-T6 alloy had higher scuffing resistance than A13-S alloy at boundary lubrication condition.

6.1.2 Conclusions on Al-Si Based Composites

1) Scuffing was initialed by material transferring to the counterface or back-transferring to the liner surface. Thus the breakdown of the lubrication film led to metal-to-metal contact resulting in locally overheat condition. This overheat resulted in local welding and eventually, approached the onset of scuffing.

2) The scuffing resistance of the composites increased with increasing the volume of Graphite and ceramic particles.

3) Coarse particles gave rise to higher scuffing resistance and less surface damage after scuffing than fine particles.

67

4) The severity of the damage of scuffed surface was related to the volume fraction of reinforcement, e.g., higher volume fraction of ceramic and graphite particles resulted in less surface damage.

6.2 Suggestions for Future Work

The author would suggest that there are two main areas where further study should take place. Firstly, more work need to be done on reciprocating wear behavior in lubricated conditions, particularly the investigation on subsurface after high cycles of sliding wear. Secondly, the effect of engine operating temperature on strength of Al matrix would be of interest.

List of References

[1]   B.S. Shabel, D.A. and W.G. Truckner, in P.J. Blau (ed.), ASM International, Metals Park, OH (1992) 785.

[2]   Y. Wang and S. C. Tung, Wear, 225-229 (1999) 1100-1108.

[3]   R. Shivanath, B. Tech. P.K. Sengupta, M Met. T. S. Eyre, J. of the British Foundryman Vol 70 (1977), 349-356.

[4]   S. Das, S. V. Prasad, T. R. Ramachandran, Tribology of Al-Si Alloy-Graphite Composites, J. of Materials Science (1987), 22-26

[5]   I. M. Hutchings, S. Wilson, A.T. Alpas, in Comprehensive Composite Materials, A. Kelly and C. Zweben, eds., vol. 3, Metal Matrix Composites, T.W. Clyne, ed., Elsevier, Oxford, 2000, chapter 19, "Wear of aluminum-based composites." 501-519.

[6]   C.S. Lee, Y.H. Kim, K.S. Han, T. Lim, J. of Materials Science, 27 (1992), 793-800.

[7]   C.I. Peel, in Metal Matrix Composites for Aerospace Applications, Euromat '91 (1992), 41-51

[8]   Standard Terminology Relating to Erosion and Wear; G40, Annual Book of ASTM Standards, ASTM, 145

[9]   C.S. Yust, International Metal Review, vol 30 (1985), No 3, 141-154

[10] O. Vingsbo, Engineering Materials for Advanced Friction and Wear Applications, ASM (1988), 1-10

[11] K.C. Ludema, in ASM Handbook, vol. 18, Friction and Wear Applications, ASM (1992), 257-271

[12] C.S. Lee, Tribology and Wear, International Metal Reviews, vol 30 (1985), No. 3, 141-154

[13] T.F.J. Quinn, Tribology International, vol 16, 5, Oct. 1983, 257-271

[14] T.F.J. Quinn, Tribology International, vol 16, No. 6, Dec 1983, 305-315

[15] E.F. Finkin, Adhesive Wear: A General Review of the Experimental Knowledge and Theory, Materials in Engineering Applications, vol 1, April 1979, 154-161.

[16] L.E. Samuels, E.D. Doyle and D.M. Truly, in ASM 1980 Material Science Seminar, edited by David A. Rigney, 5-35.

[17] M. F. Jenson, J.Bottiger, Wear 253 (2002) 1044-1056

[18] E. Rabinowicz, Friction and Wear of Materials, Wiley, U.S.A., 1965.

[19] N.P. Suh, Tribophysics, Prentice-Hall, New Jersey, 1986.

[20] S.C. Lim & M.F. Ashby, Acta Metal. Vol 35, No. 1 (1987), 1-24

[21] K.C. Ludema, Sliding and Adhesive Wear, vol. 18, Friction, Lubrication, and wear technology, ASM (1992), 237

[22] I.M. Hutchings, Sliding Wear, in Friction and Wear of Engineering Materials, 1992) ,82-92

[23] G. Dieter, Mechanical Metallurgy, Third edition, (1988) 301-304

[24] W. Ames, A.T. Alpas, Metall. Mater. Trans. A 26, (1995), 85.

[25] S. Wilson, A.T. Alpas, Wear 212 (1997) 41.

[26] A. Martin, M.A. Martinez, J. llorca, J. Wear 193 (1996) 169.

[27] S. Wilson, A.T. Alpas, Wear 196 (1996) 270.

[28] M.F. Ashby, J. Abulawi, Tribology Transitions (1991), vol.34, 4. 577-587.

[29] W. Hirst and J.K. Lancaster, The Influence of Speed on Metallic Wear, 229-241.

[30] J. K. Lancaster, Tribology International, Dec., 1990, vol 23, No. 6, 445-454.

[31] N.P. Suh, Fundamentals of Friction and Wear of Materials, ASM, (1981), 43-71

[32] S. V. Prasad, B.D. McConnel, Wear of Materials, ASME, (1991), 149.

[33] S. Das, S.V. Prasad, Wear 133 (1989) 173.

[34] P.K. Rohatgi, Y Liu, T.L. Barr, Metall. Trans. A 22 (1991), 1435.

[35] A.R. Riahi, A.T. Alpas, Wear 251 (2001), 1396-1407.

[36] H. Cheng, ASM Handbook, Friction, Lubrication, and Wear Technology, Vol. 18, 237.

[37] D. A. Rigney, Annual Reviews of Materials Science, 18 (1988), 141-163.

[38] K.H. Zum Gahr, Elsevier, New York (1987), 815.

[39] A. Kasak, T.A. Nuemeyer, Wear, 14 (1996), 445-454.

[40] Y.G. Proskuryakov, I.V. Pozdnuakova, Russian Engineering J. 43, 9 (1963), 35-38.

[41] R. S. Montgomery, Wear of Materials, K.C. Ludema ed., ASME, NY (1983) 465-470.

[42] E. Rabinowicz, Friction, Wear and Lubrication: Study Guide, MIT, Cambridge (1977)

[43] R. S. Montgomery, Wear, 24 (1973), 247-248

[44] Ludema, in Wear, Editor Duncan Dowson Elesevier, Celebration vol. 315-331.

[45] J.R. Davis, ASM Handbook, Friction, Lubrication and wear Technology, Vol 18, 553-558

[46] F. J. Martin, Wear 253 (2002), 1044-1056

[47] K. Holmes, Amsterdam ; New York : Elsevier (1993), 272-280.

[48] S.K. Biswas, A. S. Reddy, J. Indian Inst. Sci. (1996), 75, 15-35.

[49] K.M. Jasim, E.S. Dwarakadasa, Wear 54 (1987), 119-130

[50] J. Clark, A.D. Sarkar, Wear 82 (1982), 179-195.

[51] A.R. Rosenfield, 116 (1987), 317-328.

[52] J. Zhang, A.T. Alpas, Materials Science and Engineering A, A160 (1993), 25-35

[53] B.N. Pramila Bai, S.K. Biswas, J. of the ASLE, vol. 43, 1 (1987), 57-61.

[54] A. Somi Reddy, B.N. Pramila Bai, K.S.S Murthy, S.K. Biswas, Wear (1994), 115-127.

[55] B.N. Pramila Bai, E.S. Dwarakadasa, S.K. Biswas, wear 71 (1981), 381-384.

[56] X.Y. Li, K.N. Tandon, 225-229 (1999), 640-648.

[57] R.L. Deuis, C. Subramanian, J. M. Yellup, Composites Science and Technology 57 (1997), 415-435.

[58] K.M. Jasim, E.S. Dwarakadasa, J. of Material Science Letters, 12 (1993) 650-653.

[59] J. Clark, A.D. Sarkar, Wear 54 (1987), 7-16.

[60] B.N. Pramila Bai, S.k. Biswas, Wear 120 (1987), 61-74

[61] J.B. Andrews, M.V. Seneviratne, K.P. Zier and T.R. Jett, in 'Proc. Conf. Wear of Materials 1985, ed. K.C. Ludema, ASME, New York, 1985, 180-185.

[62] A.T. Alpas, J. Zhang, Wear, 155 (1992), 83-104

[63] B. Terry, G. Jones, Metal Matrix Composites, Elsevier Advanced Technology, (1990), 1533-1543.

[64] D. Charles, Met. Mater. 6 (1990), 78-82.

[65] A.T. Alpas, J. Zhang, Scripa Metallurgica et Materialia, vol. 26 (1992), 505-509.

[66] P. Rohaatgi, J. Met., 43 (1991), 10-15.

[67] J. Zhang, A.T. Alpas, Materials Science and Engineering, A161 (1993), 273-284.

[68] O.P. Modi, B.K. Prasad, A.H. Yegneswaran, M.L. Vaidya, Material Science and Engineering, A151 (1992), 235-245.

[69] A. Wang, H.J. Rack, Material Science and Engineering, 147 (1991), 211-224.

[70] P.K. Rohatgi, S. Ray, Y. Liu, International Materials Reviews, vol. 37 (1992), No 3, 129-150.

[71] S. Das, S.V. Prasad, T.R. Ramachandran, Materials Science and Engineering, A138 (1991), 123-132.

[72] A.K. Jha, S.V. Prasad, G.S. Upadhyaya, Wear, 133 (1989), 163-172.

[73] M.A. Moore, R.C. D. Richard and D.G. Attwood, Metall. Trans. 3A (1972) 2485-2491.

[74] M.M. Haque, M.A. Maleque, J. of Materials Processing Technology, 77 (1998), 122-128

[75] U. Bischofberfer, g. Neite, H.E. Exner, Key Engineering Materials, 333 (1990), 44-45.

[76] A.R. Riahi, T. Perry, A.T. Alpas, Material Science and Engieering A 343 (2003) 76-81.

[77] N. Tenekedjiev, H. Mulazimoglu, B. Closset, J. Cruzleski, Microstructures and Thermal Analysis of Strontium-Treated Aluminum-Silicon Alloys, American Founrymen's Society, Inc.,1350

74

Appendix A: Data Tables

Table 3.1 Chemical composition (%wt) of GM 396 Al-Si alloys

Si	Cu	Mg	Fe	Ni	Mn	Zn	Sr	Ti
13.2	2.3	0.34	0.13	0.01	0.32	0.01	0.017	0.01

Table 3.2 Material designation, processing procedures of GM396 alloys

Materials		Casting Method	Heat Treatment
GM Designation	Designation used in Work		
1758-S	A13-S	Silica sand	none
1758-Z	A13-Z	Zircon-sand cast	none
39-7	A13-C-T6	Chilled cast	T6
40-7	A13-S-T6	Silica-sand cast	T6
---	A13-S-T6-AN	As A13-C-T6	350 °C, 10 min, furnace cooled

75

Table 4.1 Summary of Si particle aspect ratio, size, bulk hardness and Al matrix hardness

Alloys	Average Si aspect ratio	Average Si particle size (μm^2)	Average Hardness	
			Si rich area (1kgf,Vicker's)	Matrix (10gf, knoop)
A13-Z	4.2	111.7	712.64	52.4
A13-S	4.4	126.7	681.1	48.7
A13-C-T6	2	18.4	720.9	63.3
A13-C-T6-AN	1.9	19.1	706.4	47.2
A13-S-T6	2.1	21.6	715.5	58.5
6061 Al	---	---	---	54.3

76

Table 4.2 Maximum and mean Hertzian contact pressure as a function of load

	Load (N)	0.25	0.5	1	2	3	5
52100 steel ball (2 mm Dia.)	P_{max} (GPa)	0.56	0.71	0.89	1.12	1.29	1.51

Poison's ratio of steel:0.29, Poison's ratio of Al: 0.35; Young's Modulus of steel-210 GPa, Al-70 GPa.

Table 4.3 Summary of results of single-pass scratching tests

Materials	Si fracture (%)	COF	Scratch track width (μm)			Scratch track depth (μm)		
			Max.	Min.	Ave.	Max.	Min.	Ave.
A13-S (dry, 0.5N)	56	0.08	48.0	28.1	38.1	0.275	0.275	0.386
A13-C-T6 (dry, 0.5N)	37	0.08	24.8	16.5	20.7	0.143	0.143	0.285
A13-S (Lub. 5N)	90	0.13	135.8	122.6	129.2	0.47	0.47	0.918
A13-C-T6 (Lub. 5N)	36	0.13	94.3	75.2	84.6	0.357	0.357	0.669

77

Table 4.4 Wear track of A13-S and A13-C-T6 from reciprocating wear tests

Alloys	Wear track width (μm)			Wear track depth (μm)		
	Max.	Min.	Ave.	Max.	Min.	Ave.
A13-S (Lub. 1.2N)	448.8	414.1	431.5	1.586	0.807	1.197
A13-C-T6 (Lub. 1.2N)	312.0	221.5	266.7	0.872	0.564	0.718

Roughness of A13-S and A13-C-T6: 0.2-0.1μm (outside); 0.03-0.04 μm (on track)

78

Table 5.1 Composition, ceramic particle size and hardness of the test liner materials. For all samples consisting of graphite, the average graphite particle size is: length = $102.3 \pm 8.3\mu m$, width = 48.0 ± 18.8 μm

Materials (Cylinder liners)	Al_2O_3 particles size (μm)		Hardness HV_{1kg} (Kg/mm^2)
	Length	Width	
5A3G (F): A356 Al-5vol.% Al_2O_3 (fine)-3vol.% graphite	13.4 ± 3.8	8.9 ± 1.6	76.1 ± 3.6
5A3G (C):A356 Al-5vol.% Al_2O_3 (coarse)-3vol.% graphite	22.9 ± 4.3	10.3 ± 5.1	99.6 ± 2.8
5A5G :A356 Al-5vol.% Al_2O_3 (fine)-5vol.% graphite	13.1 ± 3.0	7.7 ± 1.5	81.1 ± 4.6
3A5G:A356 Al-3vol.% Al_2O_3 (fine) 5vol.% graphite	14.0 ± 3.5	7.4 ± 1.9	79.4 ± 5.5
0A5G (F):A356 Al-0vol.% Al_2O_3 (fine)-5vol.% graphite	---	---	66.4 ± 3.7

79

Appendix B: Figures

Pin on Disk

(a)

Block on Ring

(b)

Normal Load

Direction of Motion

Sample

(c)
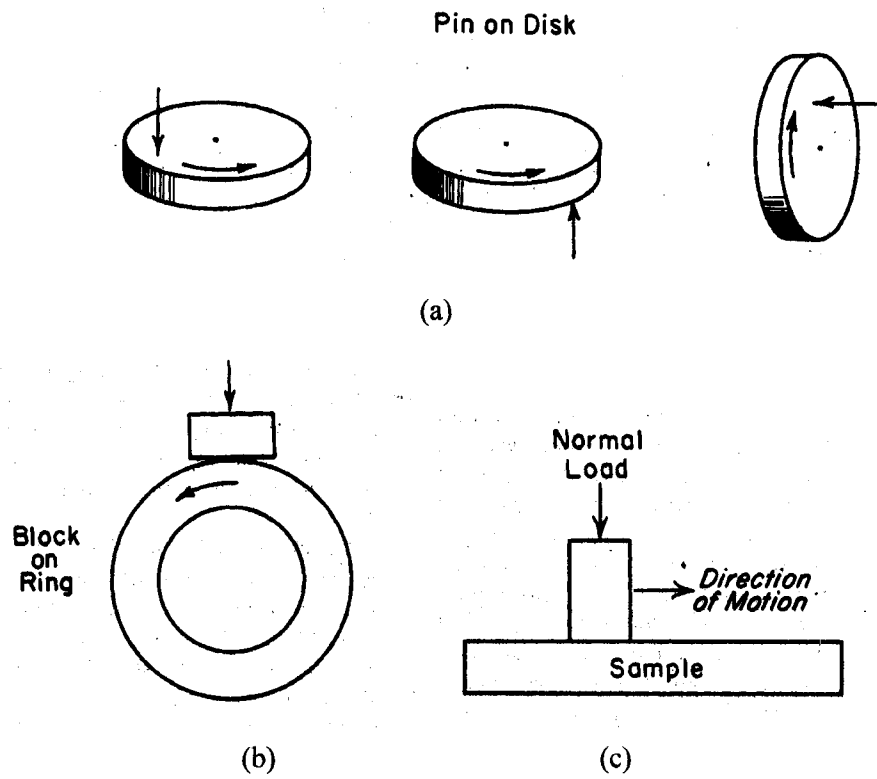
Figure 2.1 The pin-on-disk wear test machine [16]: a) three different arrangements for a simple pin-on-disk wear test machine; b) block-on-ring wear machine; c) reciprocating wear machine.

80
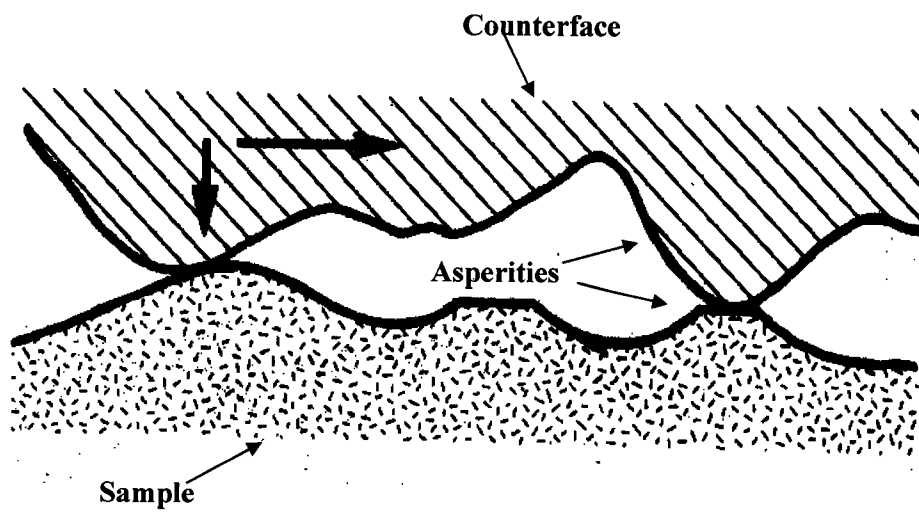
Figure 2.2 Two sliding surfaces contact by asperities. [9]

81

(a)

(b)

82
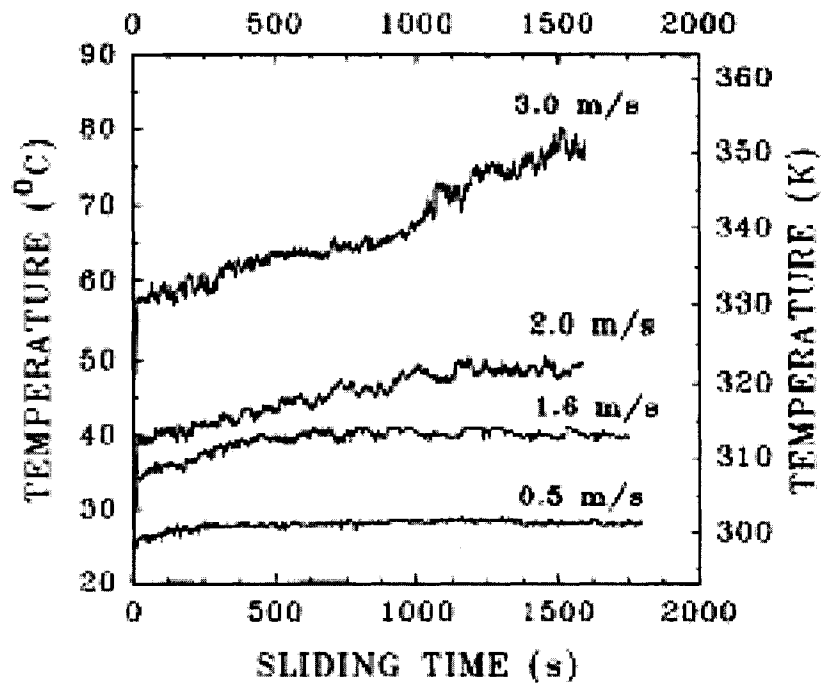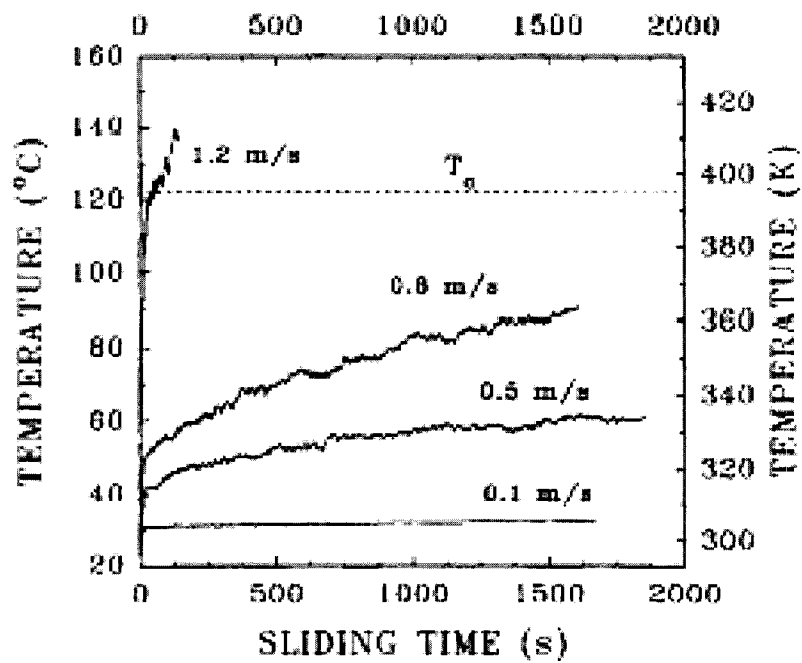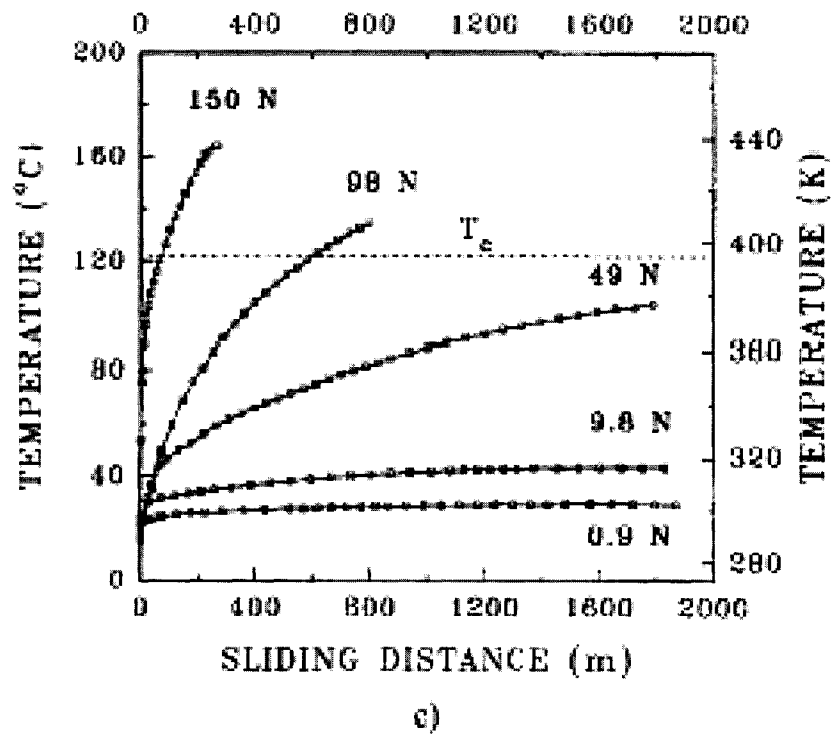
Figure 2.3 (a) Contact surface temperature versus sliding time plots at different velocities at a constant load of 5.0 N; (b) contact surface temperature versus sliding time plots at 50N; (c) contact surface temperature versus sliding distance plots at different loads at a constant sliding velocity of 0.8m/s; [22].

83
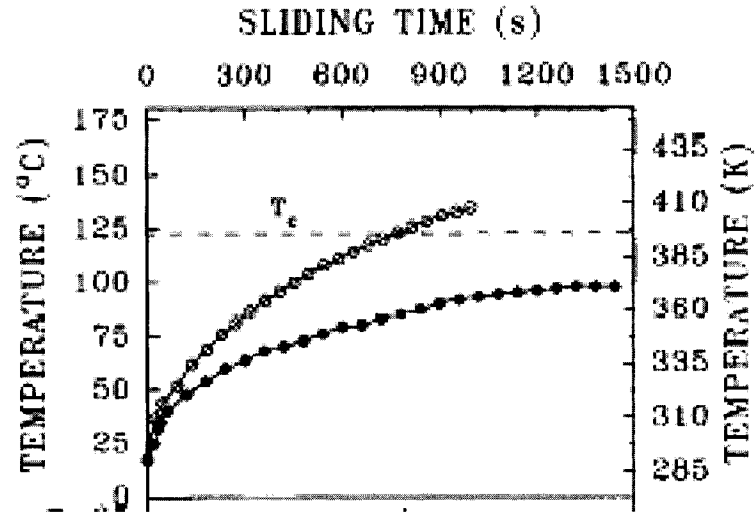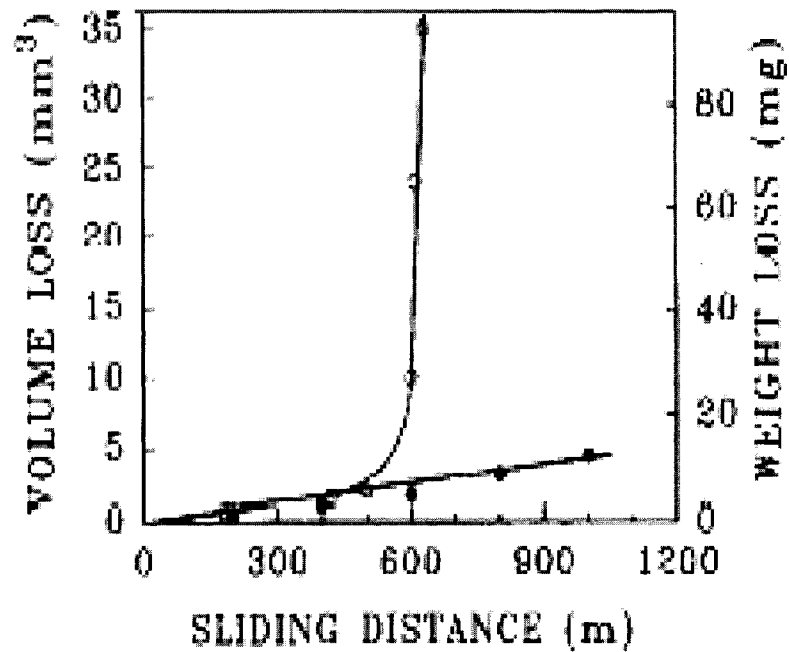
Figure 2.4 (a-b) Effect of forced cooling by chilled water on the mild to severe wear transition in 6061 Al worn against SAE 52100 steel. Without cooling the contact temperature exceeds T_c (395k) leading to severe wear (o). Cooling the system will ensure that the contact surface temperature stays below 395k, thus only mild wear is observed (●). Load =98N, v=0.8m/s. [22]

84
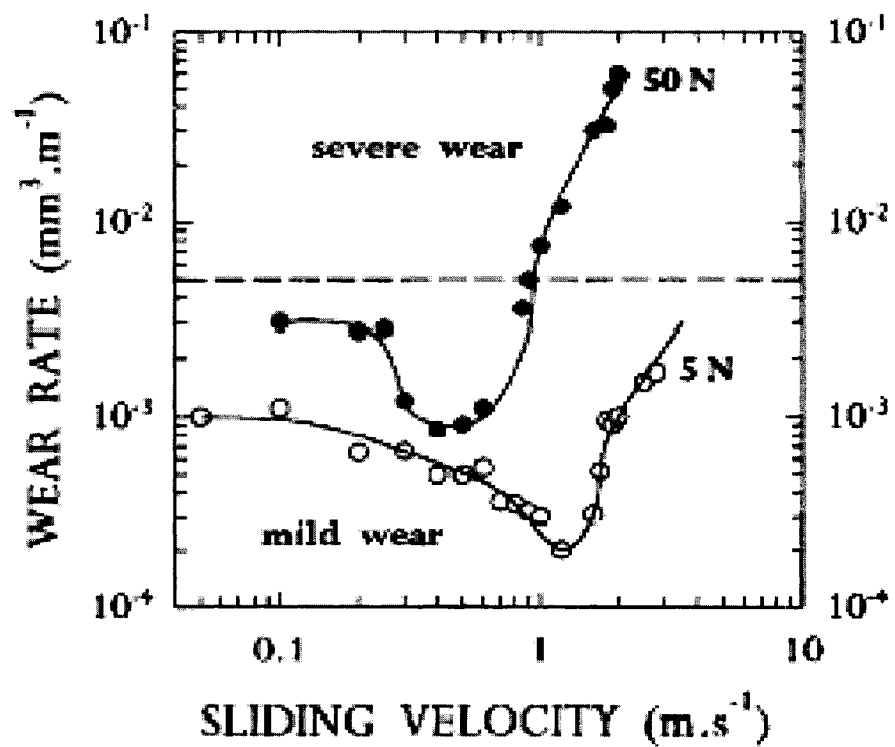
Figure 2.5 Wear rate versus sliding speed diagram for tests performed at two contact loads: 5.0N (o) and 50.0N (●). [22]

85
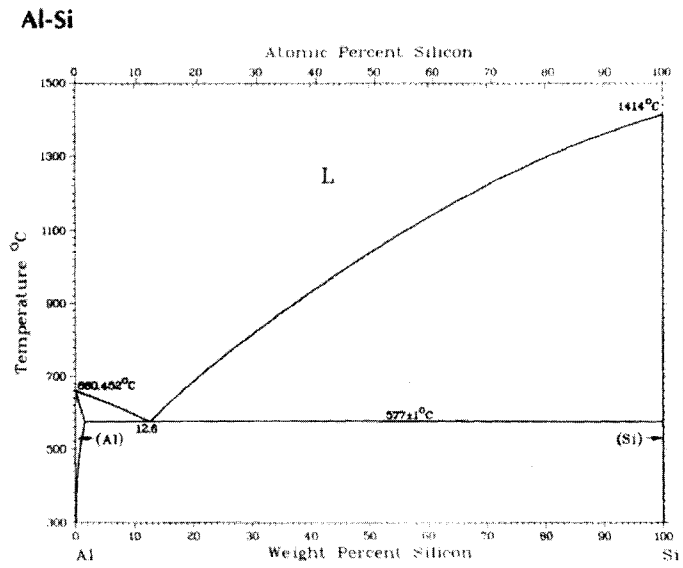
Al-Si

Figure 2.6 Phase diagram of Al-Si alloy system

86
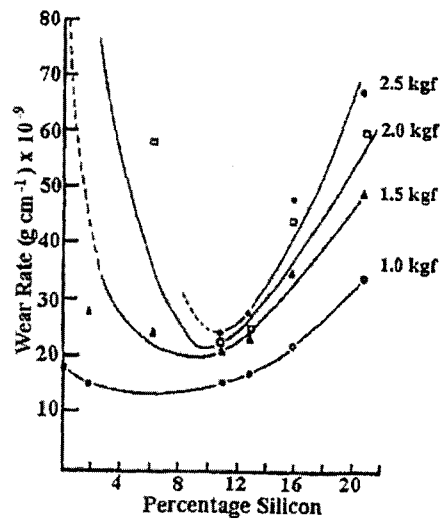
Figure 2.7 Wear rate as a function of Si Addition for Al-Si alloys subjected to dry sliding. [53].
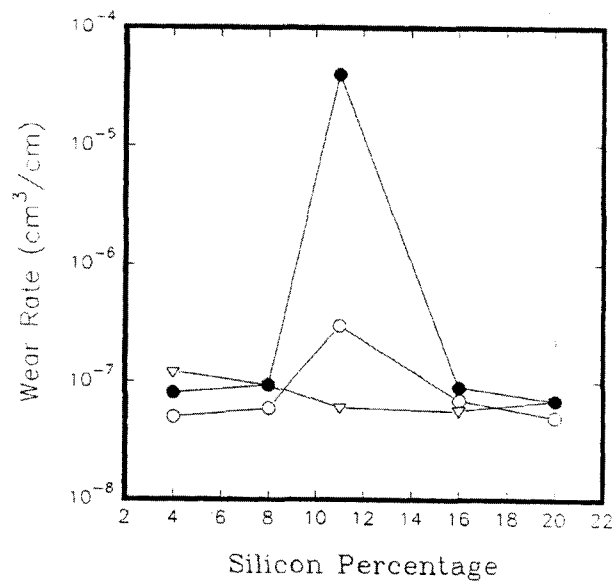
Figure 2.8 Wear rate as a function of Si content worn against steel at 1m/s, 10N (o), 20 N (•) AND 60N (Δ) load [3].

87
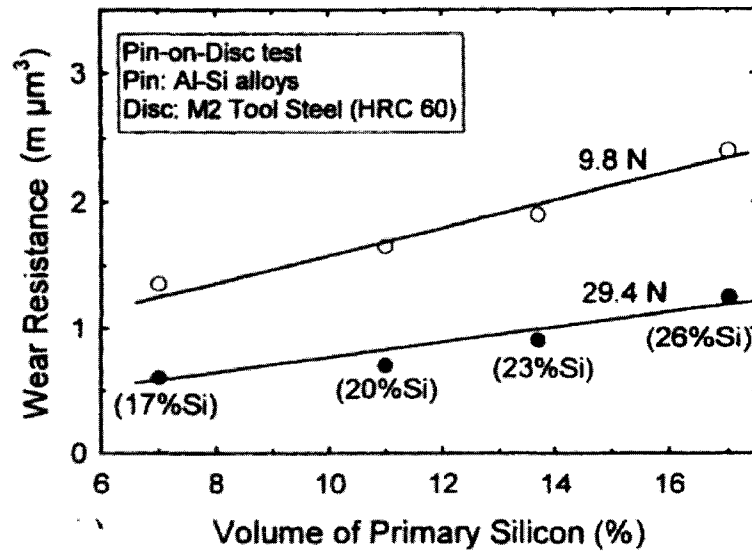
Figure2.9 Effect of Silicon content in hypereutectic Al-Si alloys on wear, from pin-on-disk tests sliding against hard steel (figures in brackets denote total silicon content) [55].

88
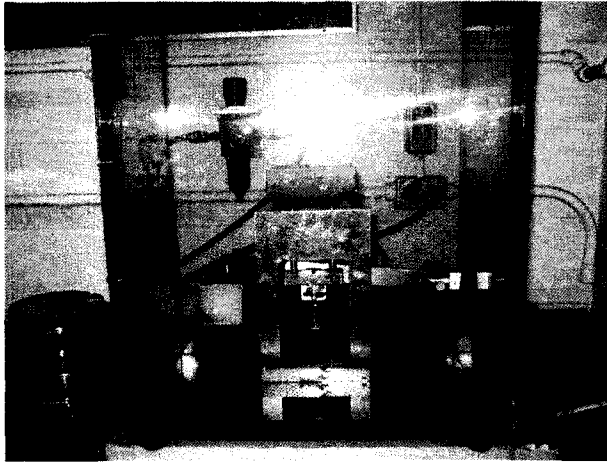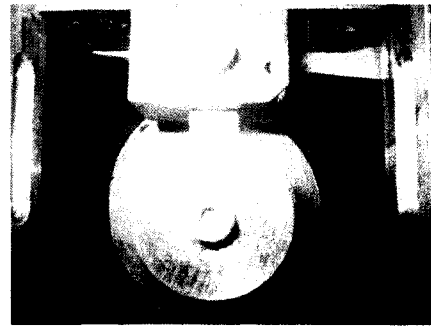
(a)   (b)

Figure 3.1 The block-on-ring Wear machine. a) A general view of the machine; b) the block-on-ring configuration.

89
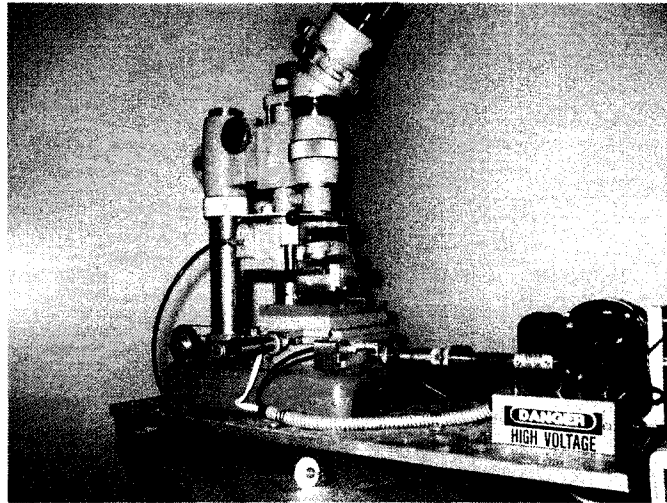
(a)
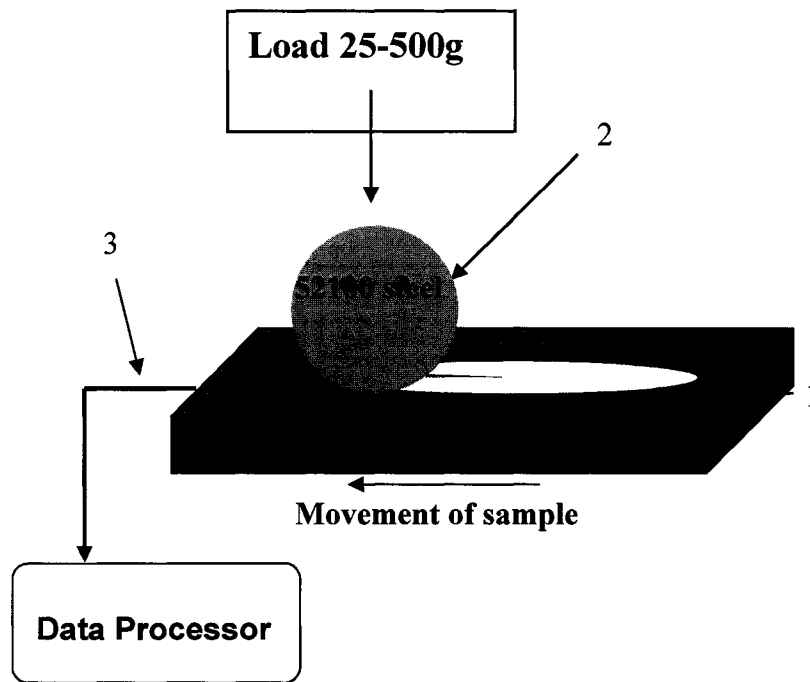
(b)

Figure 3.2 The Scratch Tester (1-movable sample; 2-stationaly indenter; 3-load cell). a) A general view of the scratch tester; b) a schematic show of the tester.

90

(a)
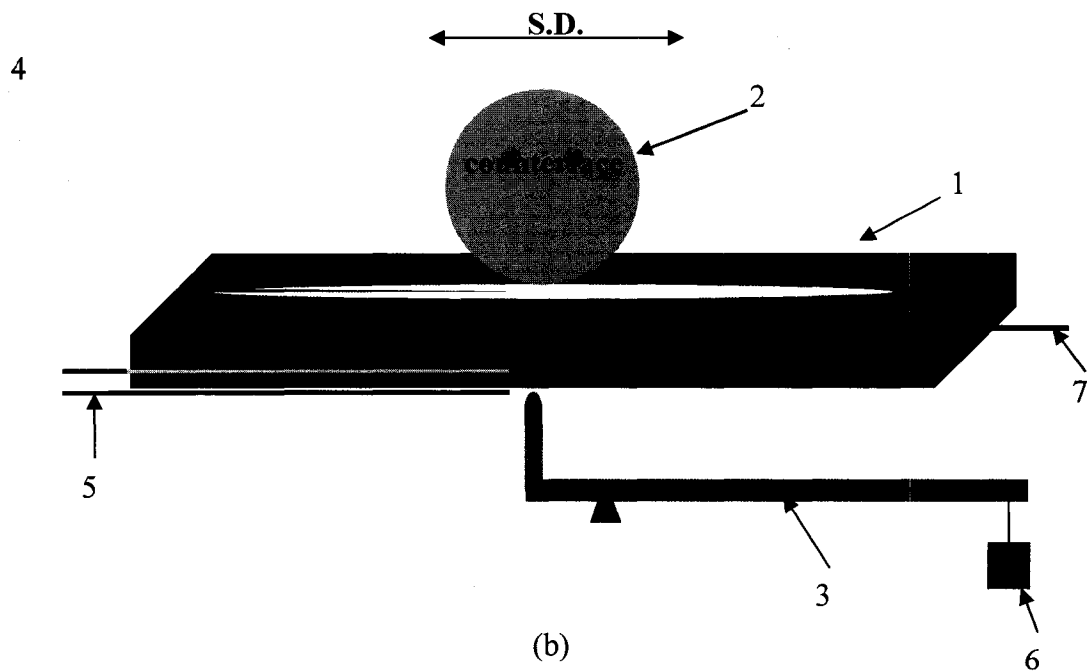
(b)

Figure 3.3 The reciprocating wear tester (1-stationary sample; 2-counterface; 3-loading arm; 4-oil reservoir; 5-thermalcouple; 6-load; 7-cartridge heater). a) A general view of the reciprocating wear tester; b) a schematic show of the reciprocating wear tester.

91
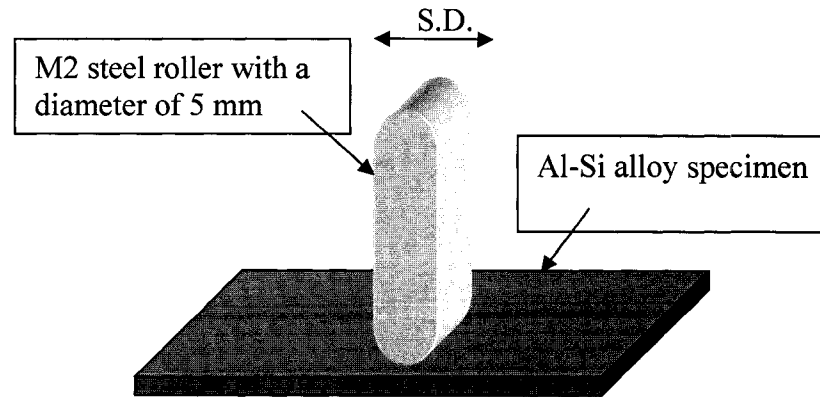
Figure 3.4 Contact configuration of Al-Si alloy scuffing tests
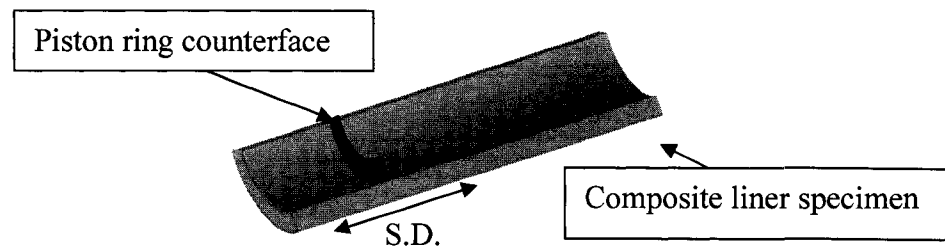
Figure 3.5 Contact configuration of Al-Si based composites scuffing tests

92
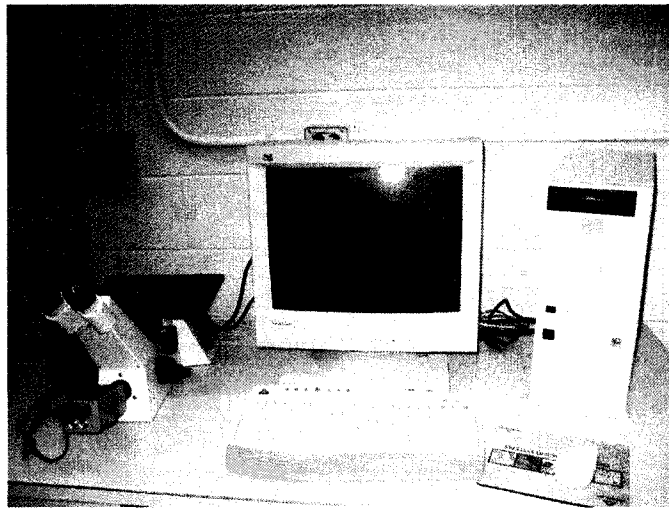
Figure 3.6 Buehler Digital Image Analyzer Model 2002

93
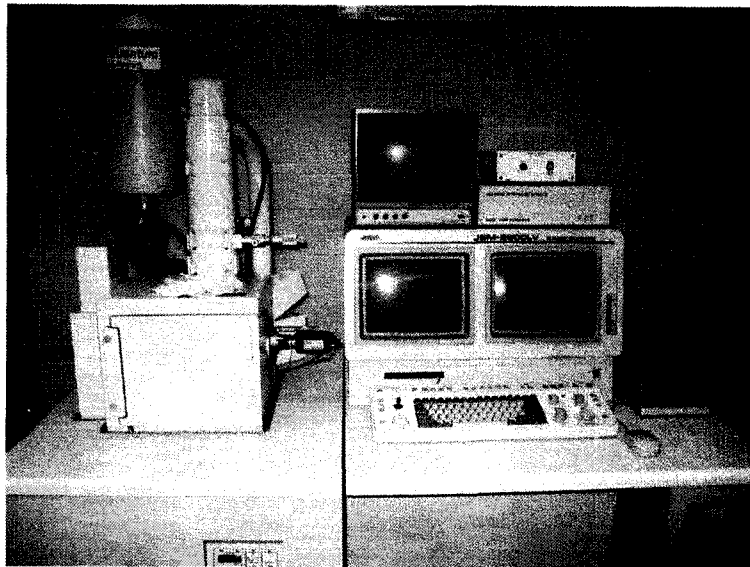
Figure 3.7 Scanning Electron Microscope (Jeol Model JSM-5800 LV)

94

Figure 3.8 Buehler Microhardness Tester

95
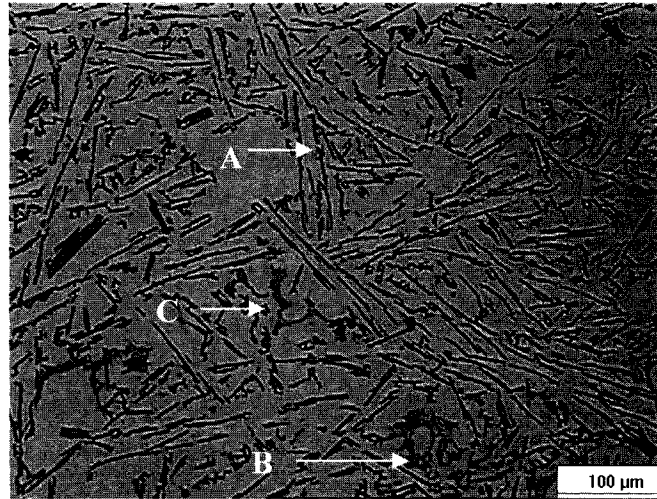
Figure 4.1 General optical image of the microstructure of A13-S alloy [A: Needle-shaped eutectic Si particles, B: $Al_{15}(FeMn)_3Si_2$ phase, C: Al_2Cu eutectic phase]
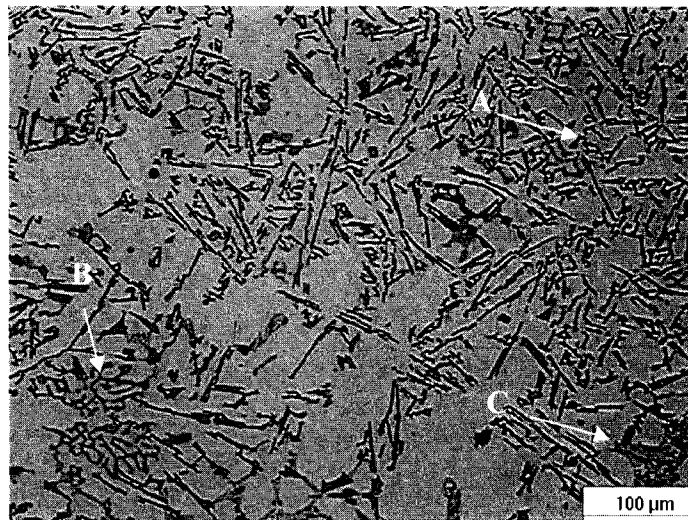
Figure 4.2 General optical image of the microstructure of A13-Z alloy [A: Needle-shaped eutectic Si particles, B: $Al_{15}(FeMn)_3Si_2$ phase, C: Al_2Cu eutectic phase]

96
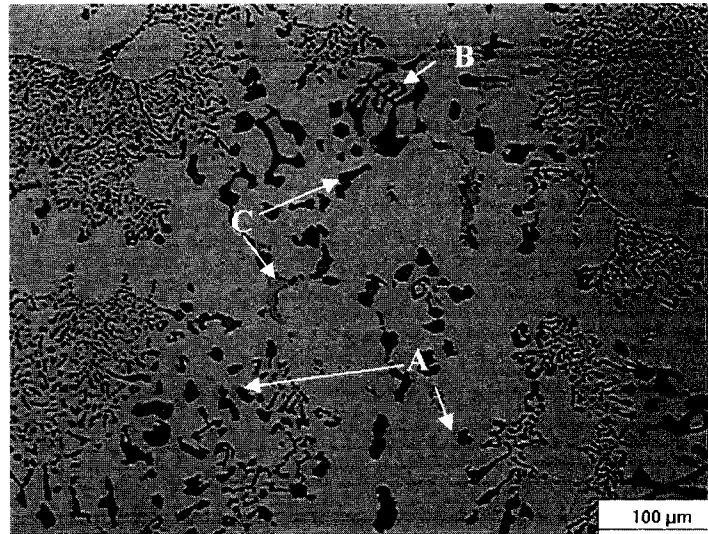
Figure 4.3 General optical image of the microstructure of A13-C-T6 alloy [A: Round-shaped eutectic Si particles, B: $Al_{15}(FeMn)_3Si_2$ phase, C: Al_2Cu eutectic phase]
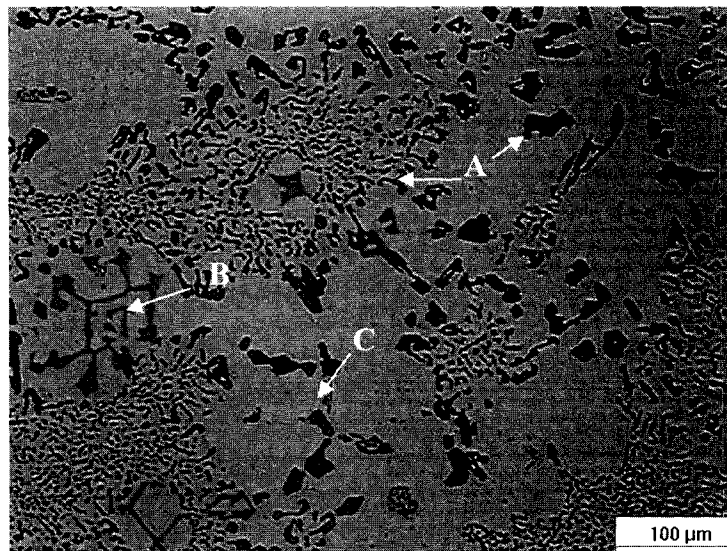
Figure 4.4 General optical image of the microstructure of A13-S-T6 alloy [A: Round-shaped eutectic Si particles, B: $Al_{15}(FeMn)_3Si_2$ phase, C: Al_2Cu eutectic phase]

97
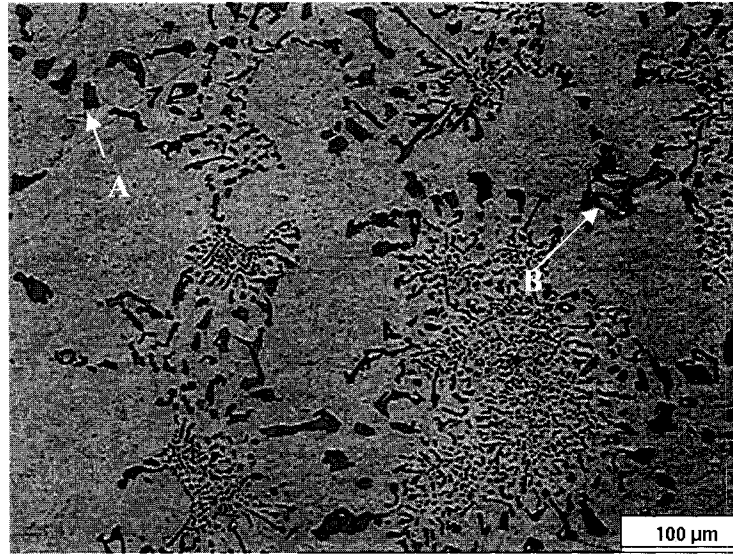
Figure 4.5 General optical image of the microstructure of A13-S-T6-AN alloy [A: Round-shaped eutectic Si particles; B: $Al_{15}(FeMn)_3Si_2$ phase]

98
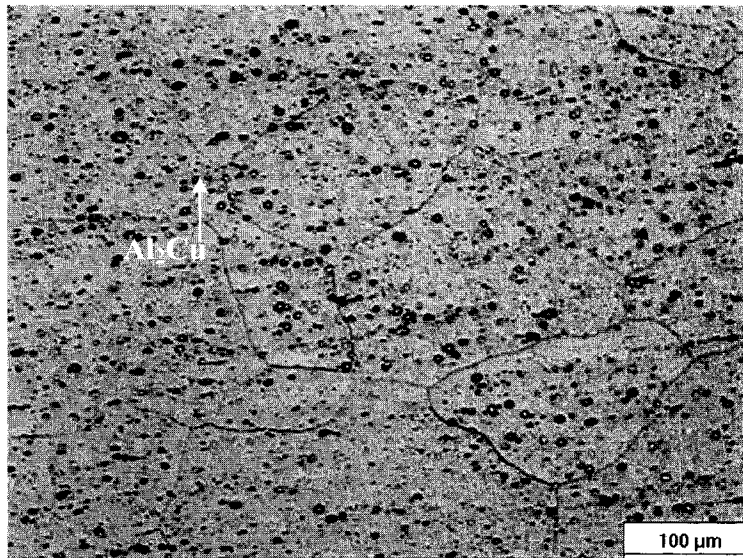
Figure 4.6 General optical image of the microstructure of the wrought 6061 Al alloy. Small particles in the matrix are Al_2Cu phase [large particles were not observed in matrix]

99
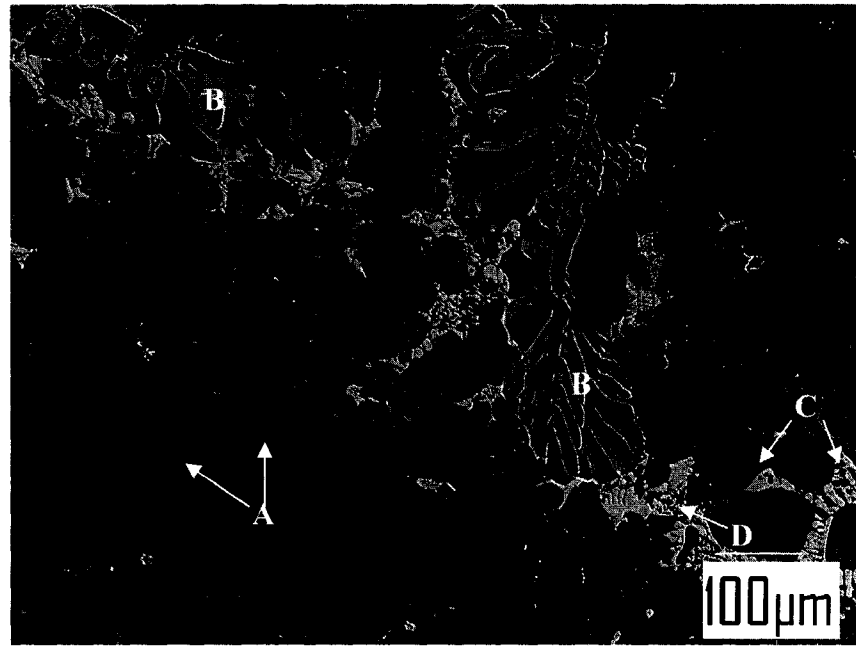
(a)
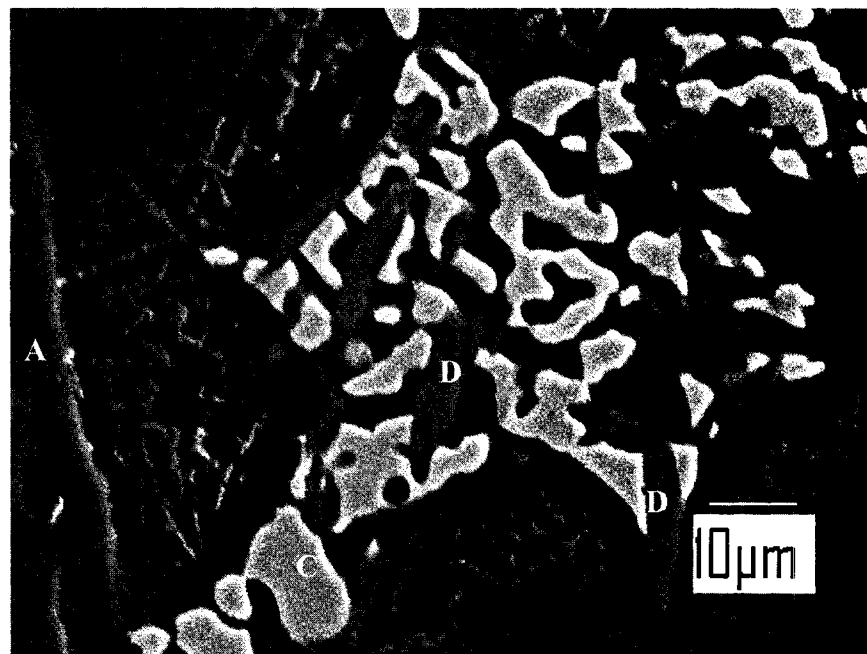
(b)

Figure 4.7 SEM microstructure shows various phases in the as-cast A13-S alloy. (a) x 200, (b) x 2000 [A: needle-shaped eutectic Si, B: $Al_{15}(FeMn)_3Si_2$ (Chinese script), C: Al_2Cu, D: needle-shaped $Al_5Mg_8Si_6Cu_2$ plates existed between Al_2Cu phase, F: Cu-Fe-Mn-Si]

100
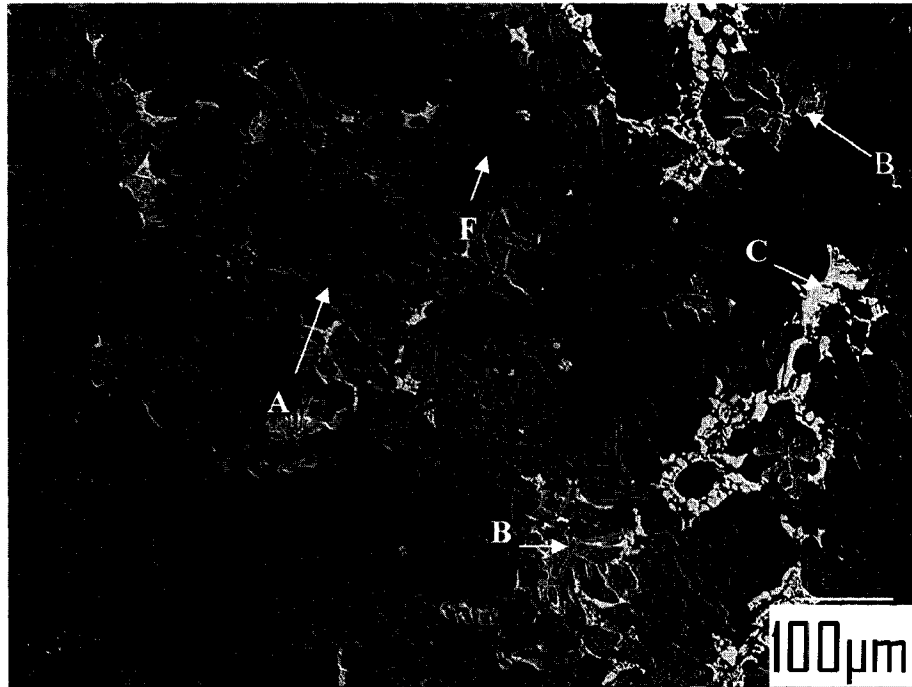
(a)
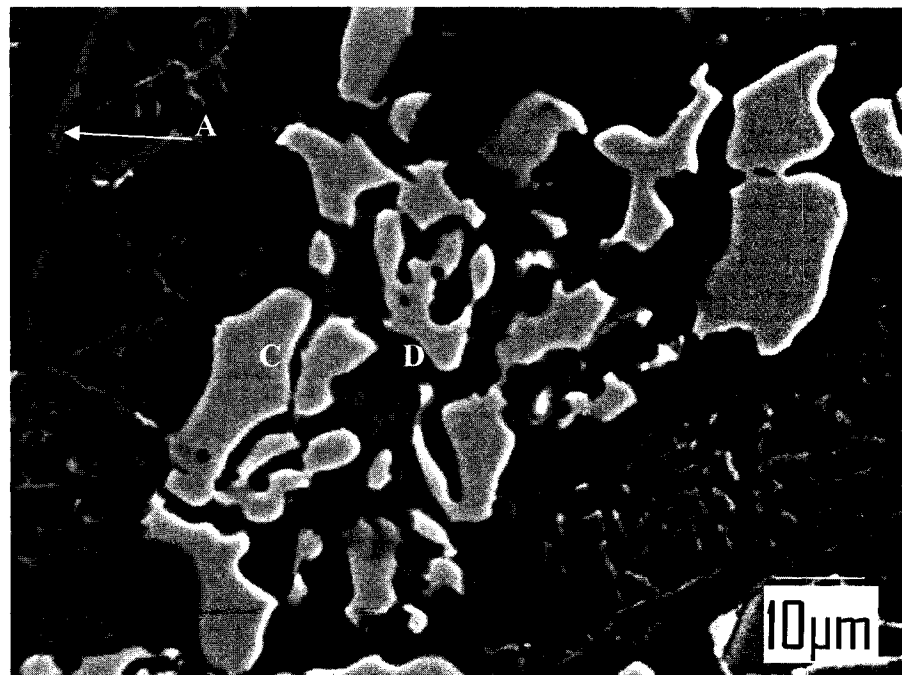
(b)

Figure 4.8 SEM microstructure showing various phases in the as-cast A13-Z alloy. (a) x 200, (b) x 2000 [A: Needle-shaped eutectic Si, B: $Al_{15}(FeMn)_3Si_2$ phase, C: Al_2Cu phase, D: rounded $Al_5Mg_8Si_6Cu_2$ plates existed between Al_2Cu phase, F: Cu-Fe-Mn-Si]

101
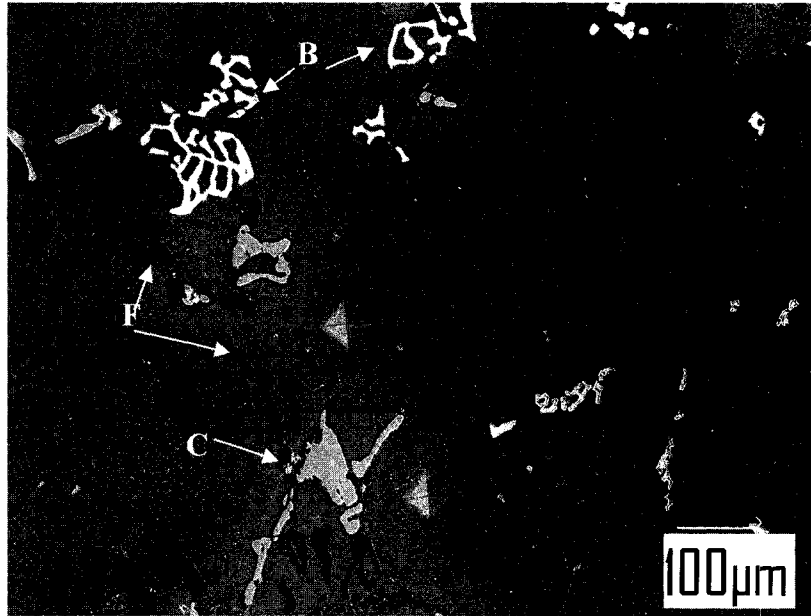
Figure 4.9 SEM microstructure showing various phases in A13-C-T6 alloy [B: $Al_{15}(FeMn)_3Si_2$ phase, C: Al_2Cu phase, F: rounded eutectic Si]

102
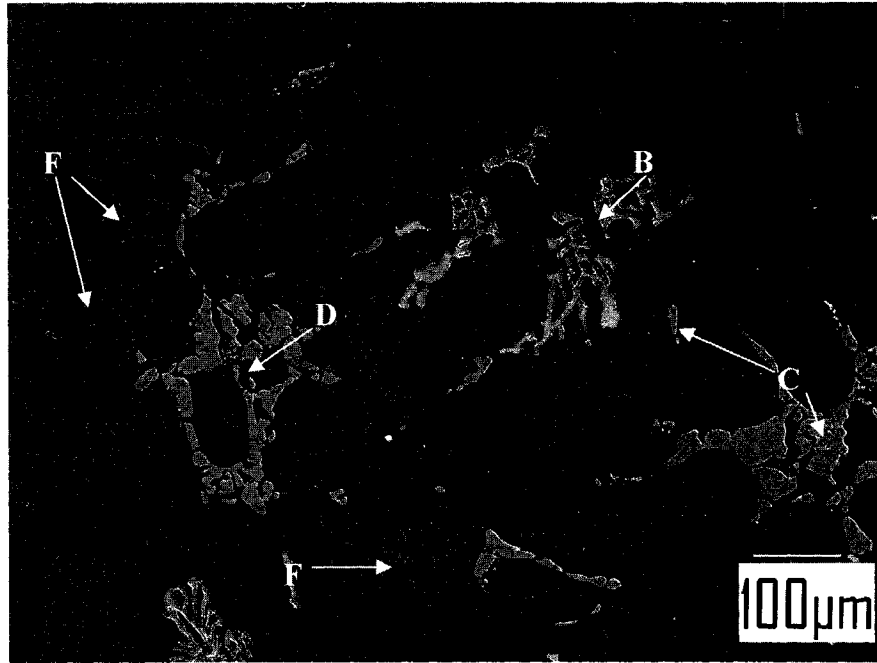
(a)
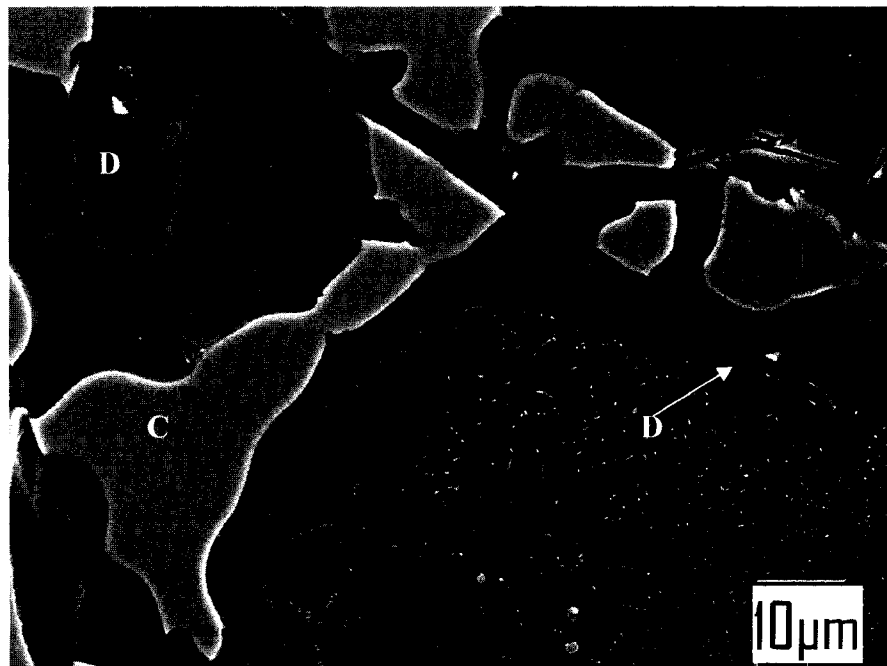
(b)

Figure 4.10 SEM microstructure shows various phases in A13-C-T6 alloy. (a) x 200, (b) x 2000 [B: $Al_{15}(FeMn)_3Si_2$ phase, C: Al_2Cu phase, D: $Al_5Mg_8Si_6Cu_2$ phase, F: rounded eutectic Si]

103
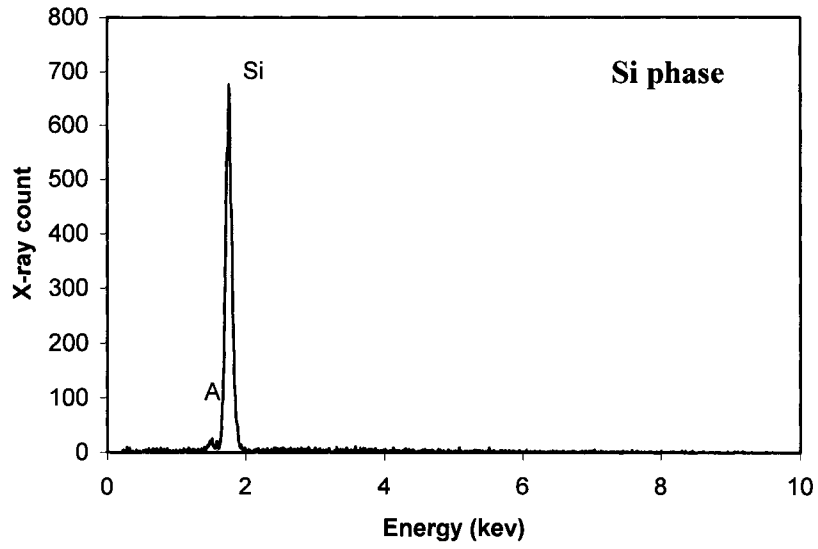
Figure 4.11 EDS spectrum of eutectic silicon (A and F)
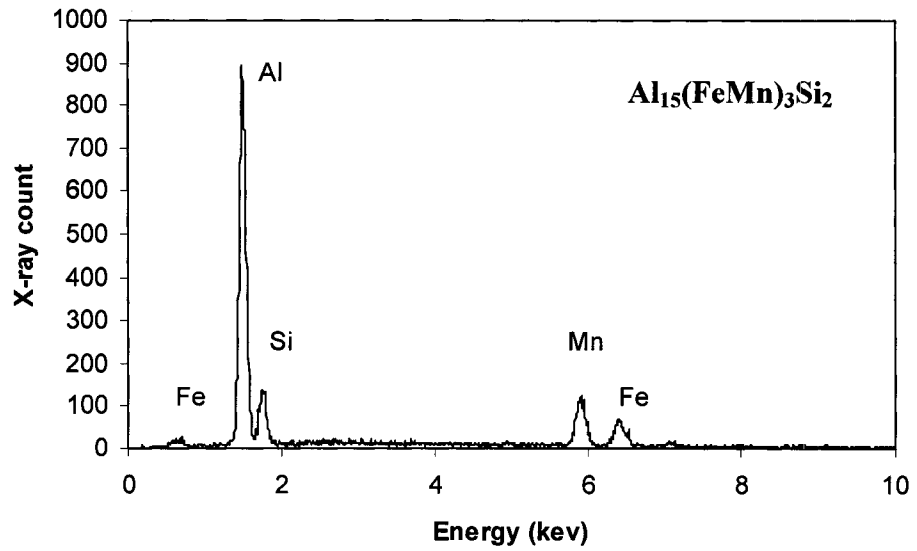
Figure 4.12 EDS spectrum of $Al_{15}(FeMn)_3Si_2$ with Chinese script (B phase).

104
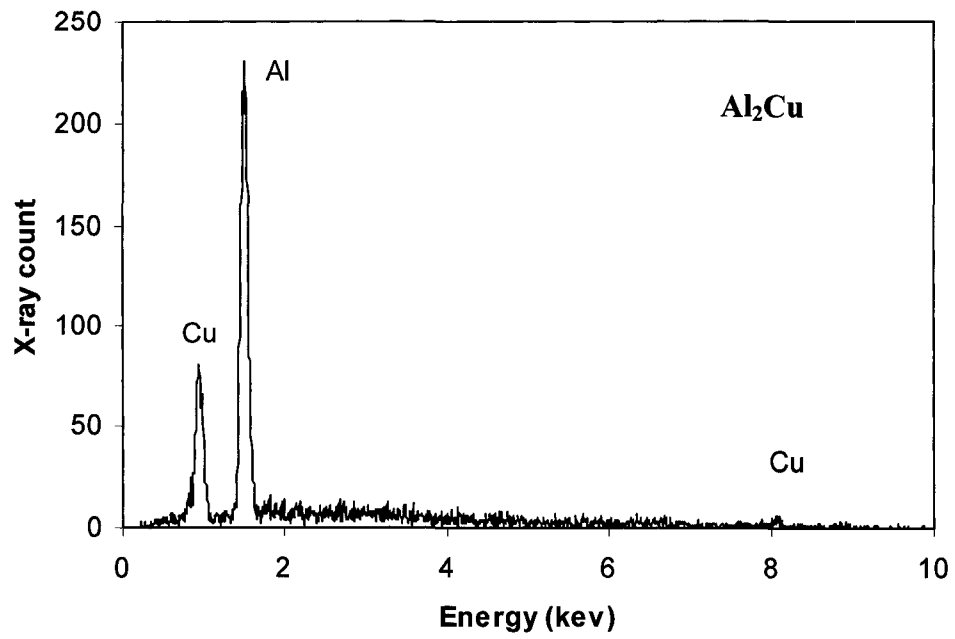
Figure 4.13 EDS spectrum of Al_2Cu (C)
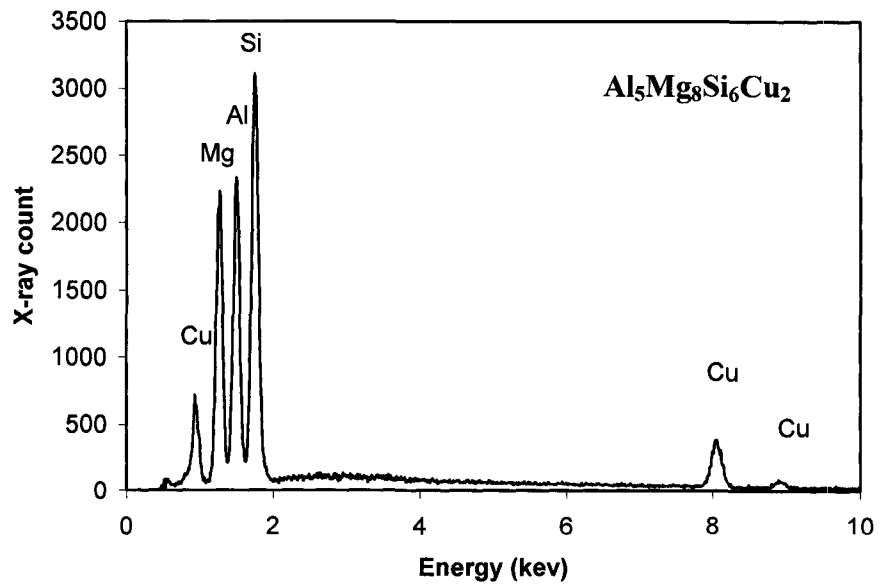
Figure 4.14 EDS spectrum of $Al_5Mg_8Si_6Cu_2$ (D phase)

105
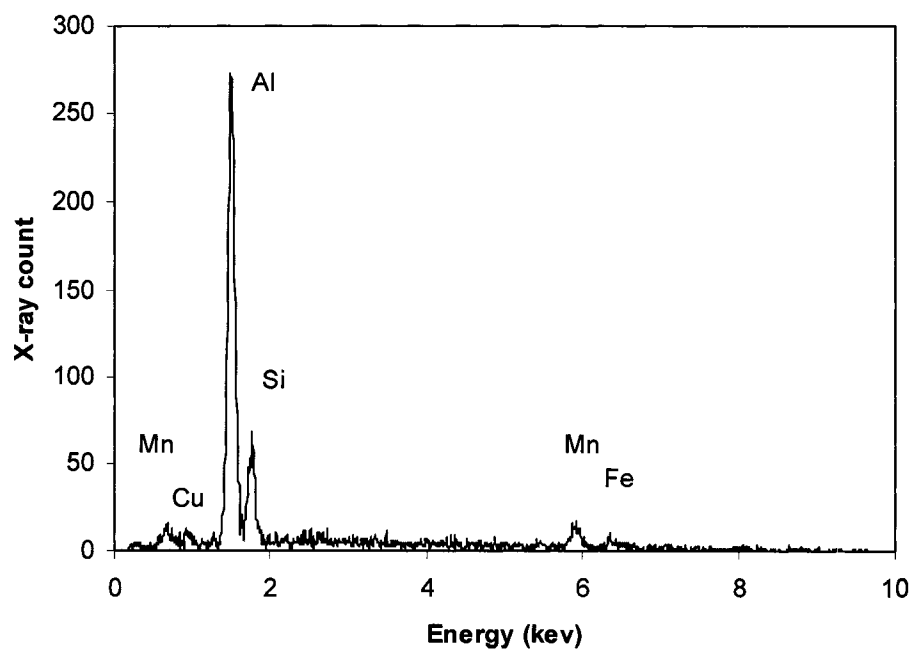
Figure 4.15 EDS spectrum of E phase [Cu-Fe-Mn-Si, formula unknow]

106
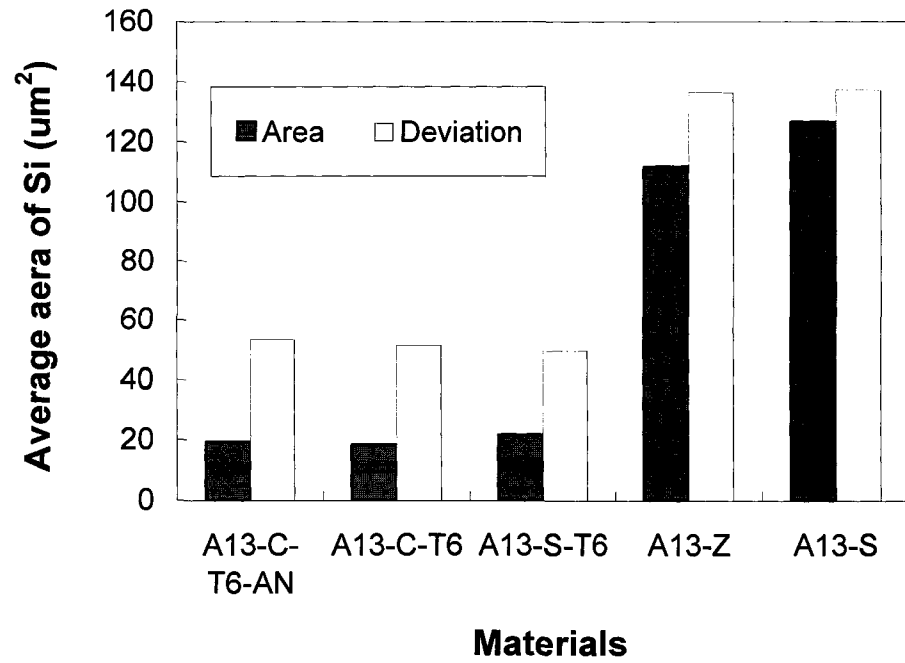
Figure 4.16 Average particle size of Si (determined by area) in the alloys
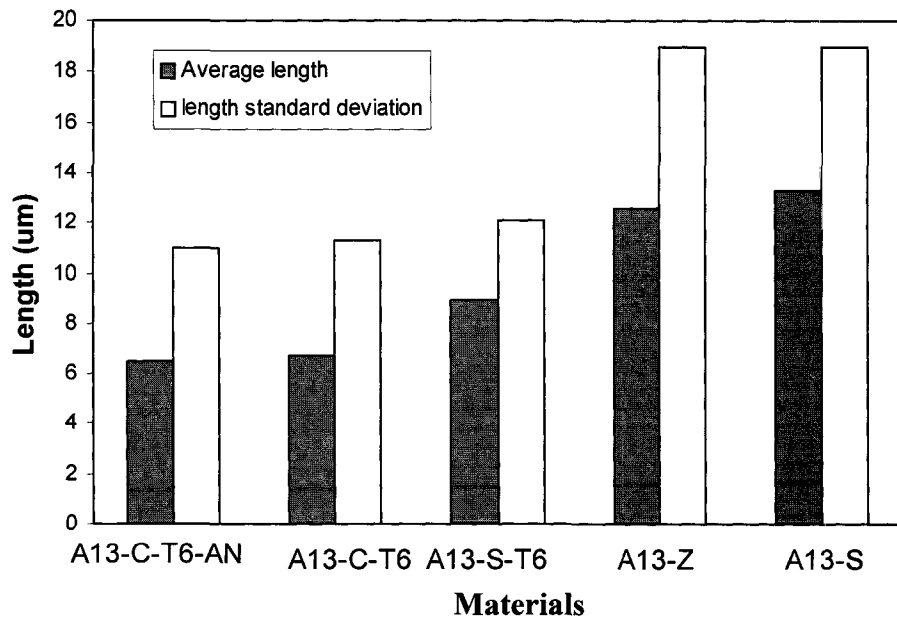
Figure 4.17 Si particle length in the alloys

107
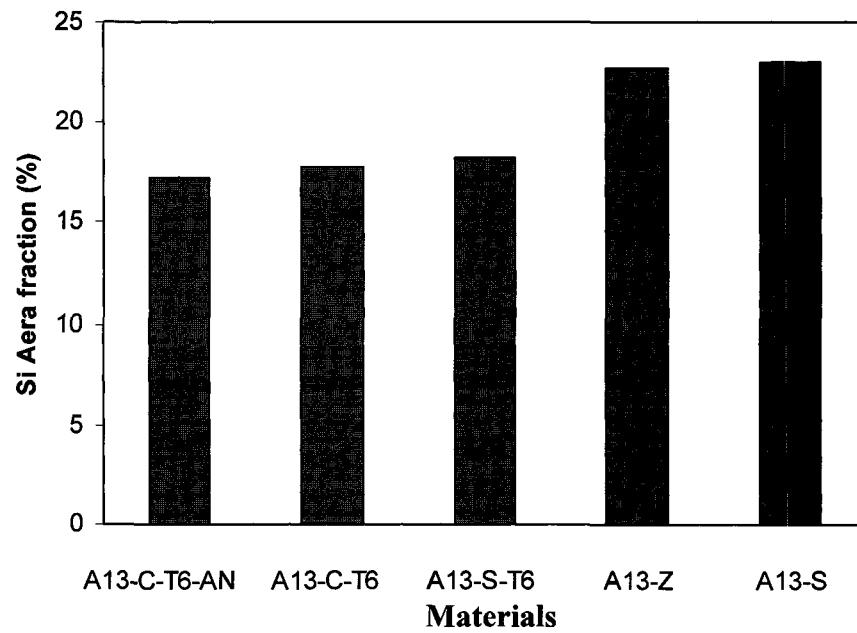
Figure 4.18 Si particle area fraction in the alloys
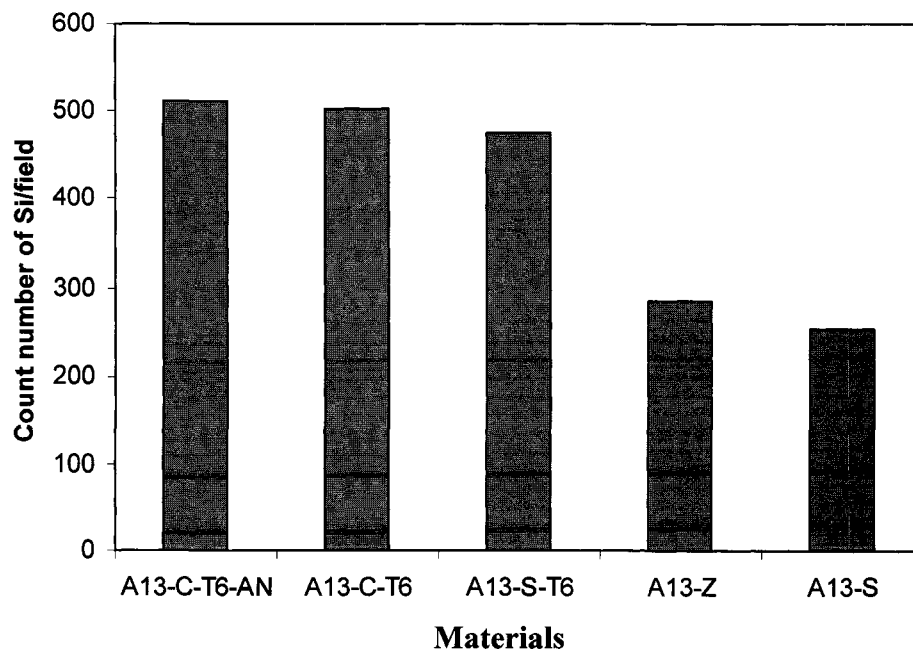
Figure 4.19 Average Si particle count number in one field (242.1μm x 181.1μm) in the alloys. (The average was taken from the count numbers in ten fields.)

108
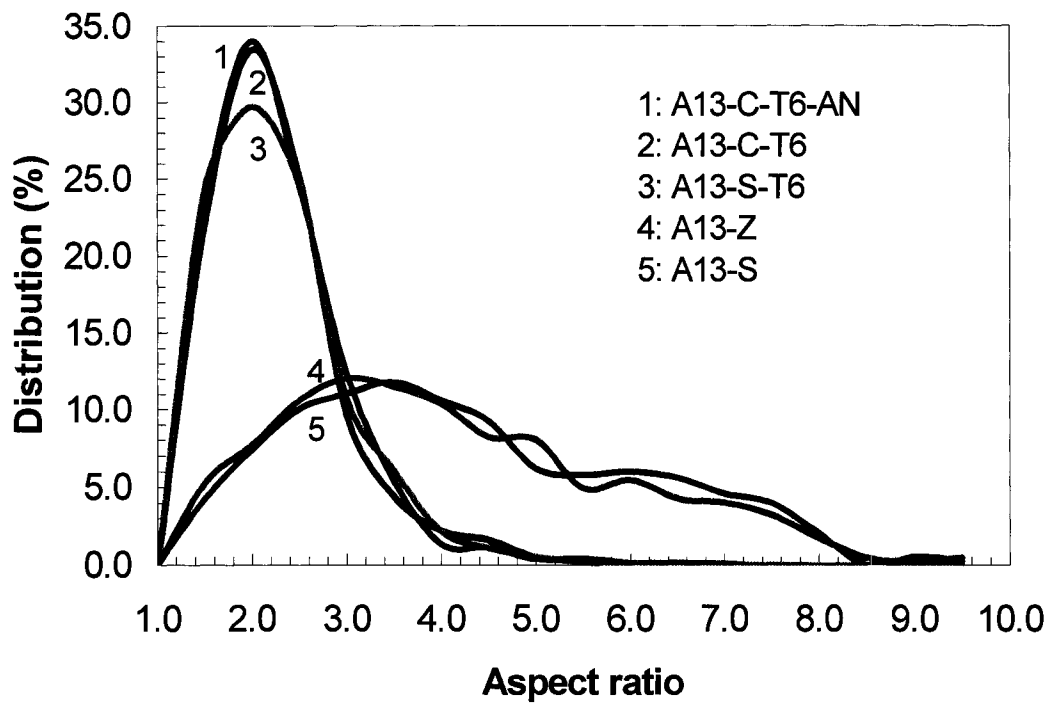
Figure 4.20 Aspect ratio distributions of Si particles in the alloys
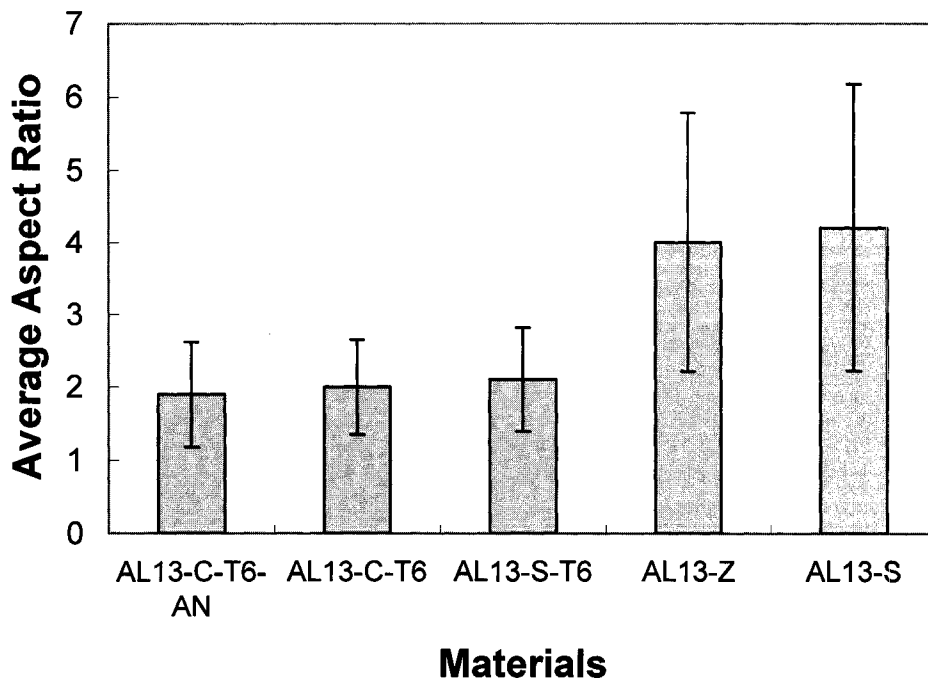
Figure 4.21 Average aspect ratio of Si particles in the alloys.

109
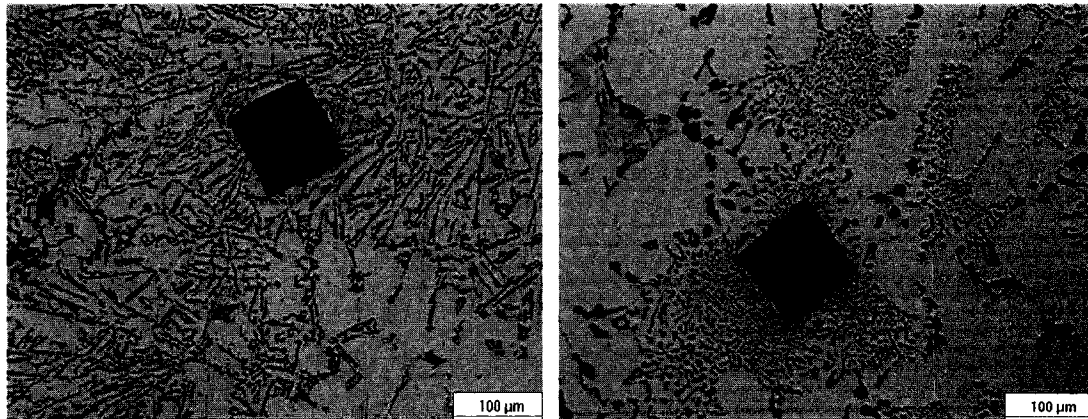
(a)   (b)
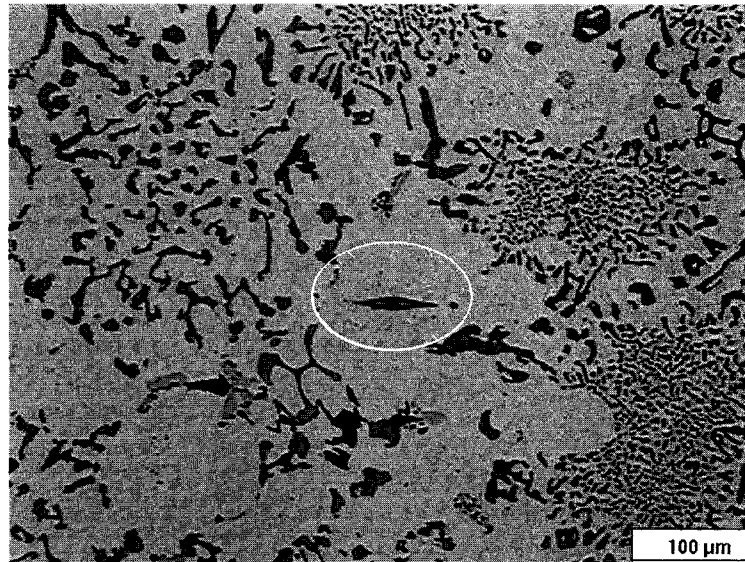
(c)

Figure 4.22 a) A Vickers indentation impression on the surface of the A13-S sample used to measure the hardness of the Si particle rich area at 1kg load; b) A Vickers indentation impression on the surface of the A13-C-T6 sample used to measure the hardness of the Si particle rich area at 1kg load; c) A Knoop indentation impression on the surface of a A13-C-T6 sample used to measure the aluminum matrix hardness at 10g load.

110
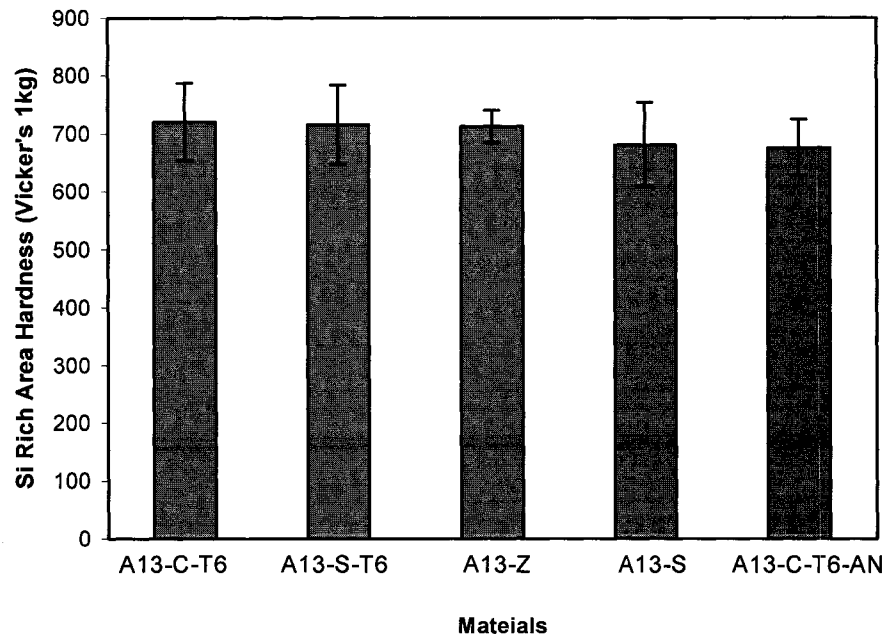
(a)
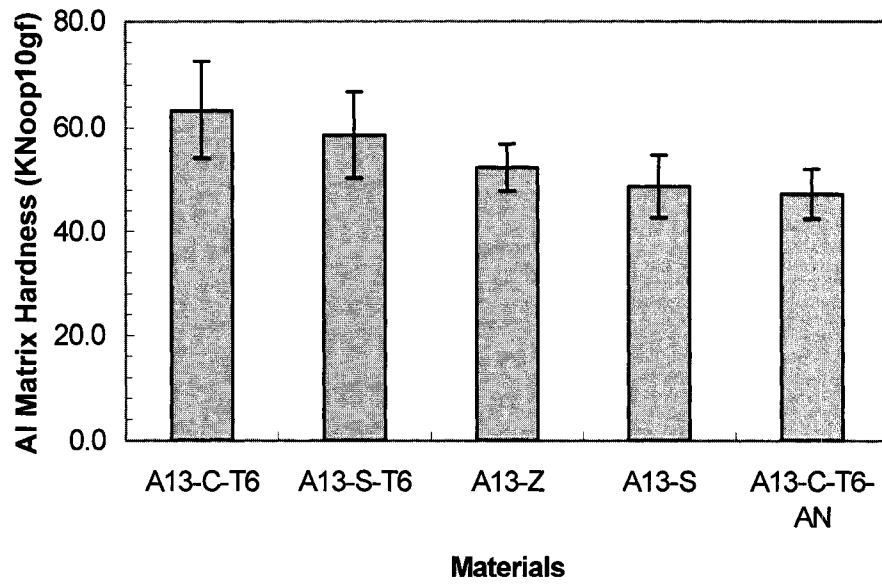
(b)

Figure 4.23- a) Bulk hardness of the alloys; b) Al matrix hardness of the alloys

111
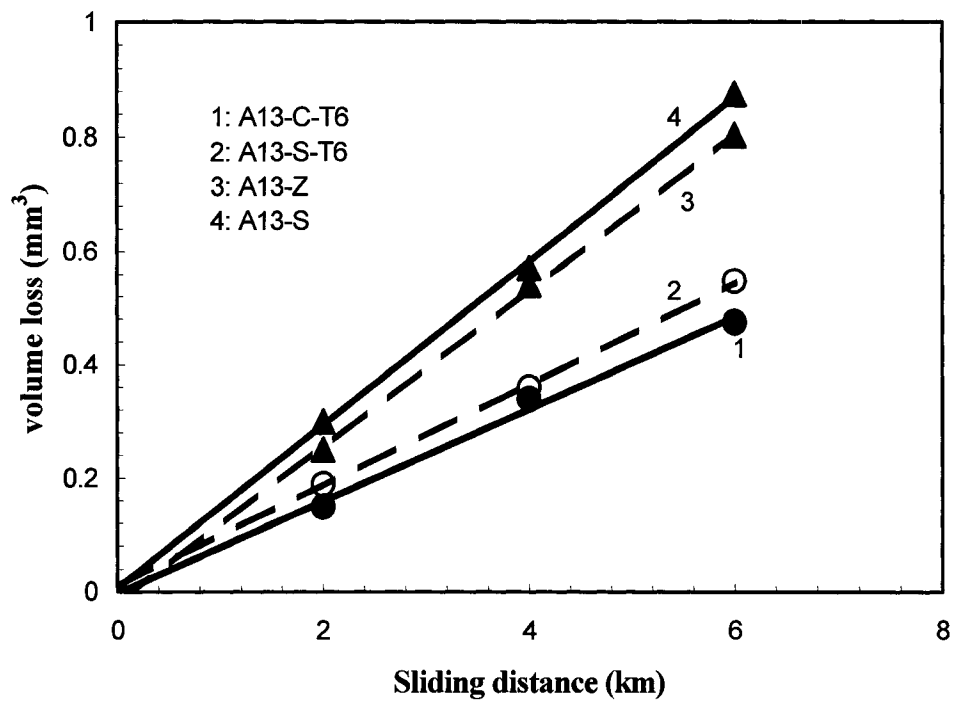
Figure 4.24 Volume loss of the four materials vs. sliding distance at 1N load and 1m/s velocity

112
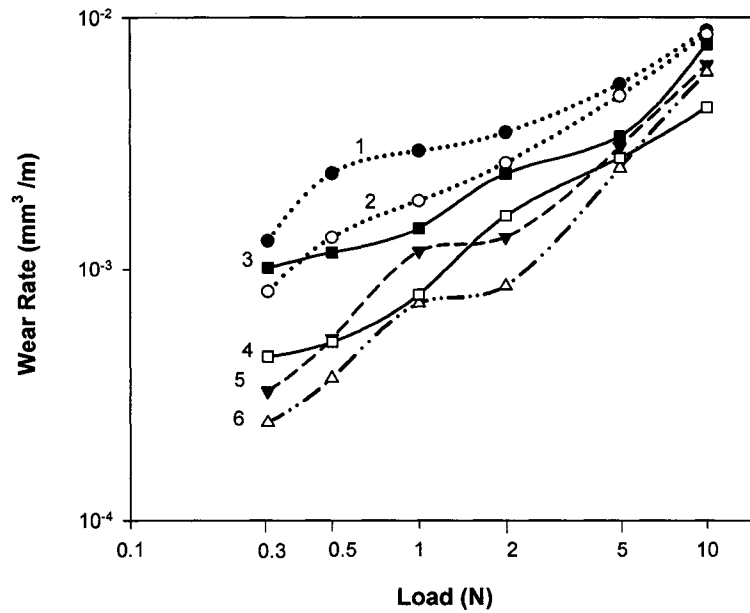
Figure 4.25 (1) Wear rates vs. load at different sliding velocities (1: Al-13-S, 2m/s; 2: Al-13-C-T6, 2m/s; 3: Al-13-S, 1m/s; 4: Al-13-C-T6, 1m/s; 5: Al-13-S, 0.2m/s; 6: Al-13-C-T6, 0.2m/s)
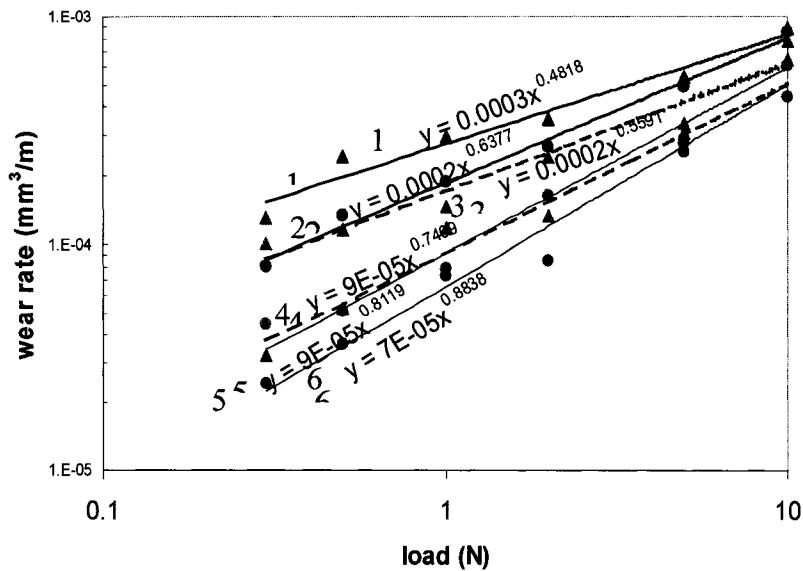
Figure 4.25 (2) Power low of volume loss of the four materials vs. sliding distance in Figure 4.25 (1). (1: Al-13-S, 2m/s; 2: Al-13-C-T6, 2m/s; 3: Al-13-S, 1m/s; 4: Al-13-C-T6, 1m/s; 5: Al-13-S, 0.2m/s; 6: Al-13-C-T6, 0.2m/s)

113
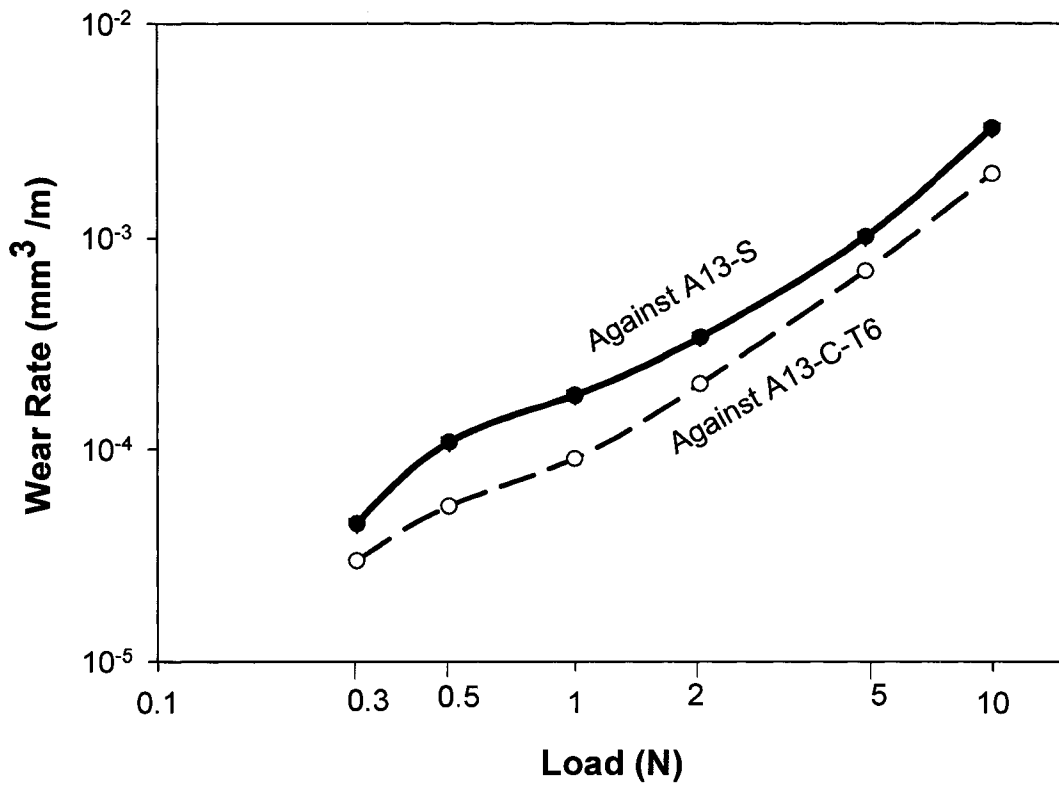
Figure 4.26 Wear rates of AISI 52100 counterface rings against A13-C-T6 and A13-S alloys.

114
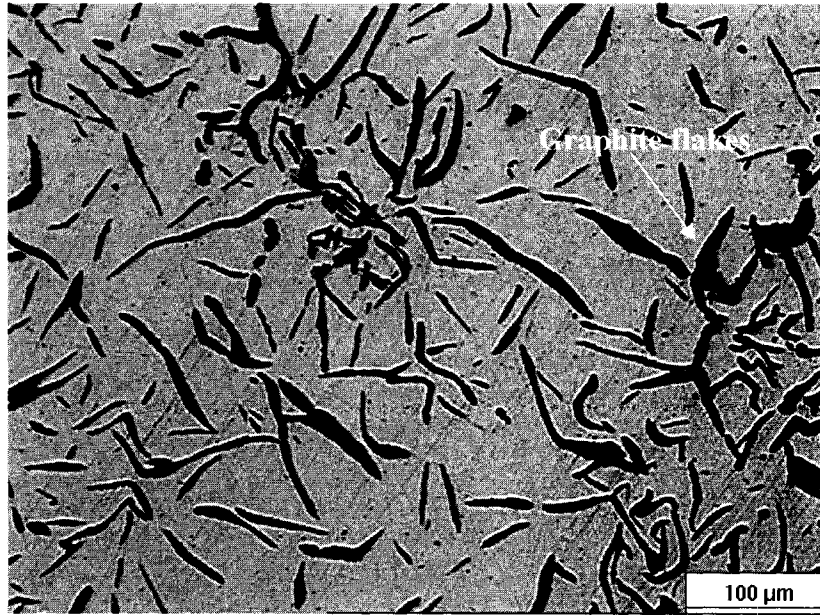
Figure 4.27 Microstructure of the AISI A40 cast iron

115
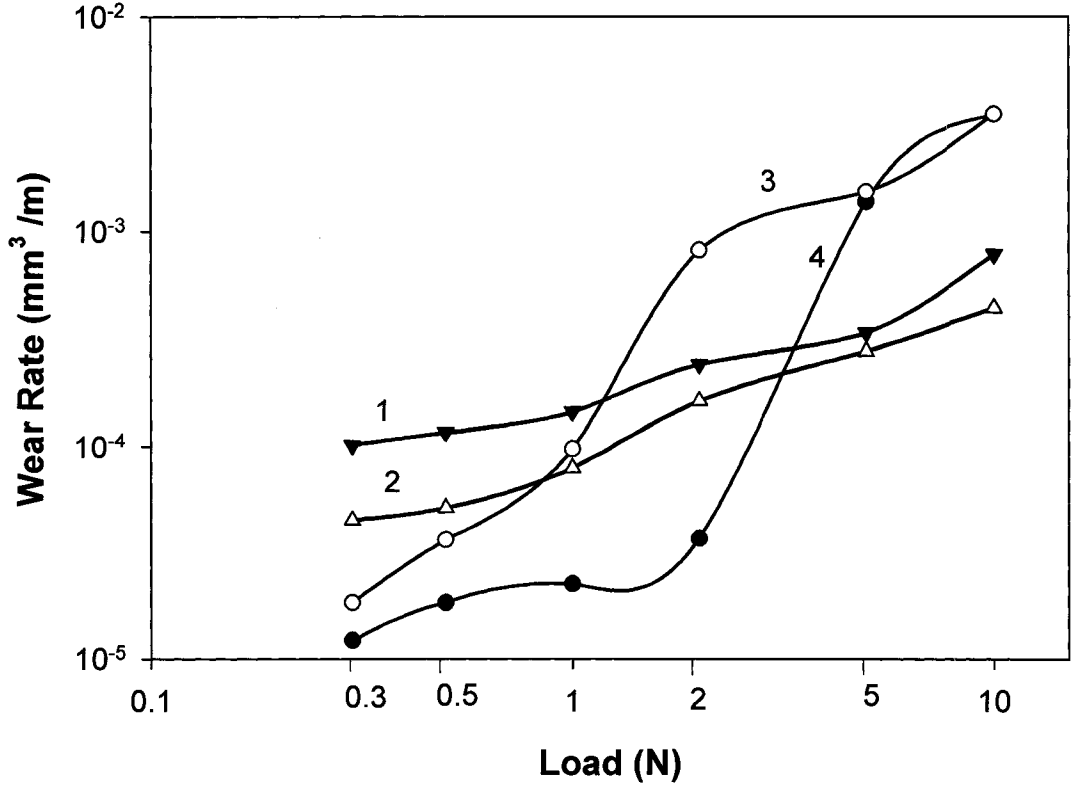
Figure 4.28 Wear rates of A13-C-T6 and A13-S against cast iron rings at 1m/s. (Wear rates against 52100 steel rings at 1m/s were also plotted as a comparison; 1: 52100 steel ring against A13-S sample; 2: 52100 steel ring against Al13-C-T6 sample; 3: cast iron ring against Al13-S sample; 4: cast iron ring against Al13-C-T6 sample)

116
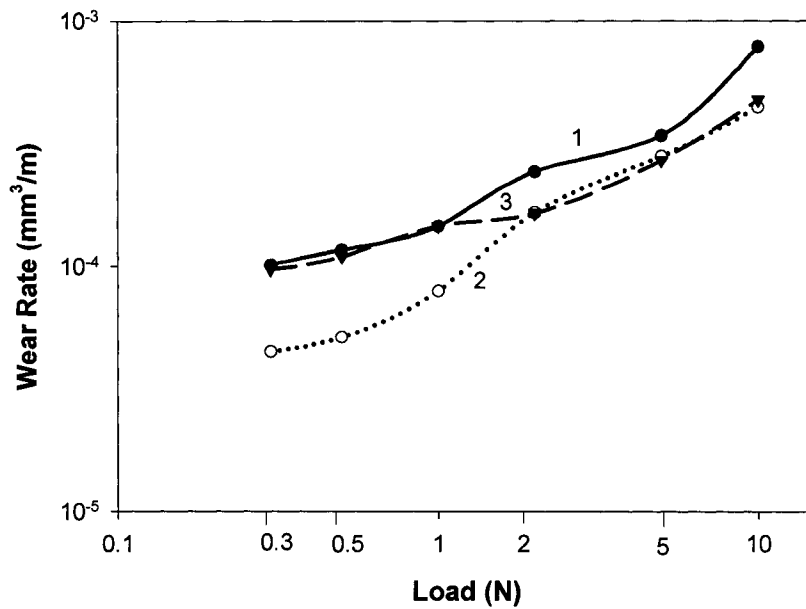
Figure 2.29 (1) Wear rates as a function of load for Al-Si alloys with different matrix hardness (1: A13-S; 2: Al13-C-T6; 3: Al13-C-T6-AN)
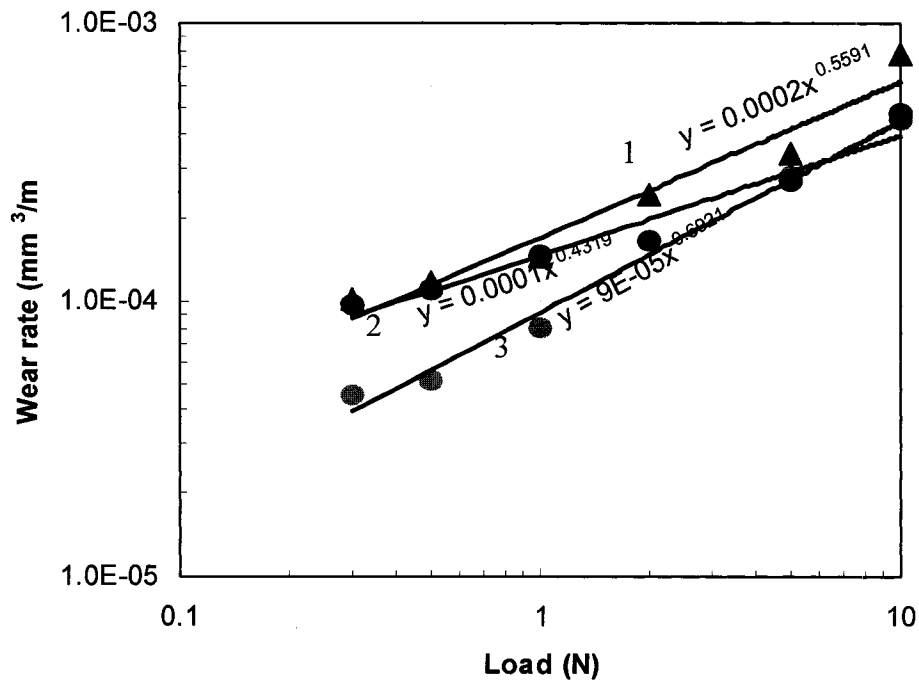
Figure 2.29 (2) Power low of wear rates as a function of load for Al-Si alloys with different matrix hardness (1: A13-S; 2: Al13-C-T6; 3: Al13-C-T6-AN)

117
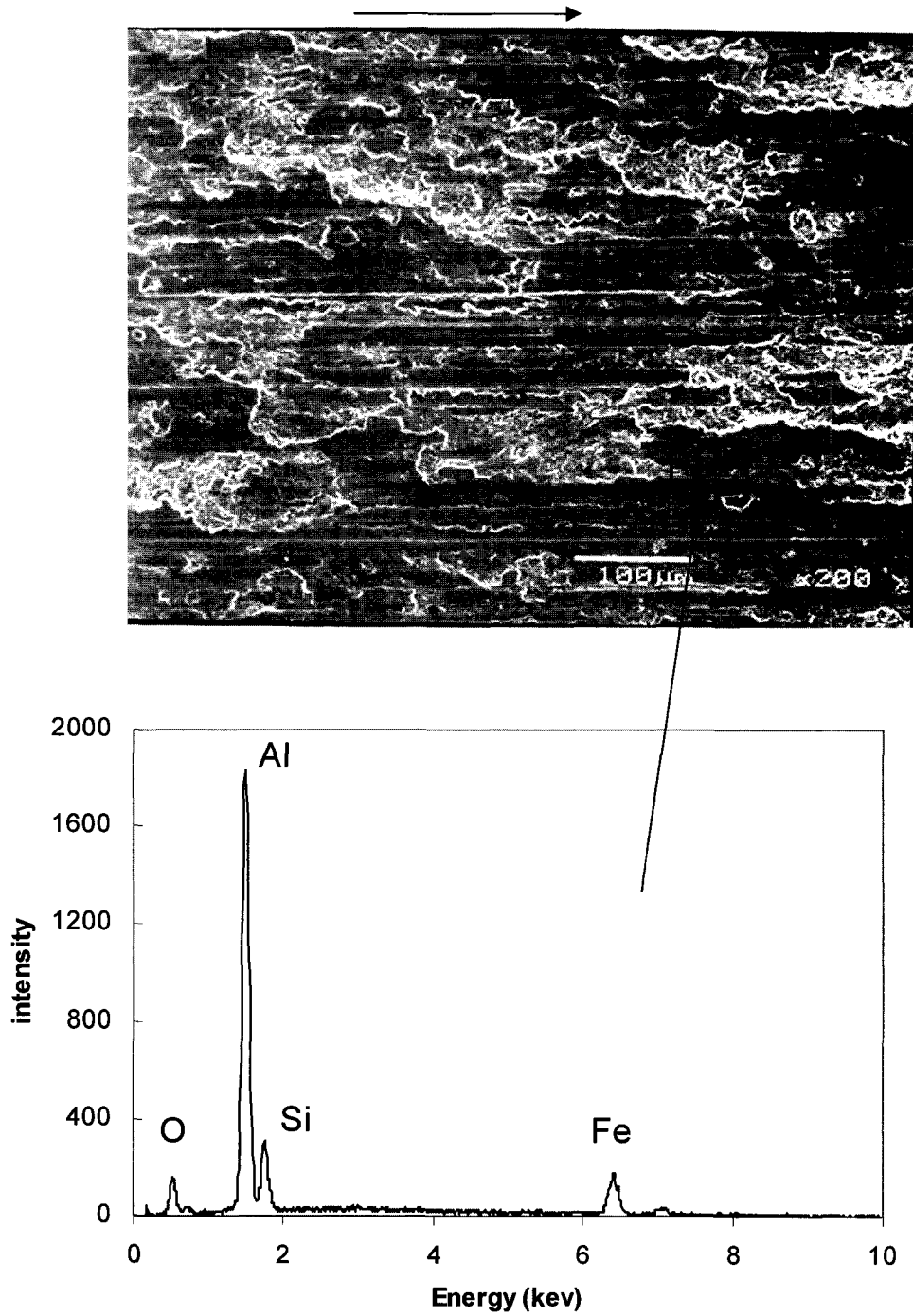
Figure 4.30- a) General SEM worn surface image of A13-C-T6 (5N) at low magnification; b) EDS analysis of the dark grey area on the SEM image is shown in Figure 4.30 (b).

118
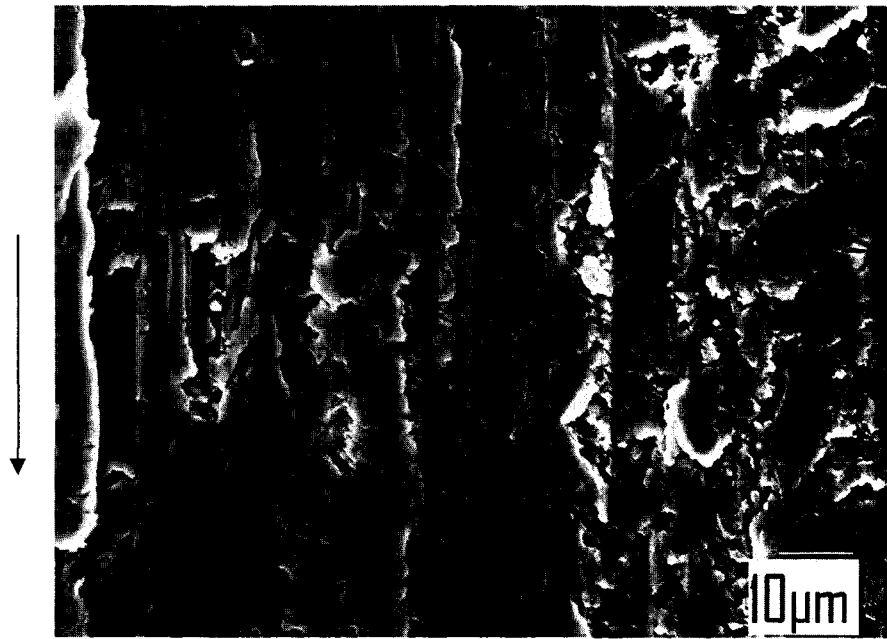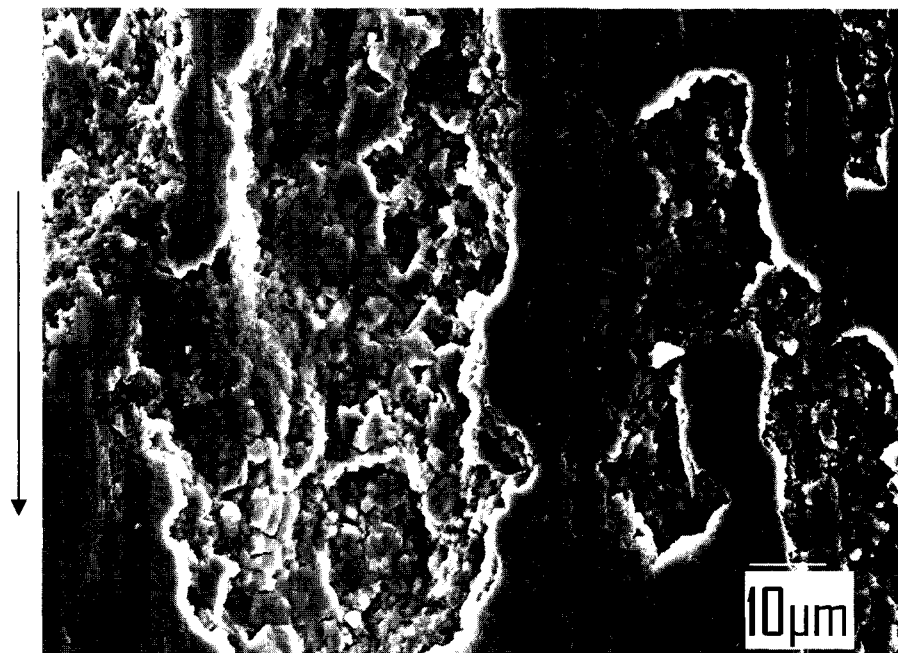
Figure 4.31- a) SEM worn surface micrograph of A13-C-T6 at high magnification; b) SEM worn surface of A13-S at high magnification. (0.3N, counterface AISI 52100 steel ring).

119
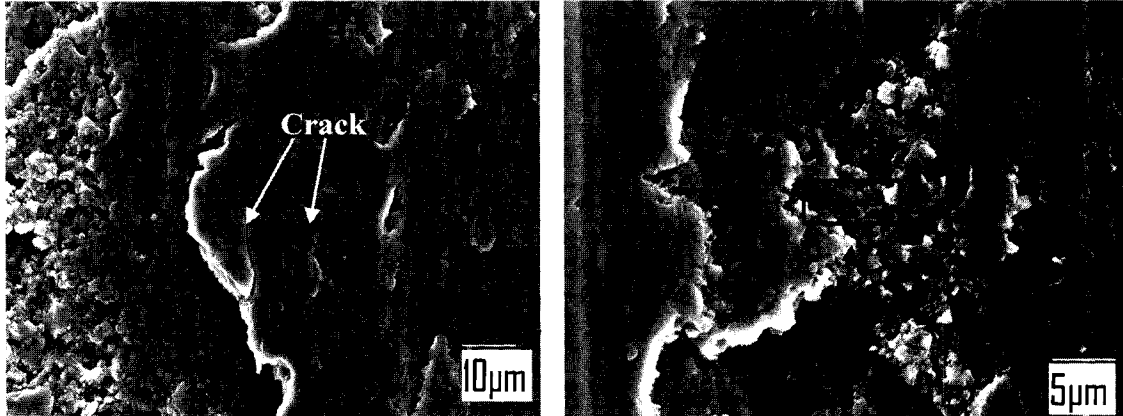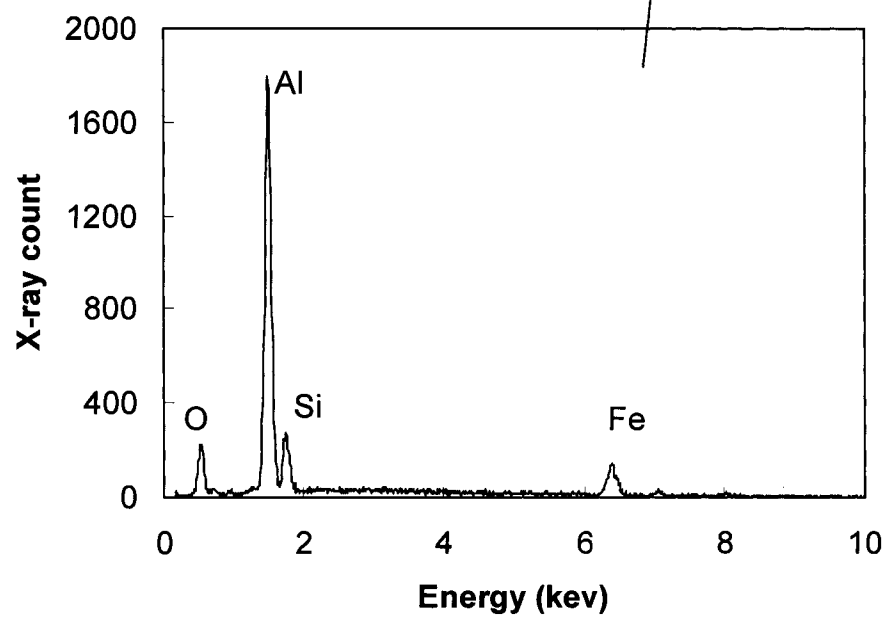
Figure 4.32- a) Arrows on the worn surface at high magnification shows micro-cracks in A13-C-T6 sample (2N); b) Top view of the mechanically mixed layer in a crater (A13-C-T6, 2N); c) EDS spectrum from the area marked by box on the SEM image Figure 4.32 (b) identified large amount of O element.

120

(a)
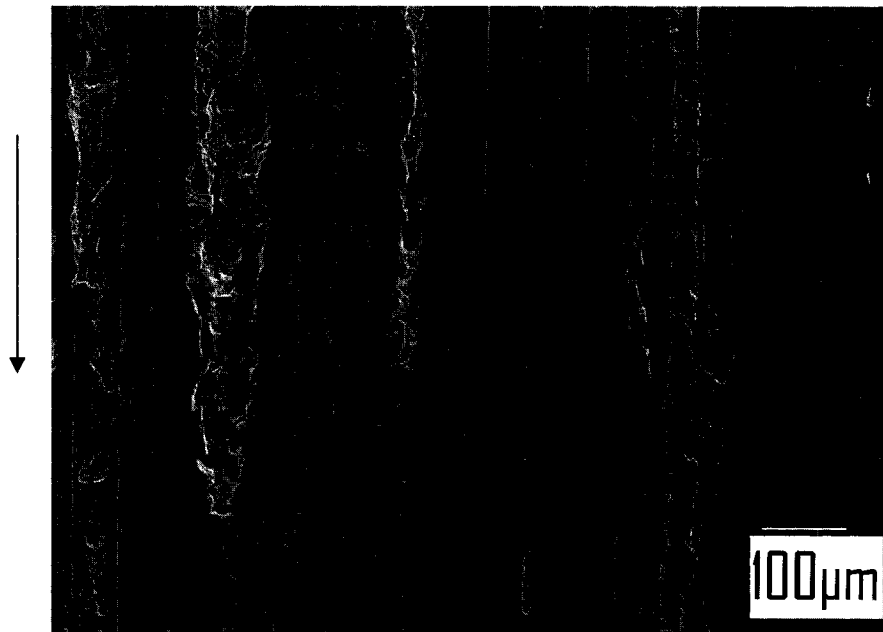
(b)

Figure 4.33- a) Worn surface of A13-C-T6 shows polished appearance (2N, counterface A40 cast iron ring); b) Worn surface of A13-C-T6 shows ploughed topographies (5N, counterface A40 cast iron ring).

121
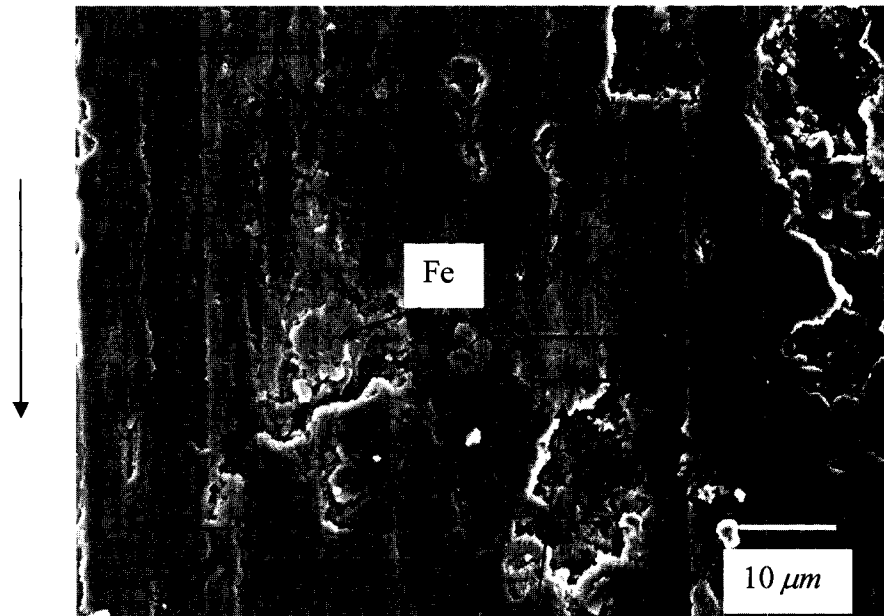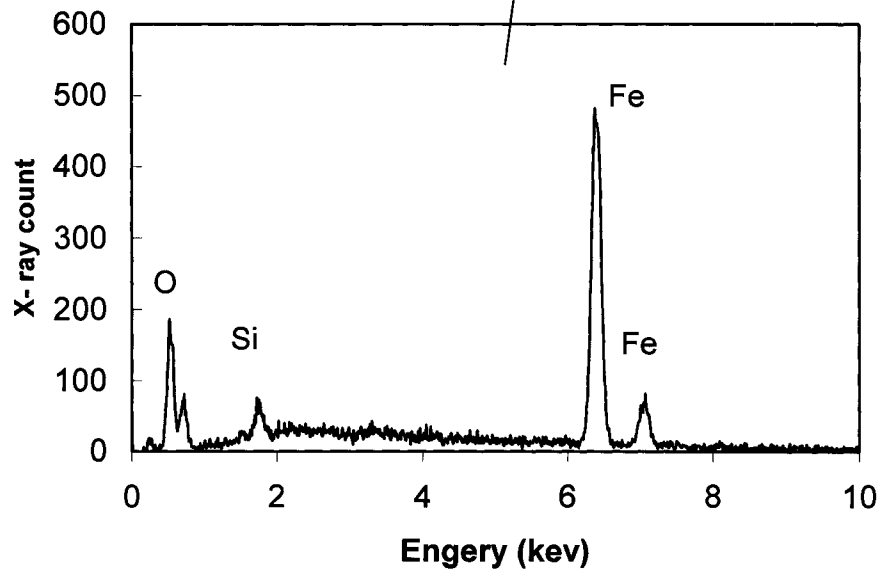
Figure 4.34- (a) Smeared transferred layer on the A13-C-T6 worn surface (5N, 1m/s); b) EDS spectrum identified that this smeared layer in Figure 4.34 (a) was Fe containing large amount of O element.

122
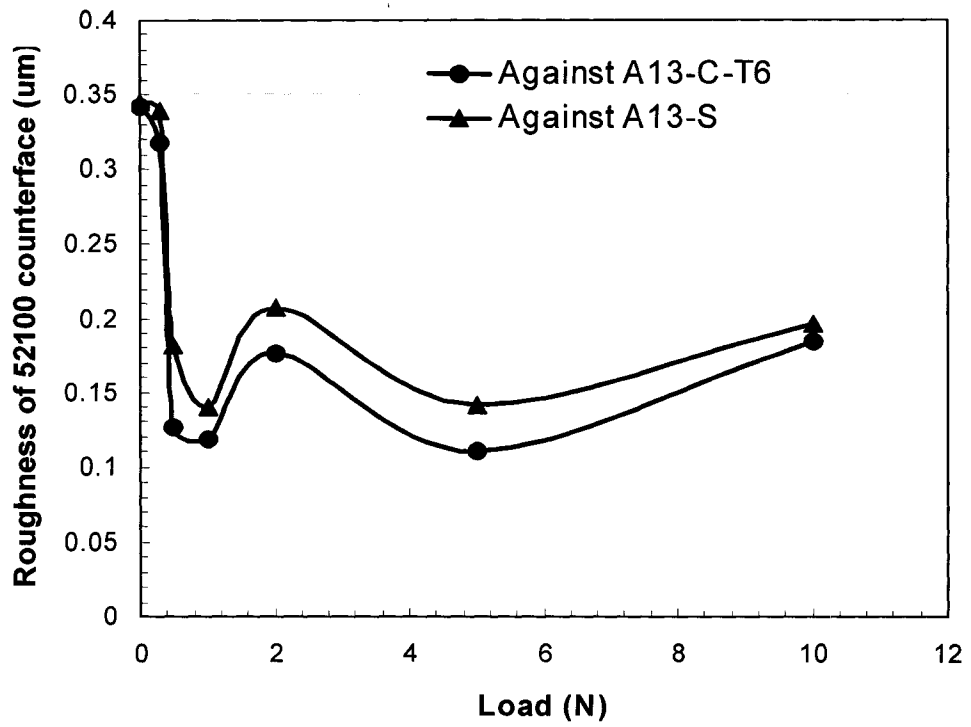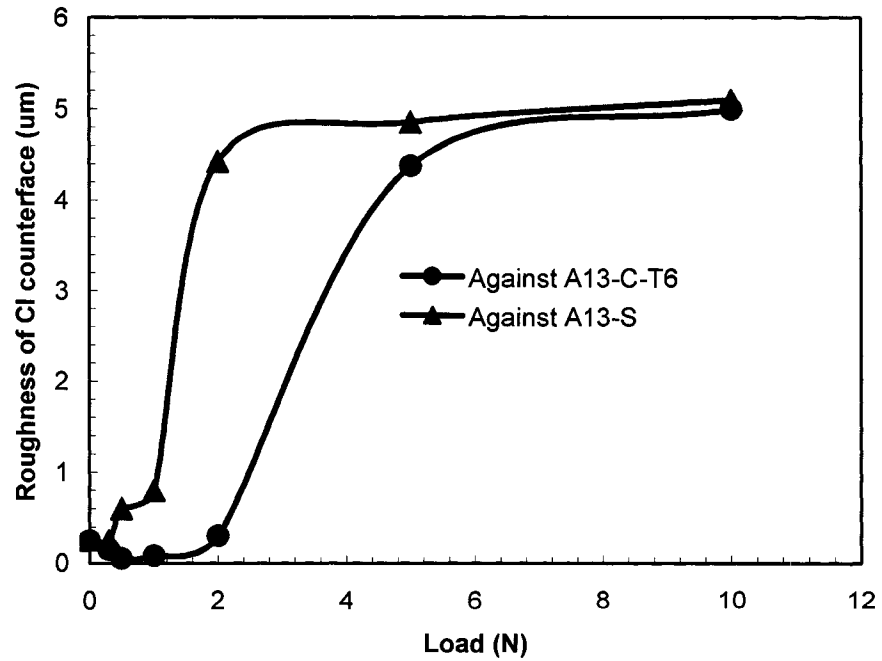
Figure 4.35- a) Surface roughness change of AISI 52100 steel rings against A13-C-T6 and A13-S samples; b) Surface roughness change of A40 cast iron rings against A13-C-T6 and A13-S samples.

123

Unworn   Worn

100µm

(a)

Unworn   Worn

100µm
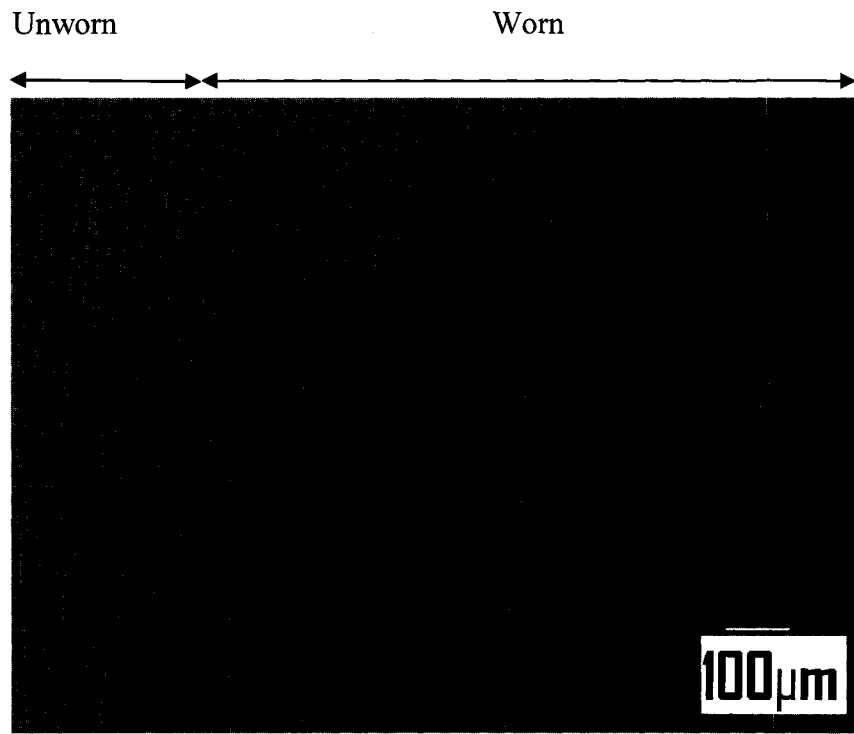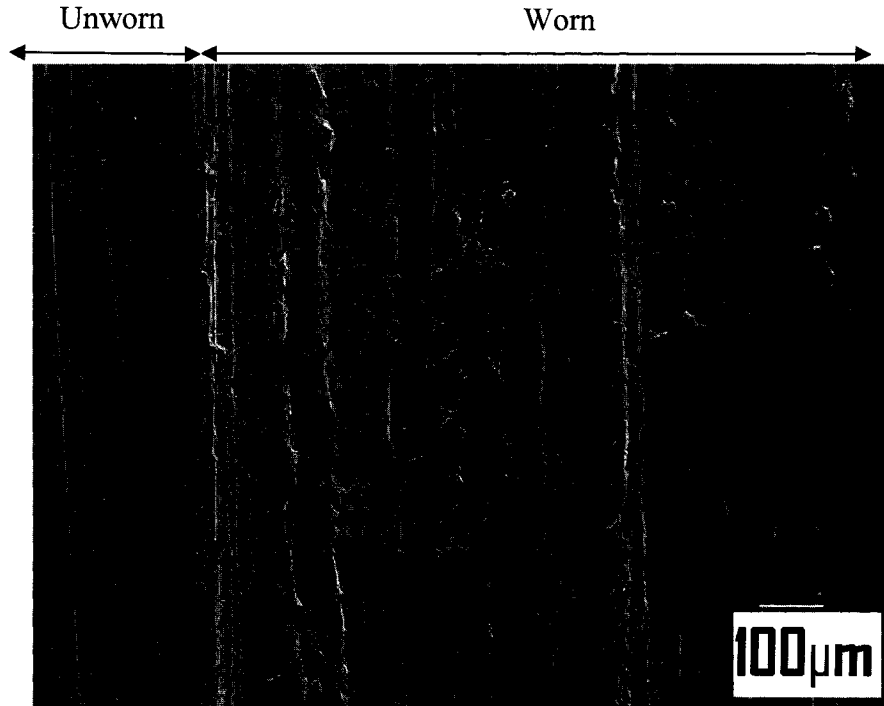
(b)

Figure 4.36 Worn surfaces of cast iron rings against A13-C-T6, (a) 5N, (b) 2N

124
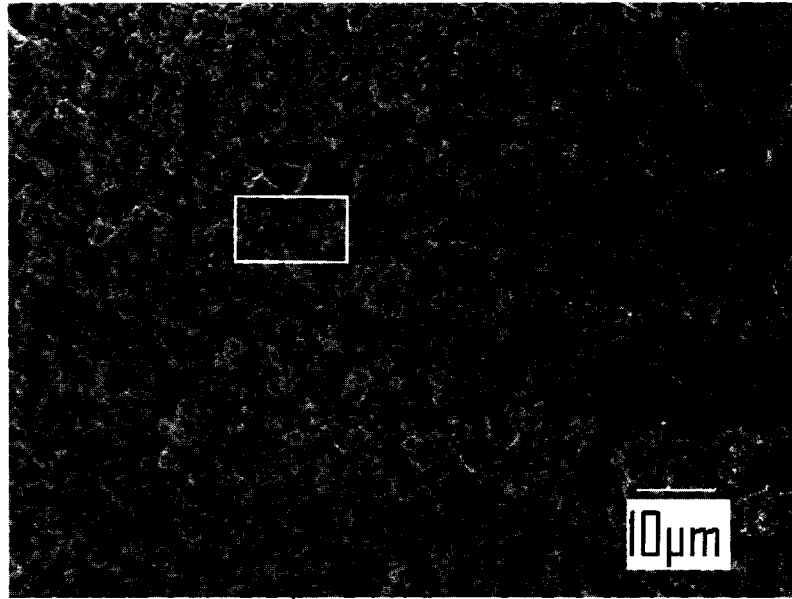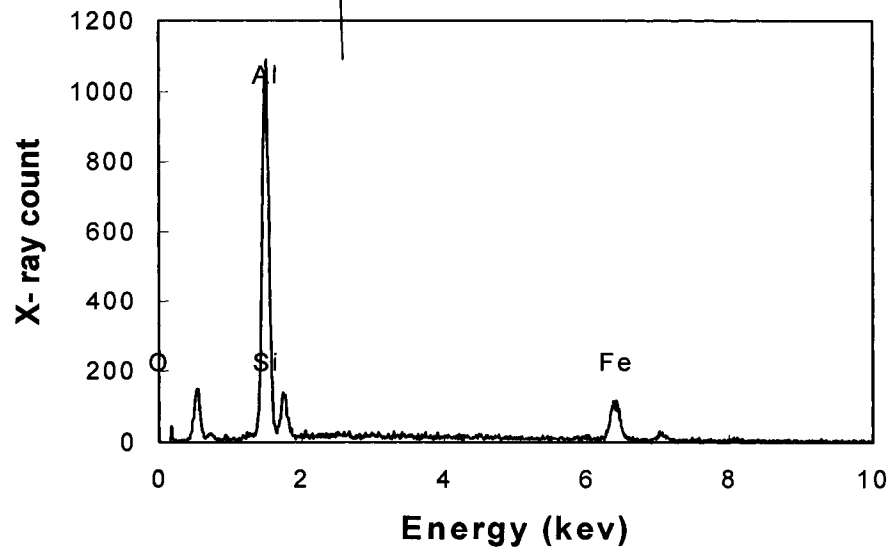
Figure 4.37- a) SEM image of debris of A13-C-T6 (0.3 N, 1m/s, counterface AISI 52100 steel ring); b) EDS spectrum from area marked by box Figure 4.37 (a).

125
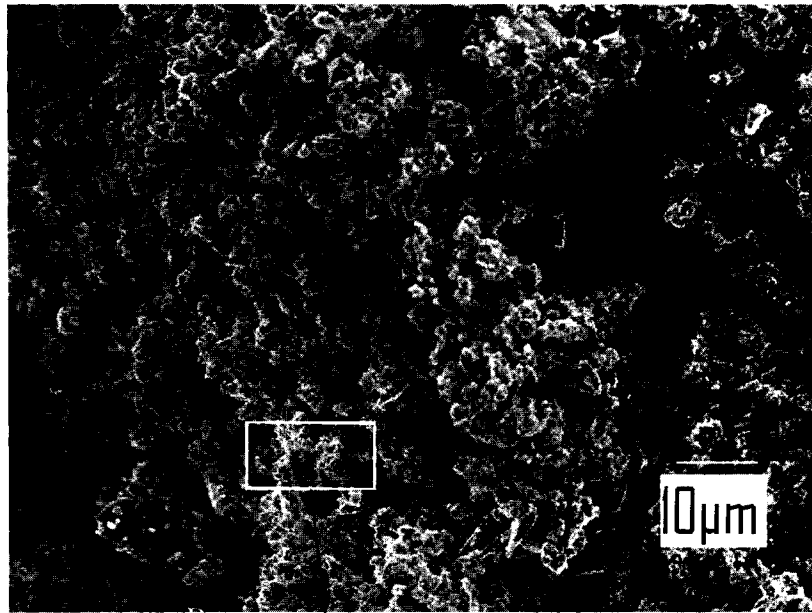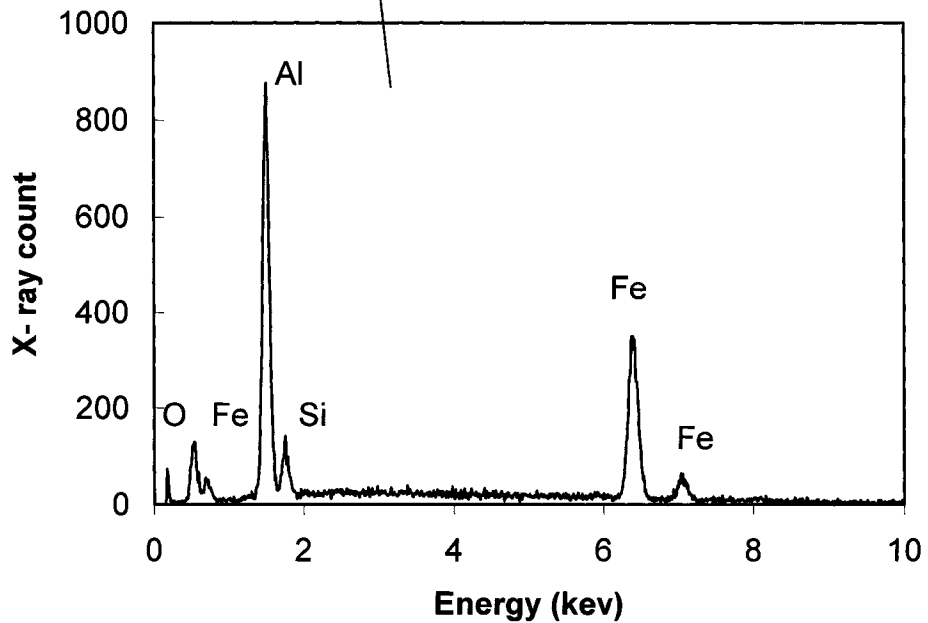
Figure 4.38- a) SEM image of debris of A13-C-T6 (10N, 1m/s, counterface 52100 ring); b) EDS spectrum from area marked by box in Figure 4.38 a.

126
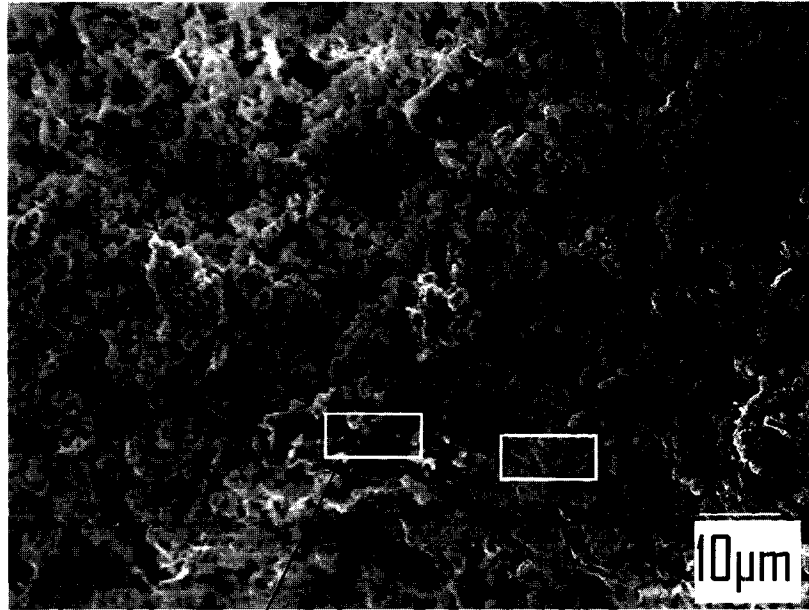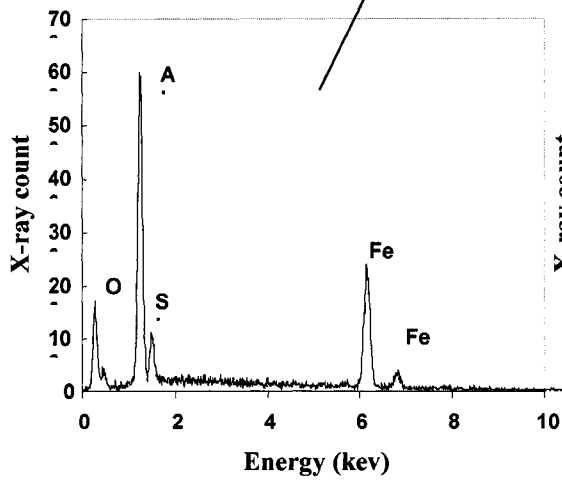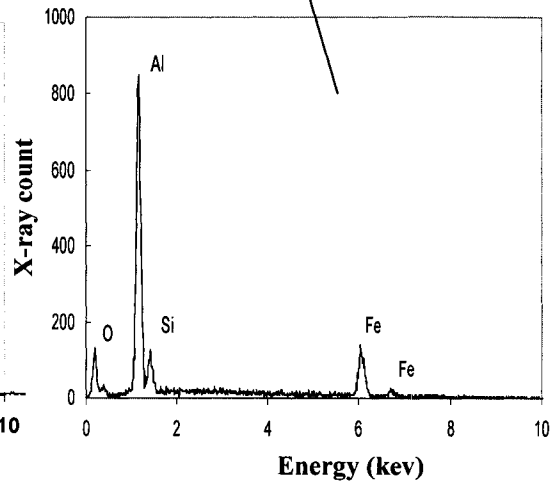
4.39- a) SEM image of debris of A13-S (10N, 1m/s, counterface 52100 steel ring), b) EDS spectrum from the indicated area in Figure 4.39; c) EDS spectrum from the indicated area in Figure 4.39. The similar compositions from areas marked by boxes indicated that the large flake eventually broke up into small powders.

127
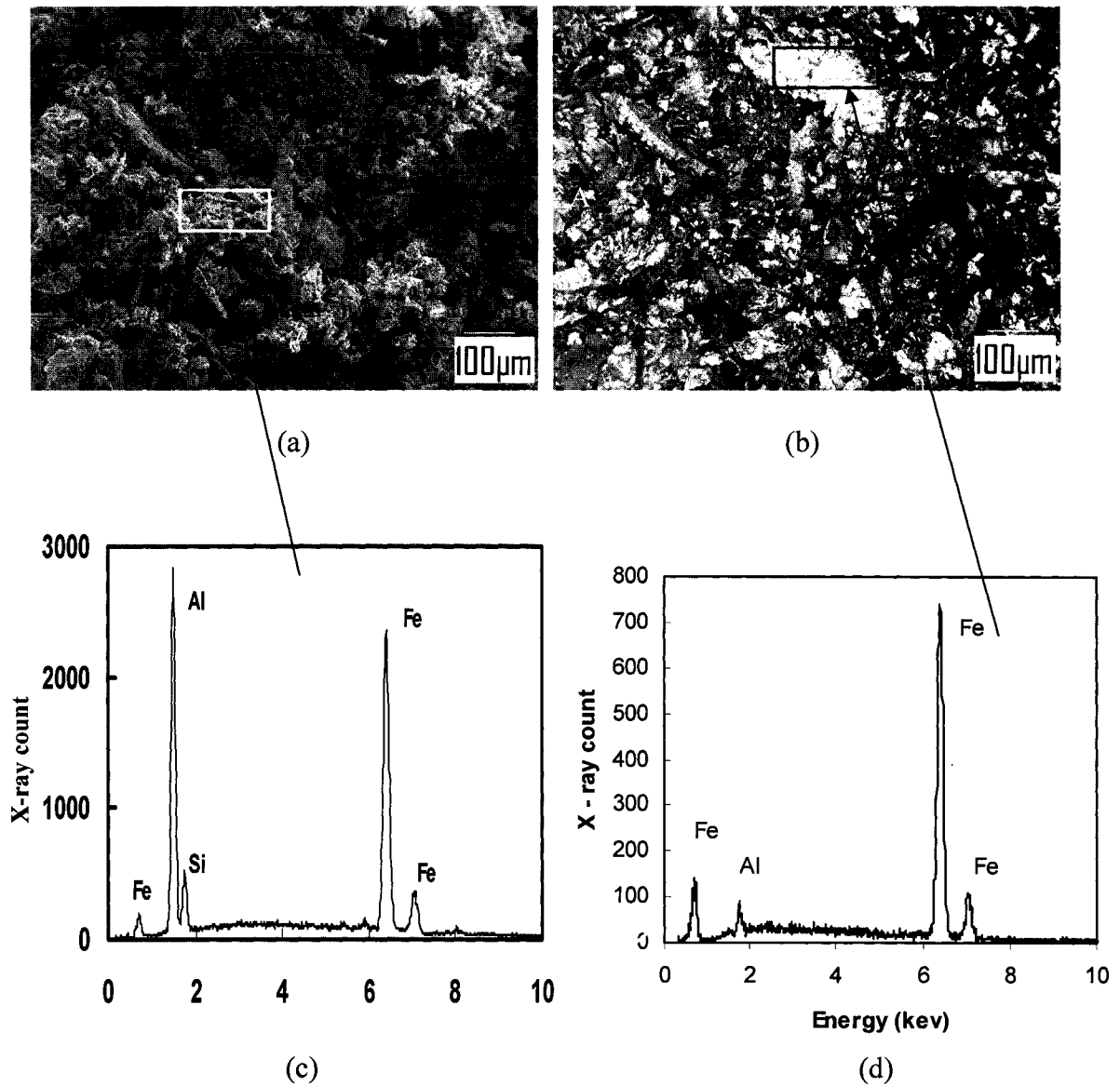
Figure 4.40- a) Secondary SEM image of debris of A13-S (5 N, 1m/s, counterface cast iron ring); -b) Backscattered SEM image Figure 4.40a; c) EDS spectrum from the indicated area in Figure 4.40 (a); EDS spectrum from the indicated area in Figure 4.40 (b).

128

Tribo-layer

(a)

S.D.
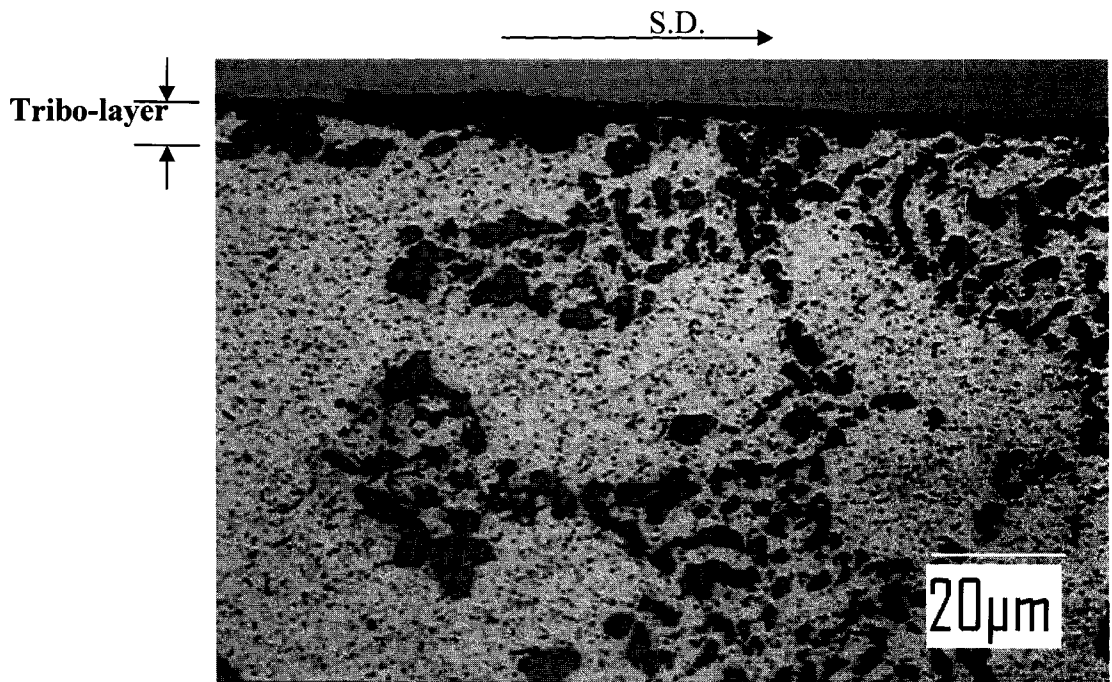
Tribo-layer

(b)

4.41 Cross sectional view of subsurface tested at 1N, 1m/s. a) A13-S, b) A13-C-T6

129
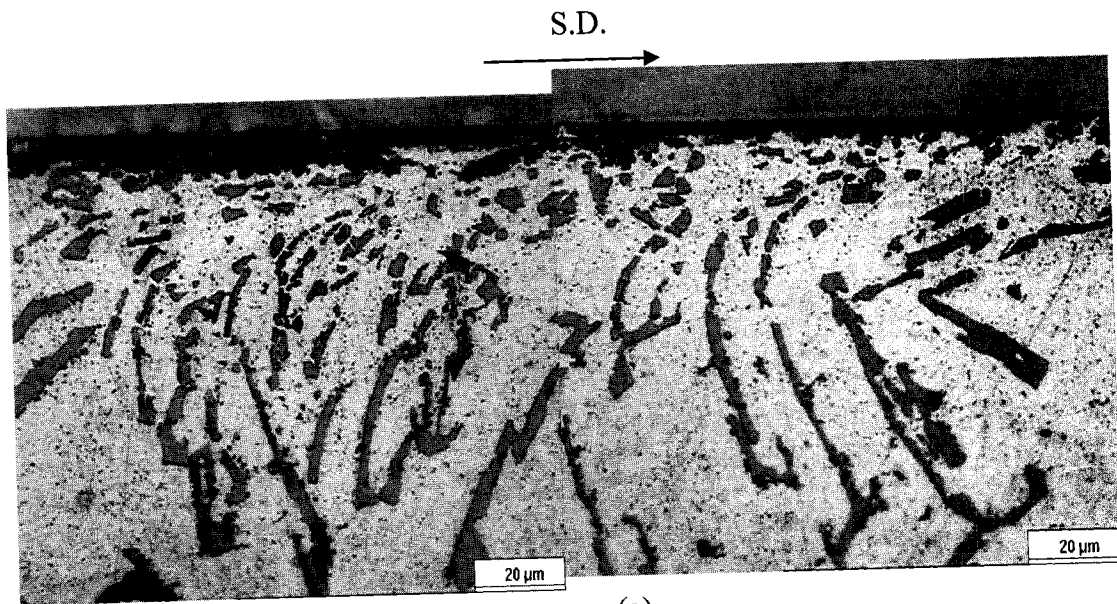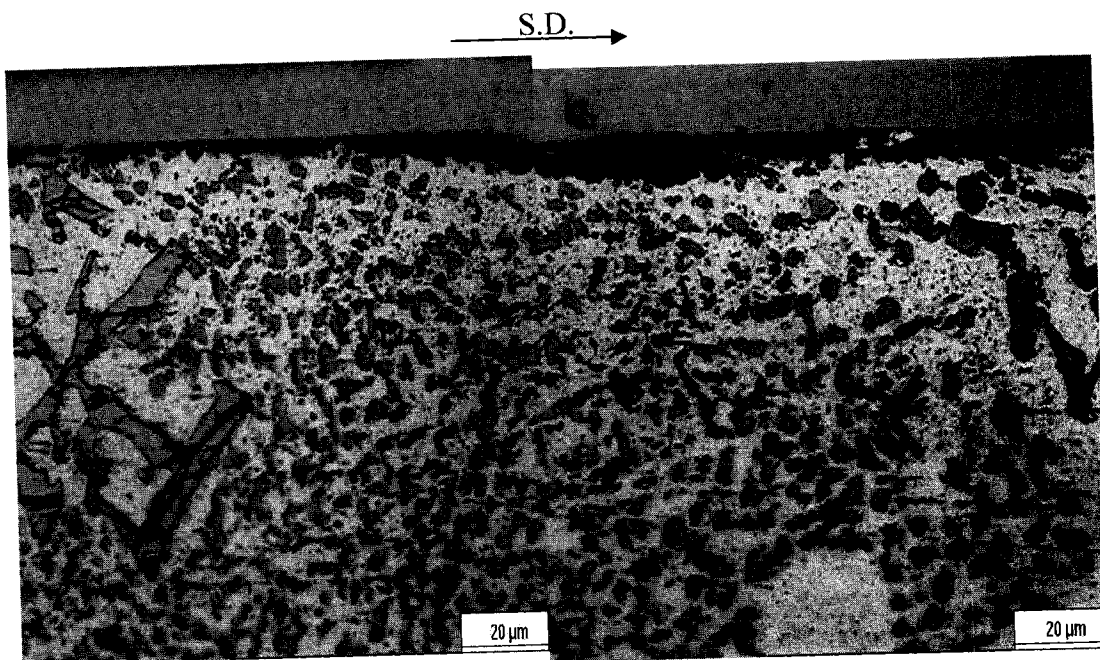
Figure 4.42 Cross sectional view of subsurface tested at 10N, 1m/s. a) A13-S sample; b) A13-C-T6 sample. The dark layers in Figure 4.42 (a) and (b) are tribo-layer zone

130
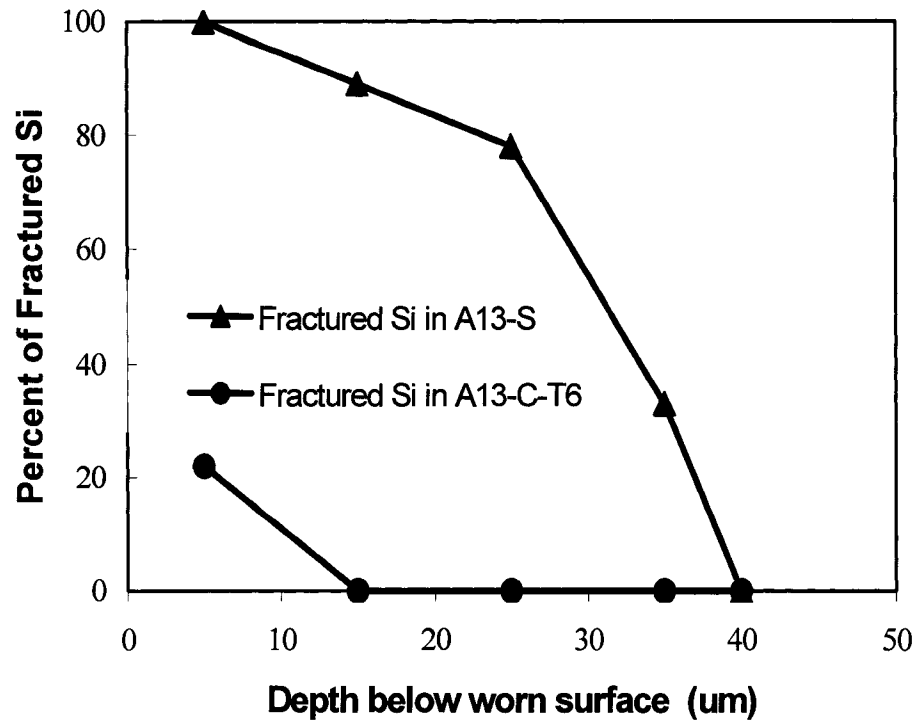
(a)
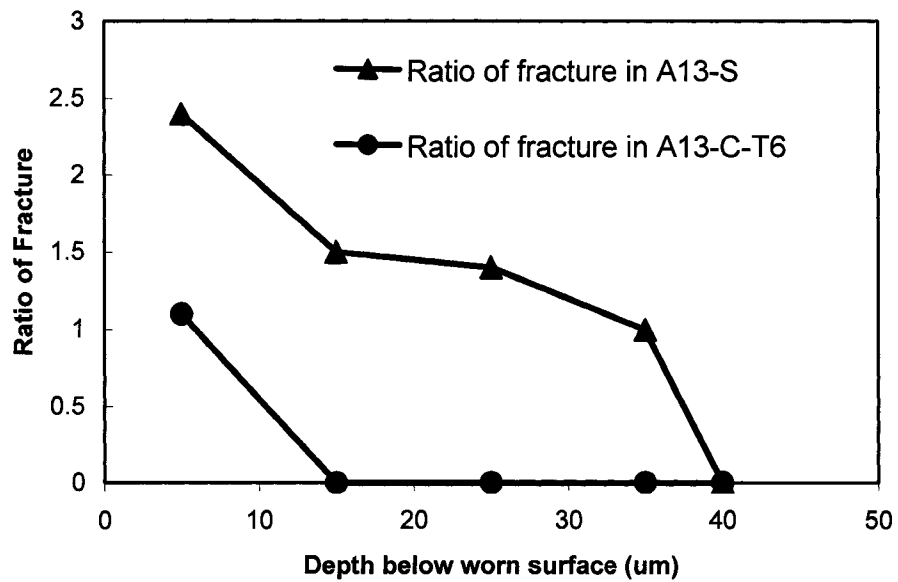
(b)

4.43 a) Silicon particle fracture at different depth (10N, 1m/s); b) ratio of Si particle fracture at different depth.

- Fractured Si=Number of fractured Si particles/overall Si particles within the depth.
- Ratio of fracture = Number of fragments of each Si particle/number of fractured Si particles within the depth.

131

S.D.

(a)

(b)

(c)
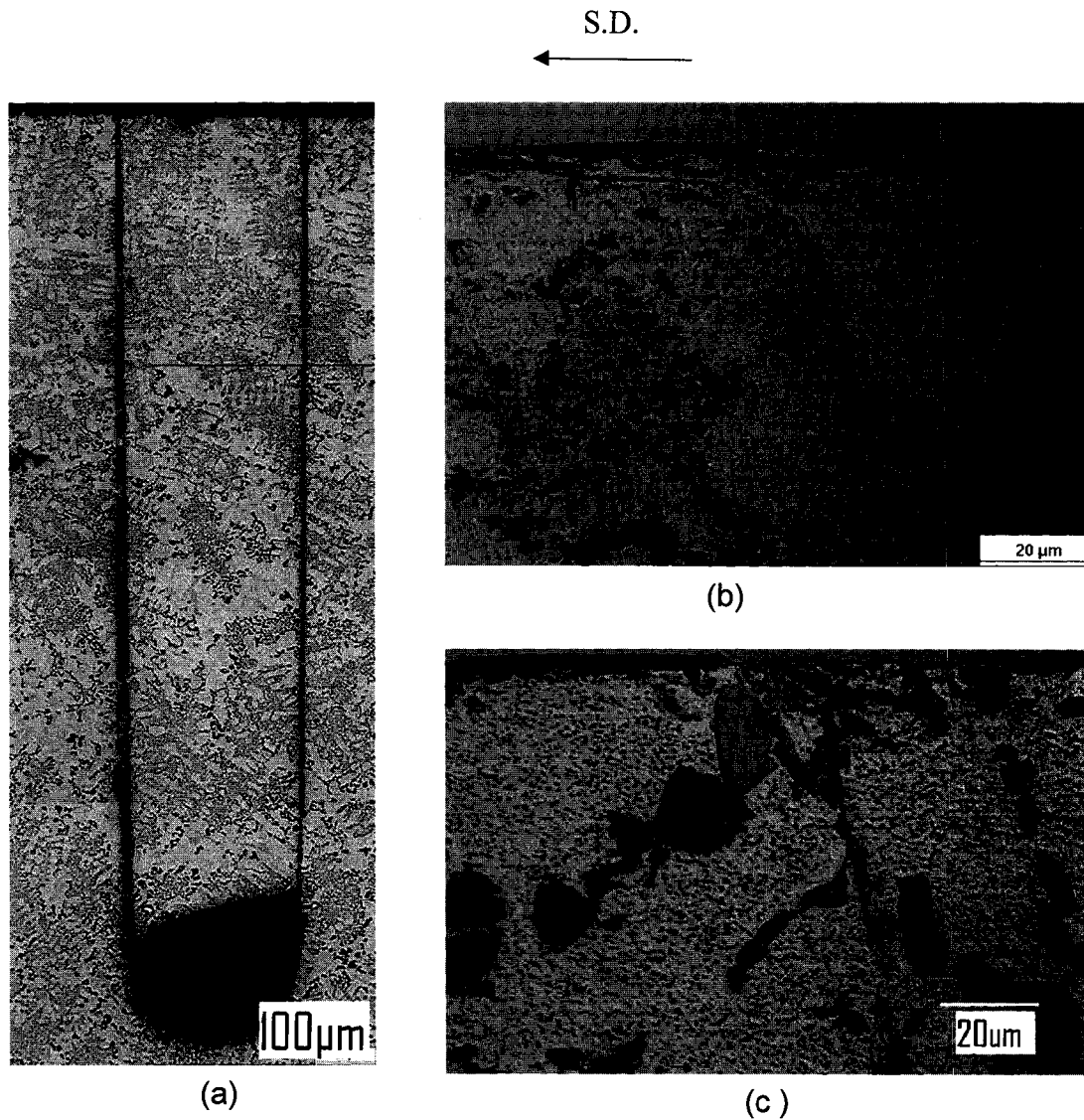
Figure 4.44- a) a reference marker was introduced into slit cut in a A13-C-T6 sample; b) subsurface strain indicated by a marker in the area reinforced with fine round-shaped Si particles after test; c) subsurface strain indicated by a marker in the area reinforced with medium size particles after test. Tests were at 1N, 1m/s with counterface of AISI 52100 steel rings.

132
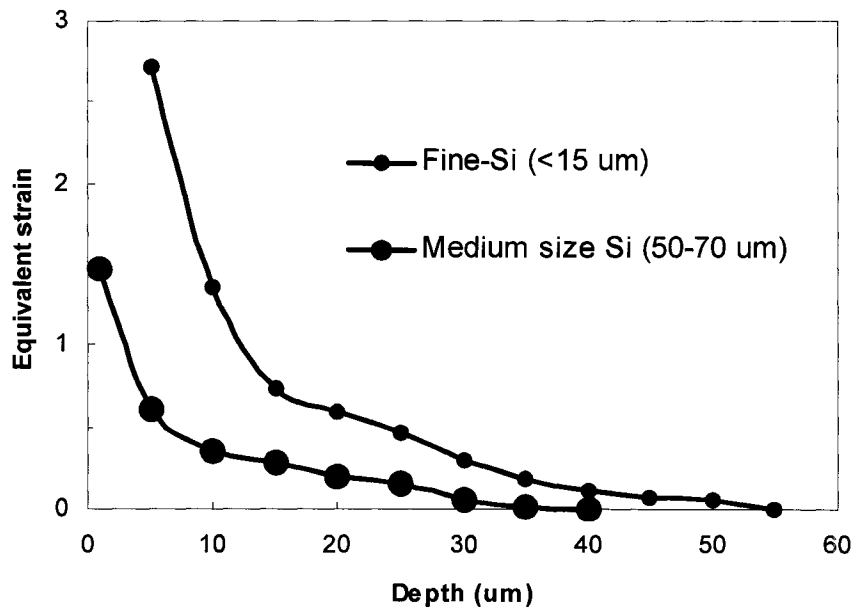
Figure 4.45 Equivalent plastic strain gradients in A13-C-T6 subsurface areas with different particle size (1N, 1m/s).

133
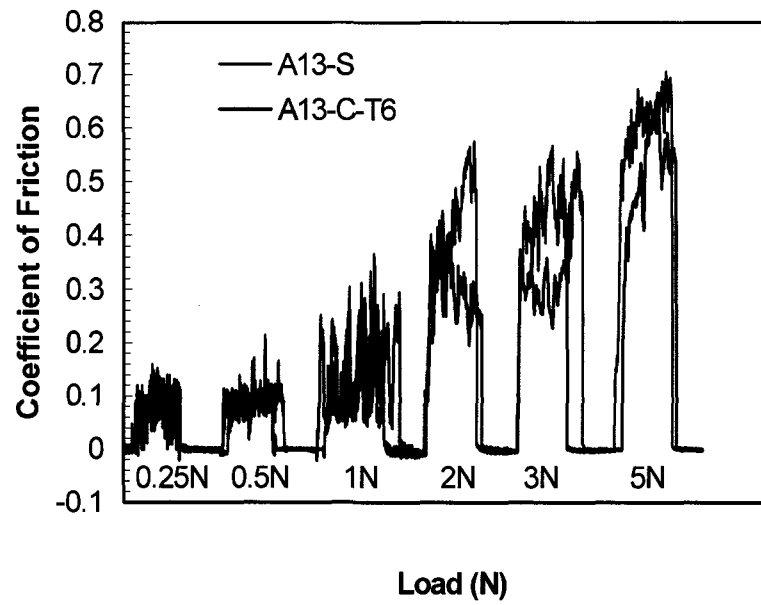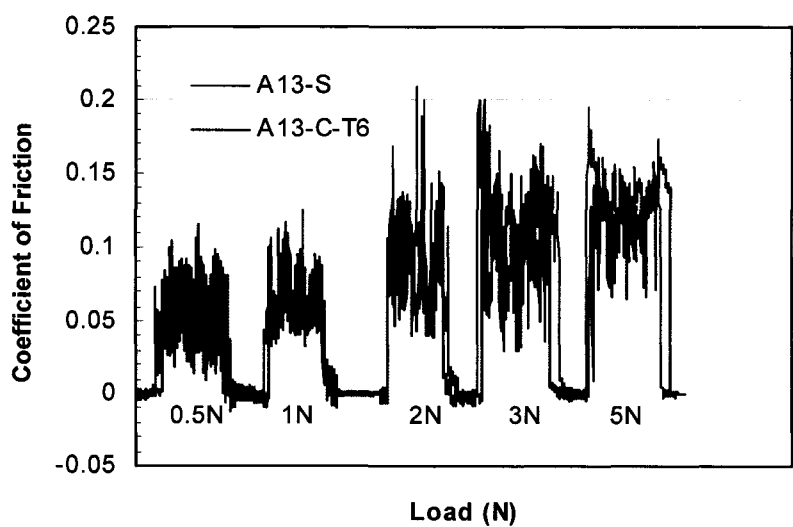
Figure 4.46 COF measured from the scratch tests with the step distance of 20 mm, (a) dry scratch; (b) lubricated scratch.

134
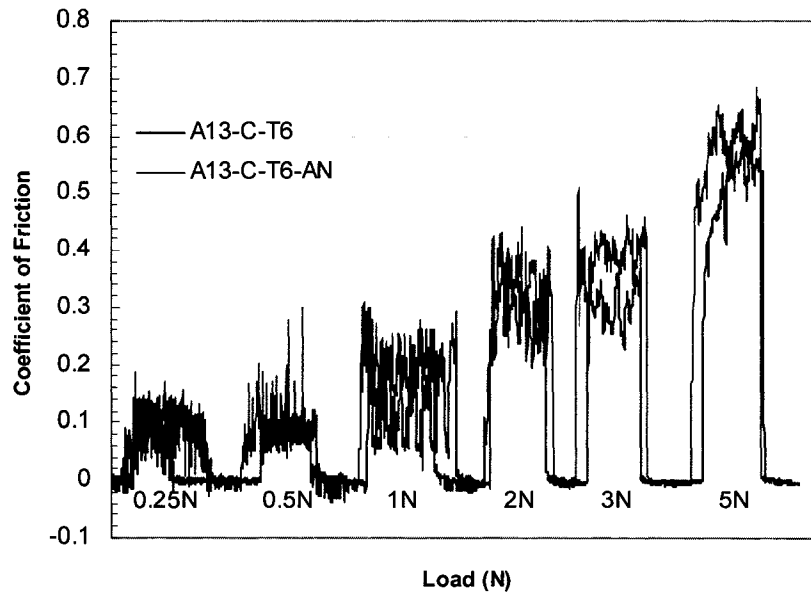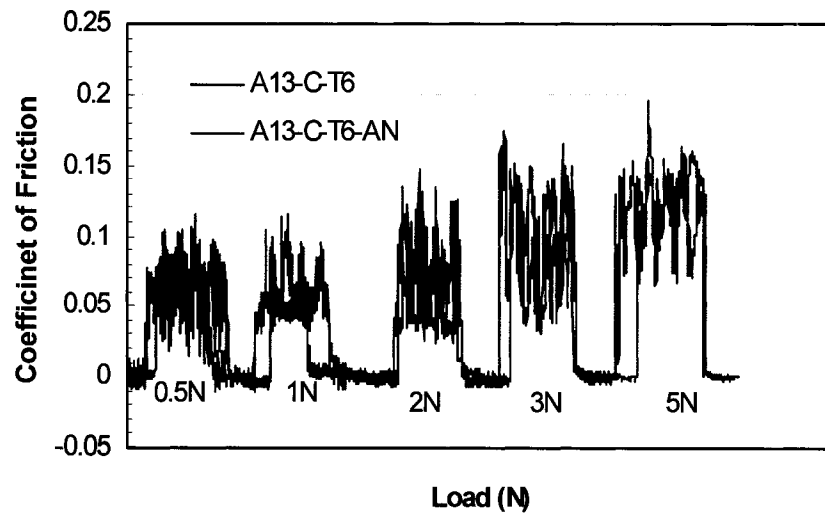
Figure 4.47 COF measured from scratch tests with the step distance of 20 mm. (a) dry scratch; (b) lubricated scratch.

135
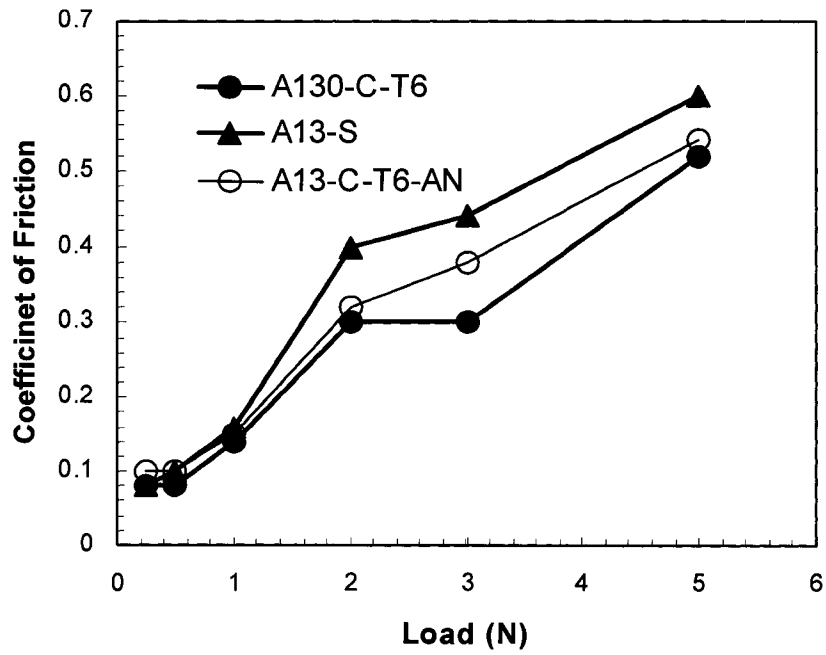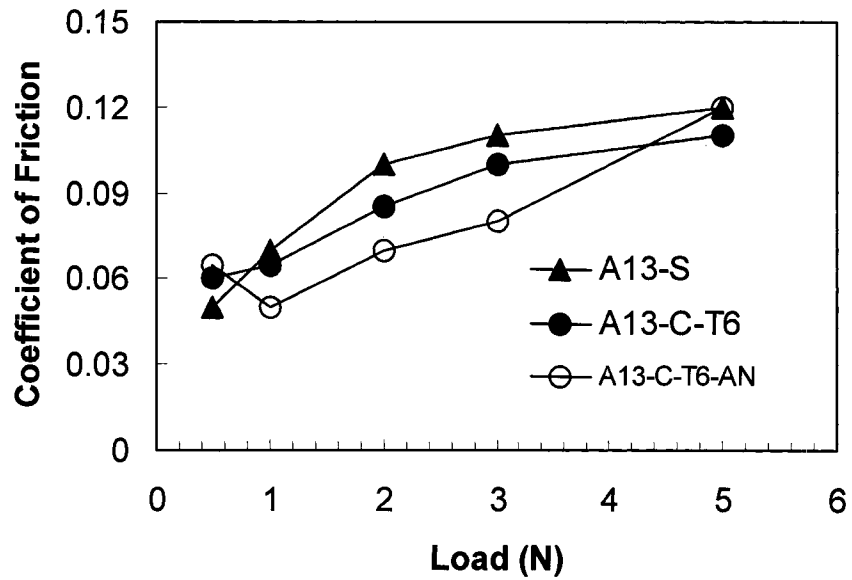
Figure 4.48 COF of the alloys measured from single-pass scratch tests. a) Dry tests; b) lubricated tests.

136

(a)

137
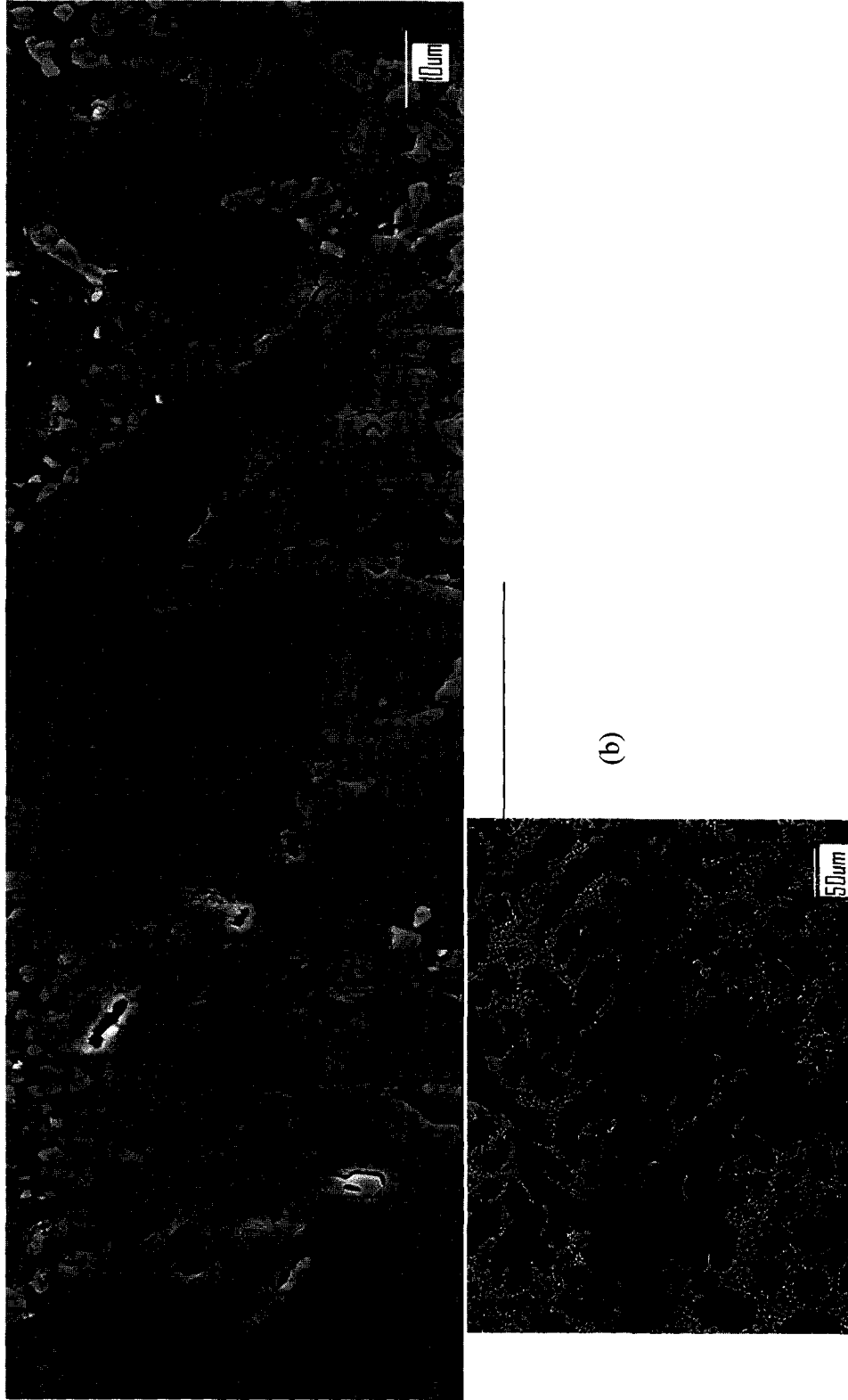
Figure 4.49 Morphologies of scratched surfaces at 0.5 N, dry test (a) A13-S, (b) A13-C-T6

138

(a)

139
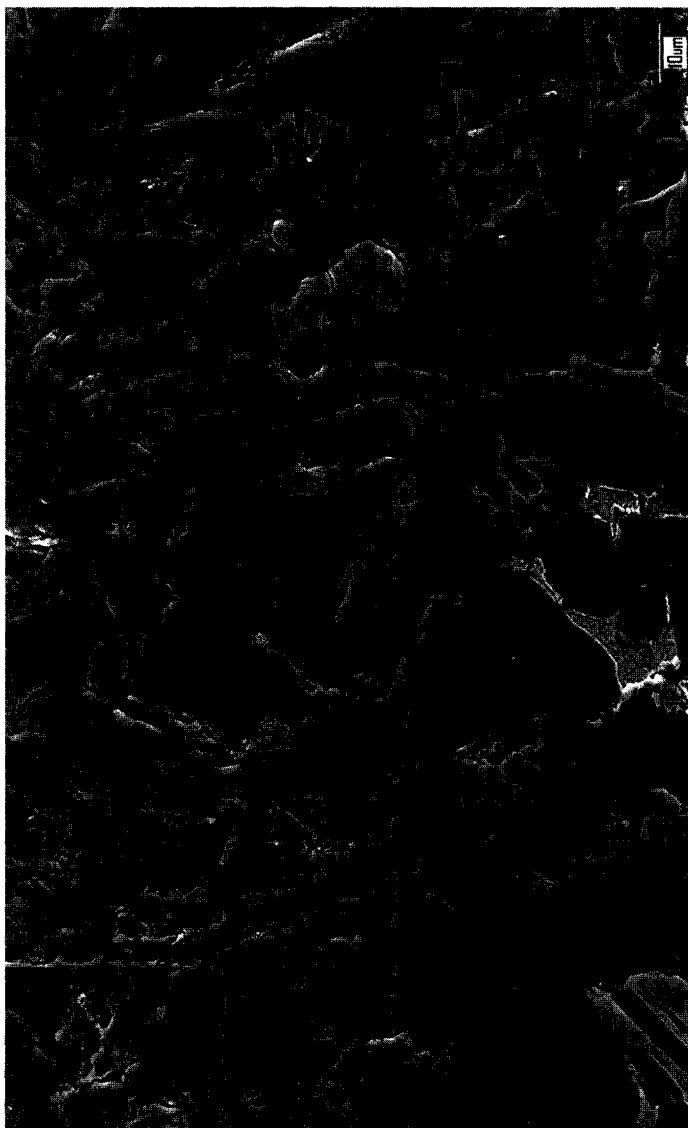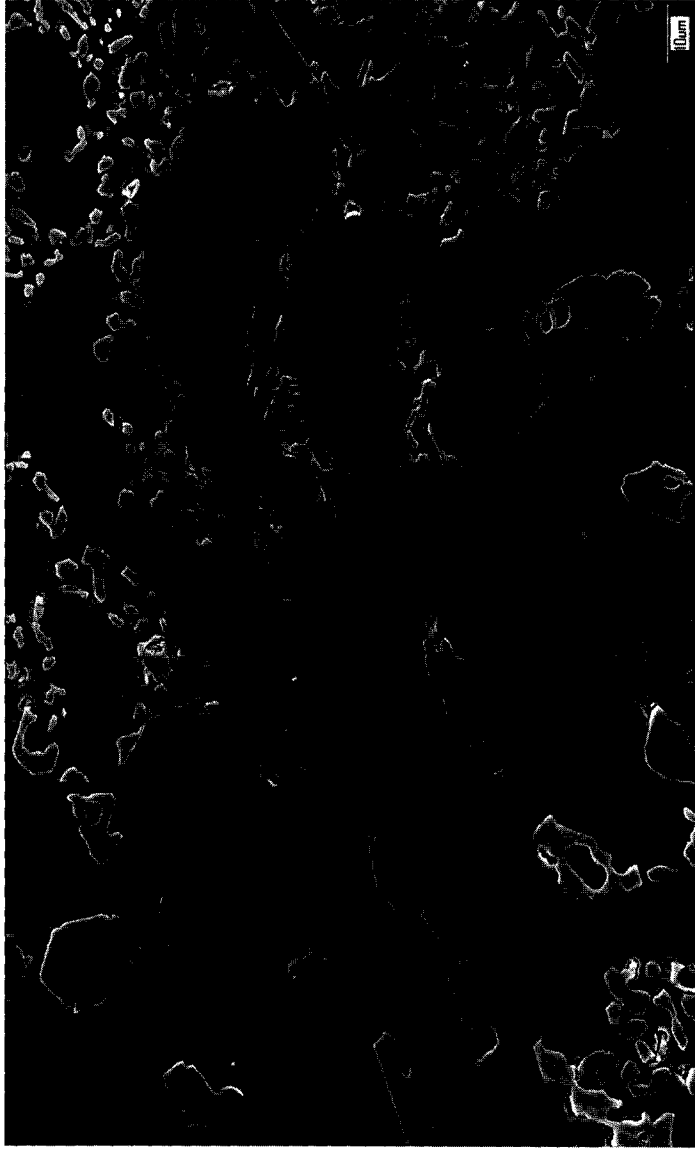
Figure 4.50 Topography of scratched surfaces at 5N, lubricated test. (a) A13-S, (b) A13-C-T6

(b)

140

(a)

141
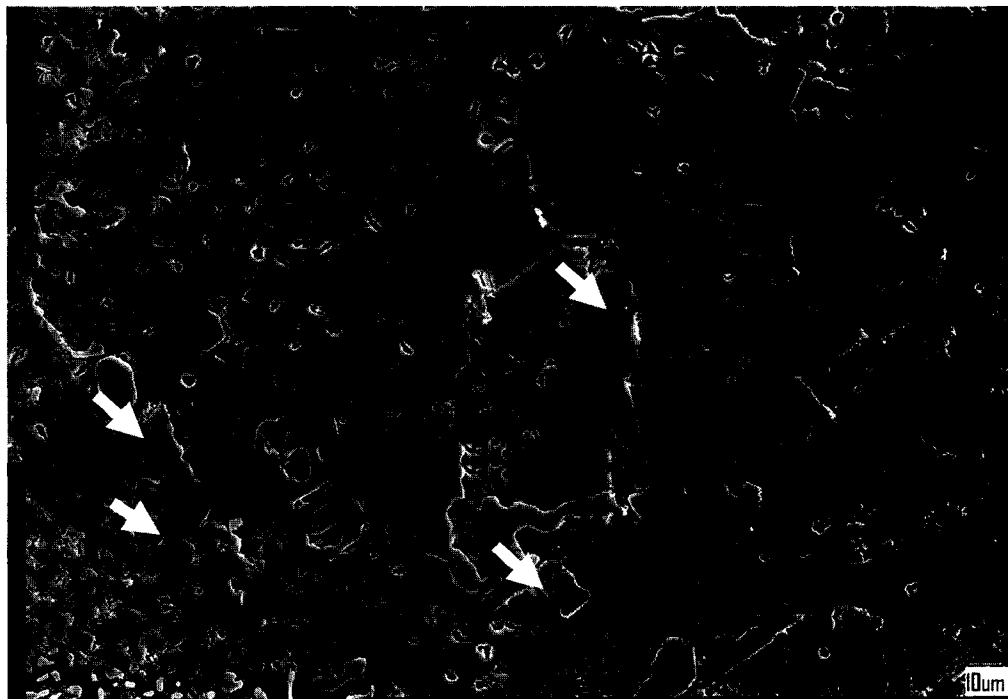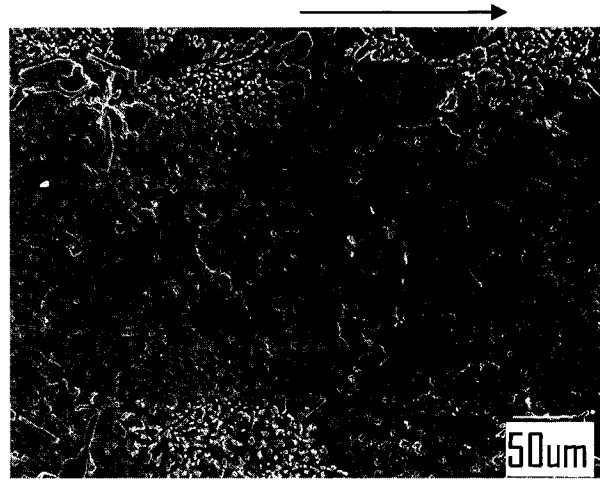
(b)

Figure 4.51 Scratch topographies of A13-C-T6-AN (a) dry scratch, (b) lubricated scratch. Arrows in (b) indicated the particle fracture.
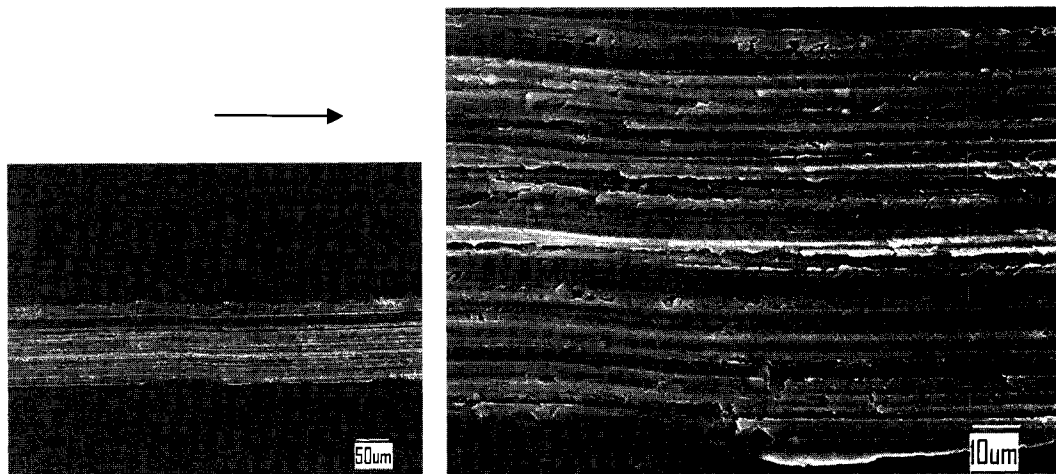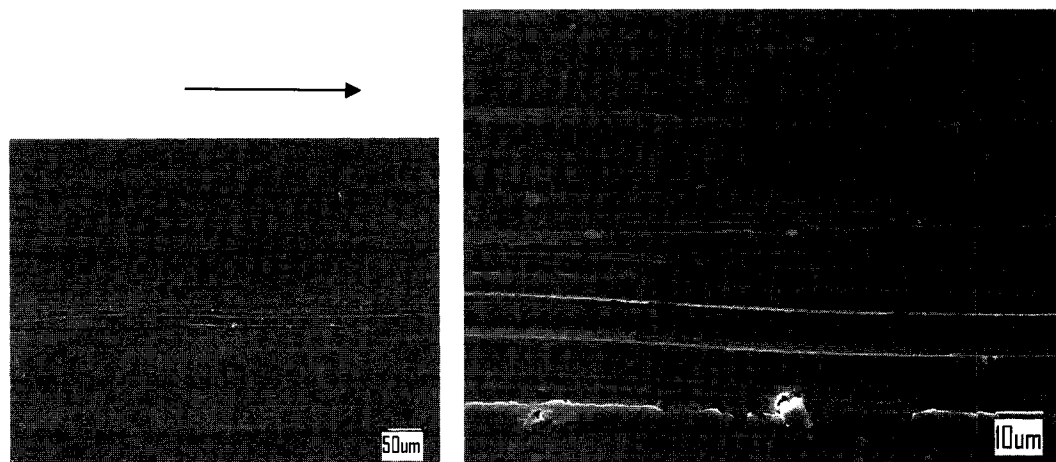
Figure 4.52 Topography of A6061 Al scratch surface. (a) dry scratch at 0.5N, (b) lubricated scratch at 5N.

143
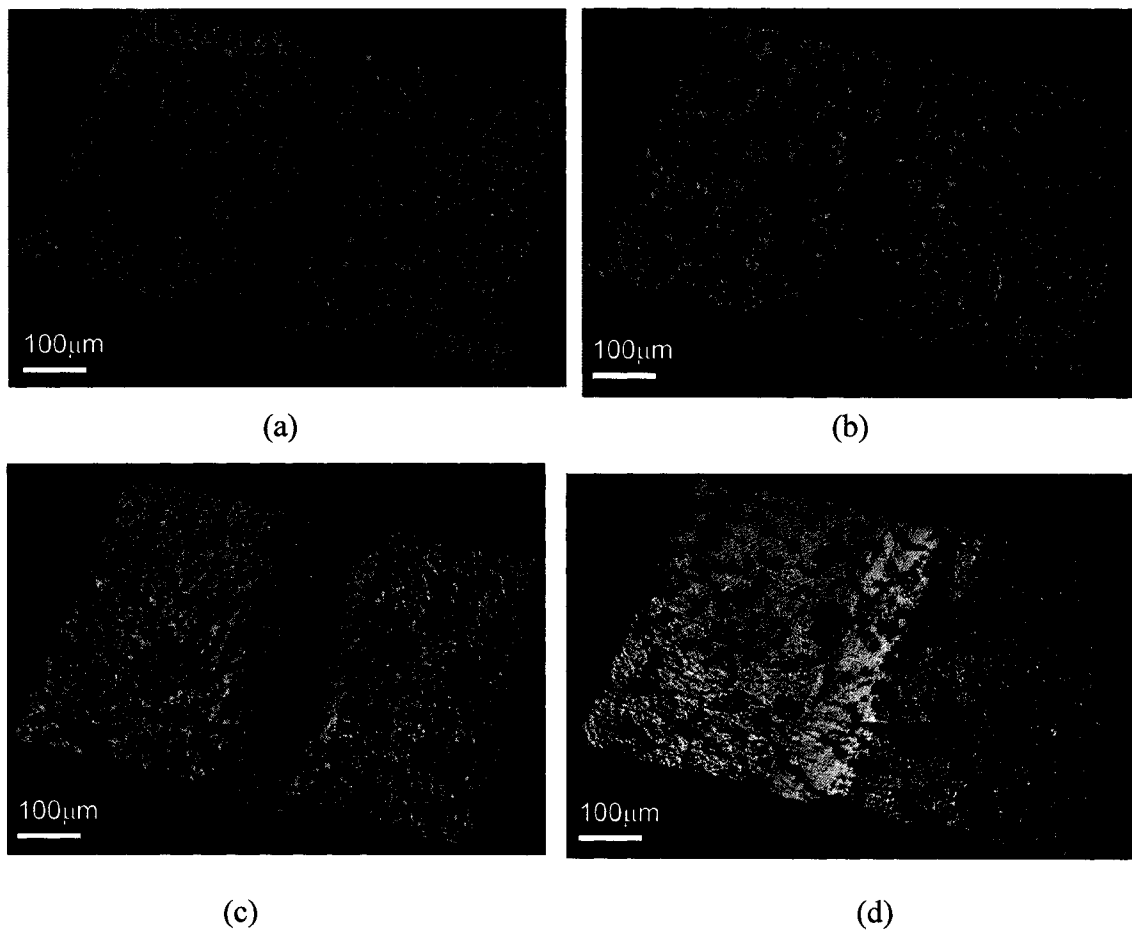
Figure 4.53 Single-pass worn tracks of WYKO 3D images. (a) A13-S (0.5N, dry); (b) A13-C-T6 (0.5N, dry); (c) A13-S (5N, lubricated); (d) A13-C-T6 (5N, lubricated).

144

S.D.

Outside the wear track
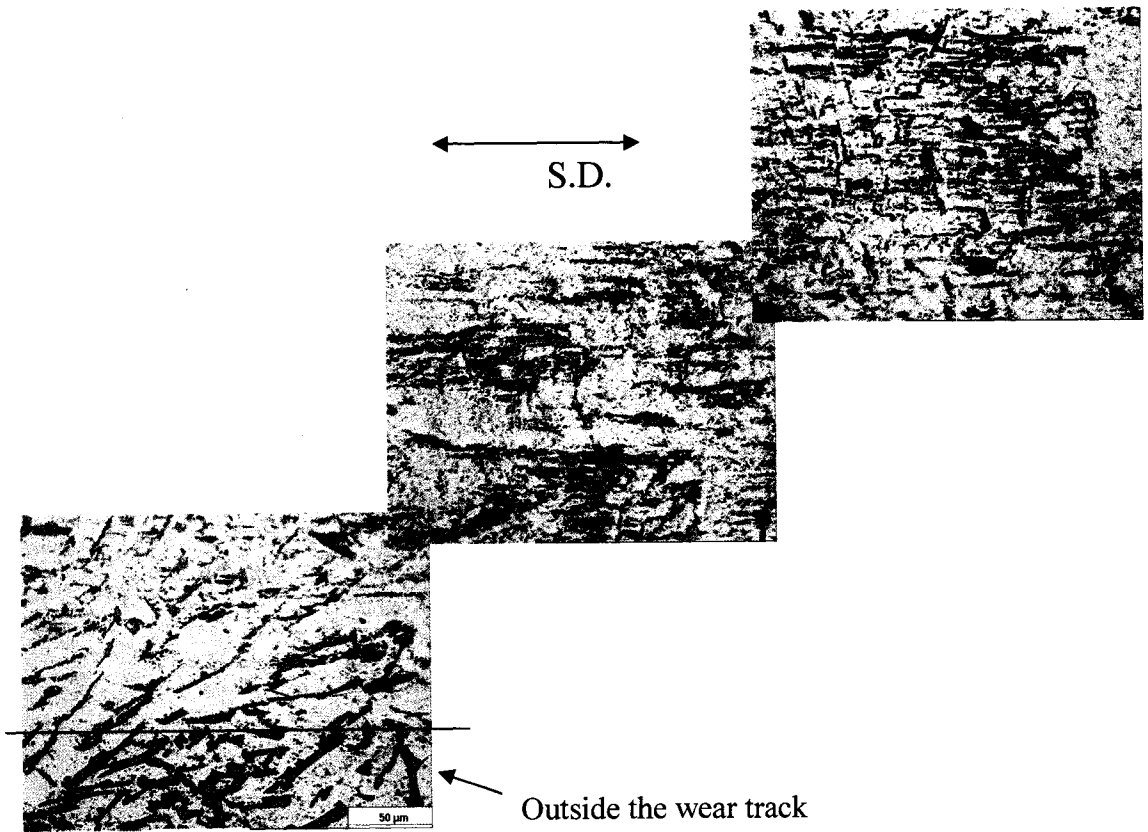
(a)
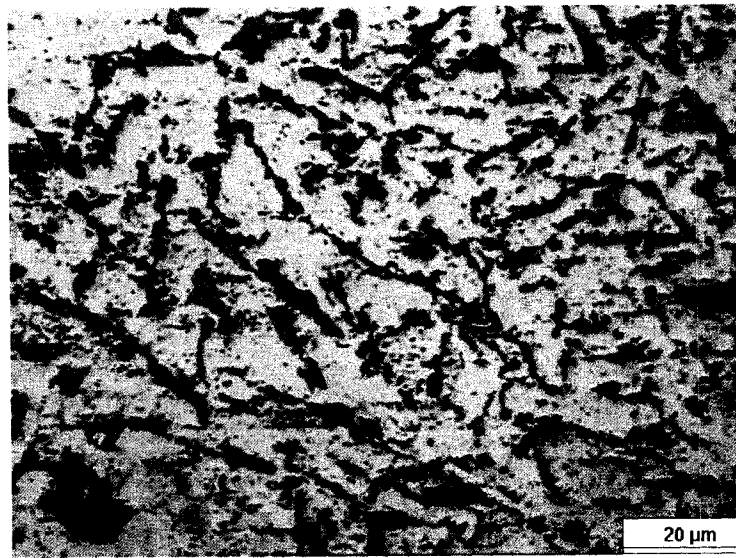
(b)

Figure 4.54 Topographies of worn surface of A13-S after 2.16Km reciprocating wear at 0.72m/s velocity, 150 °C. (a) x500, (b) x1000.

145

S.D

Outside the wear track
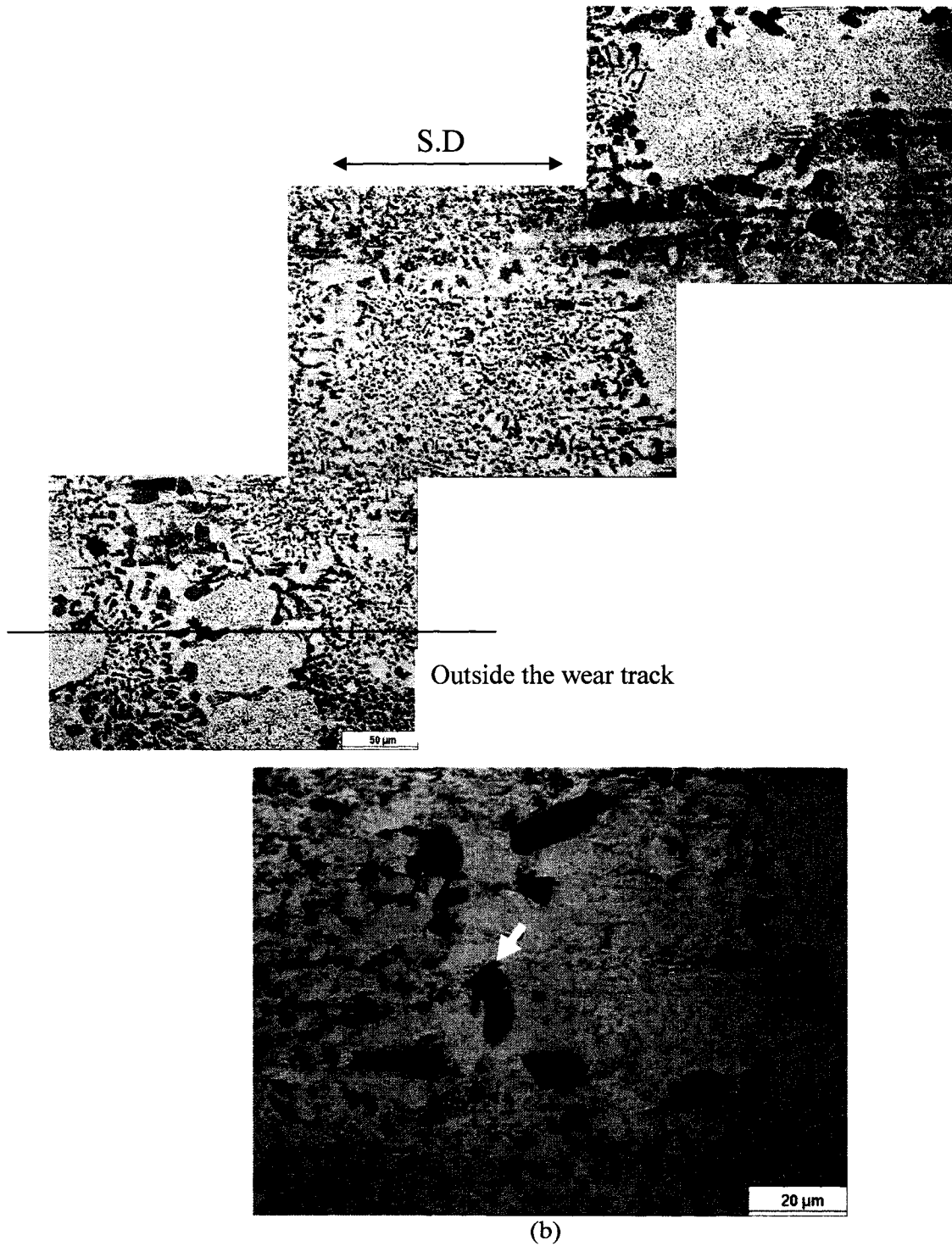
(b)

Figure 4.55 Topographies of worn surface of A13-C-T6 after 2.16Km reciprocating wear at 0.72m/s velocity, 150 °C. (a) x 500, (b) x 1000. The arrow showed the grooved Si particle.

146

(a)
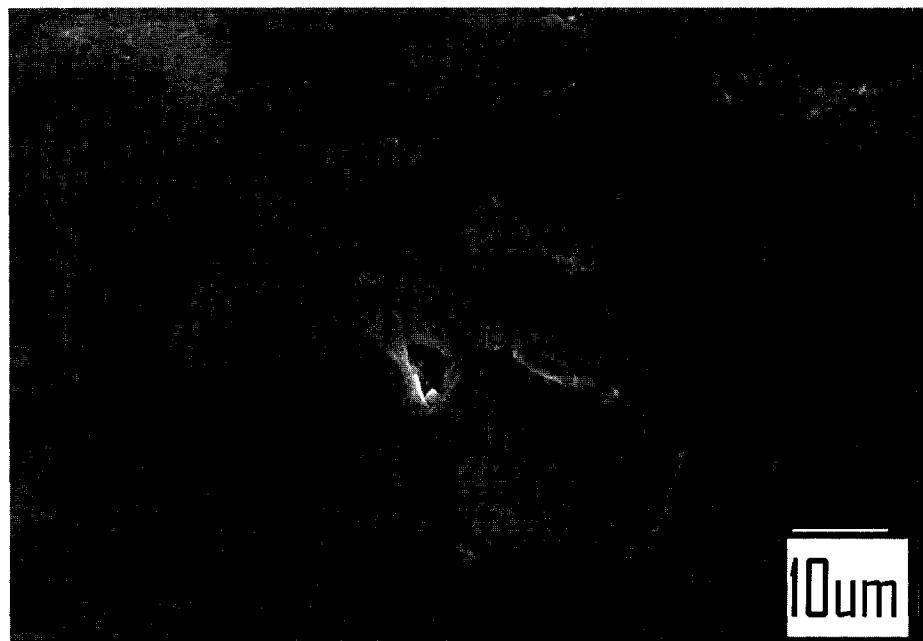
(b)

Figure 4.56 SEM morphology of worn surfaces. (a) The needle-shaped Si particles in A13-S are fractured and grinded; (b) The round-shaped Si particles in A13-C-T6 underwent minimal damage with aluminum smeared over the surfaces.

147
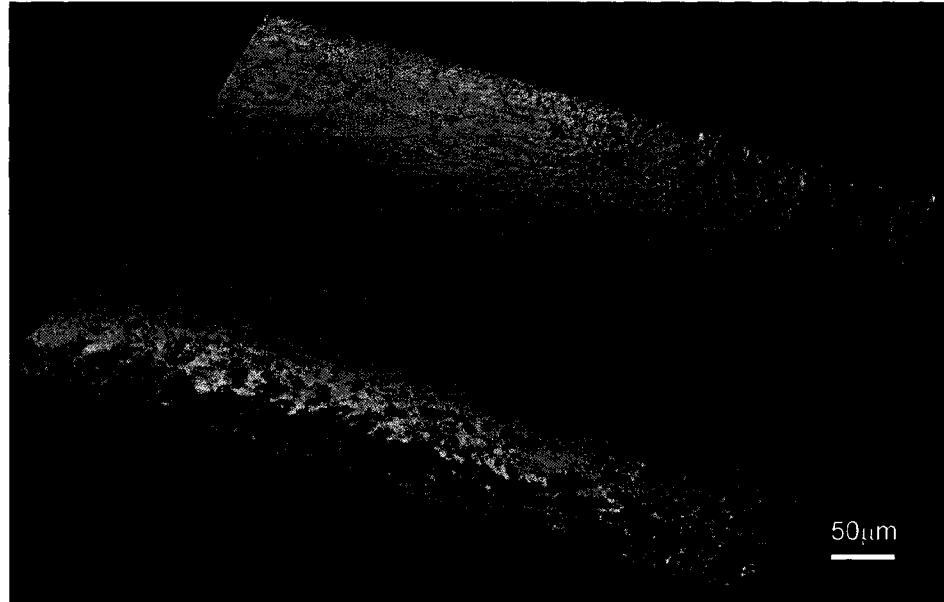
(a)
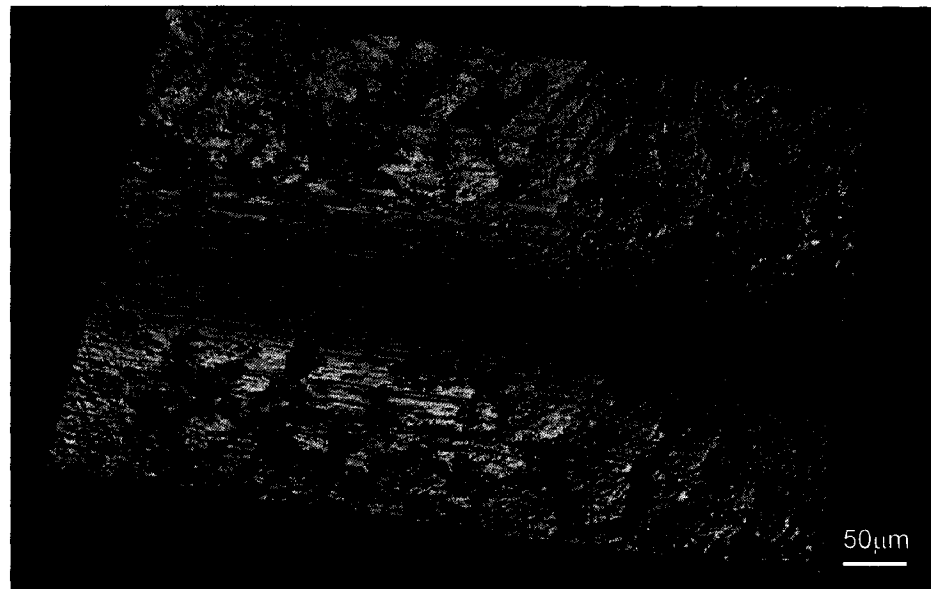
(b)

Figure 4.57 WYKO 3D images of scratch tracks. (a) A13-S, (b) A13-C-T6 after 2.16km wear test at 0.72m/s, 150 °C, lubricated condition.

148
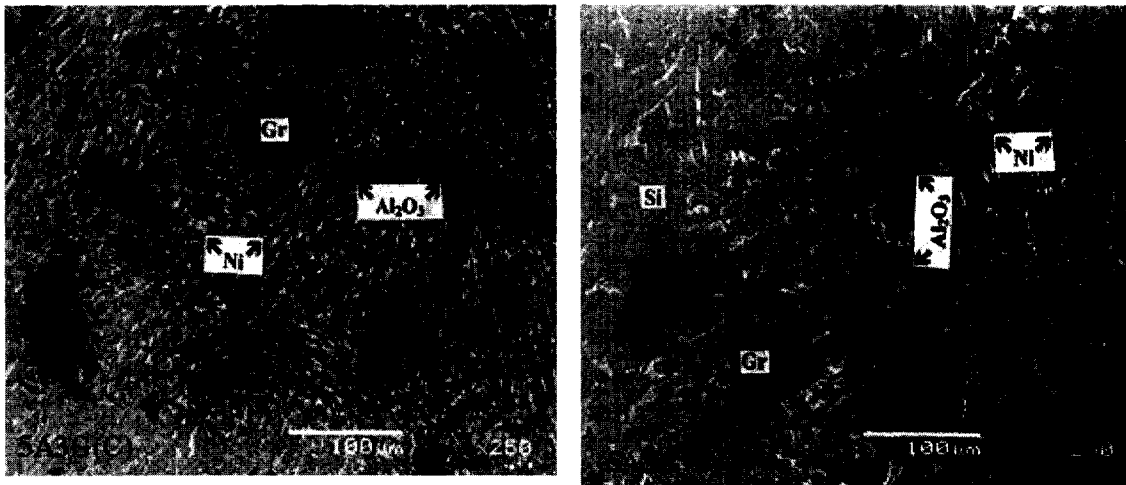
(a)

(b)
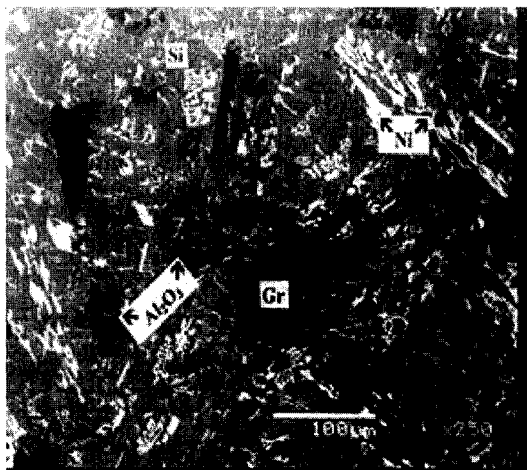
(c)
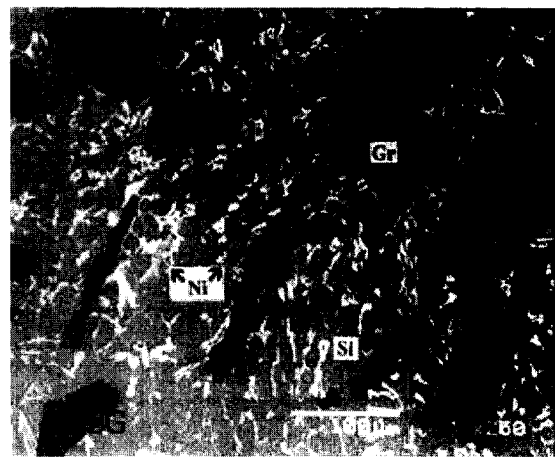
(d)
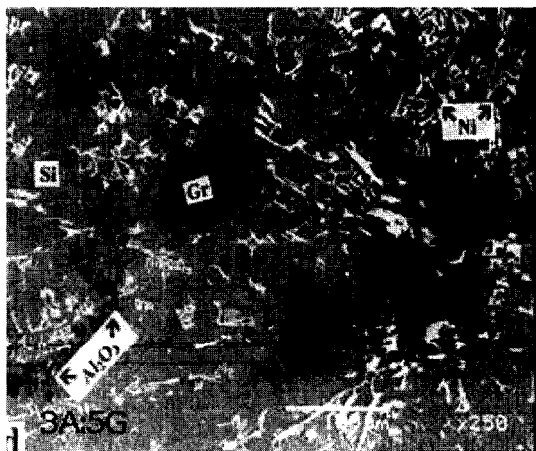
(c)
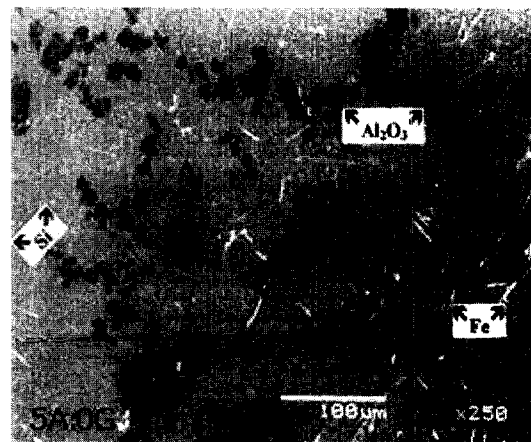
(d)

Figure 5.1 Microstructures of the Al-Si based composite materials

149
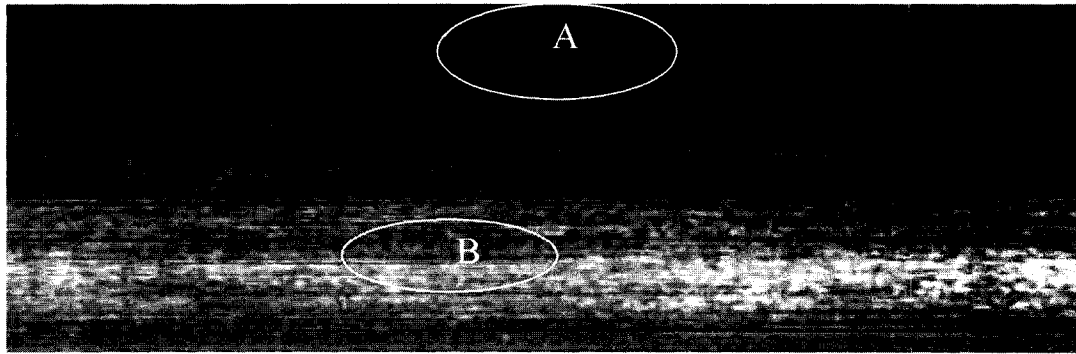
Figure 5.2 Topography of 5A3G (C) worn surface in low magnification (x3), 350N.
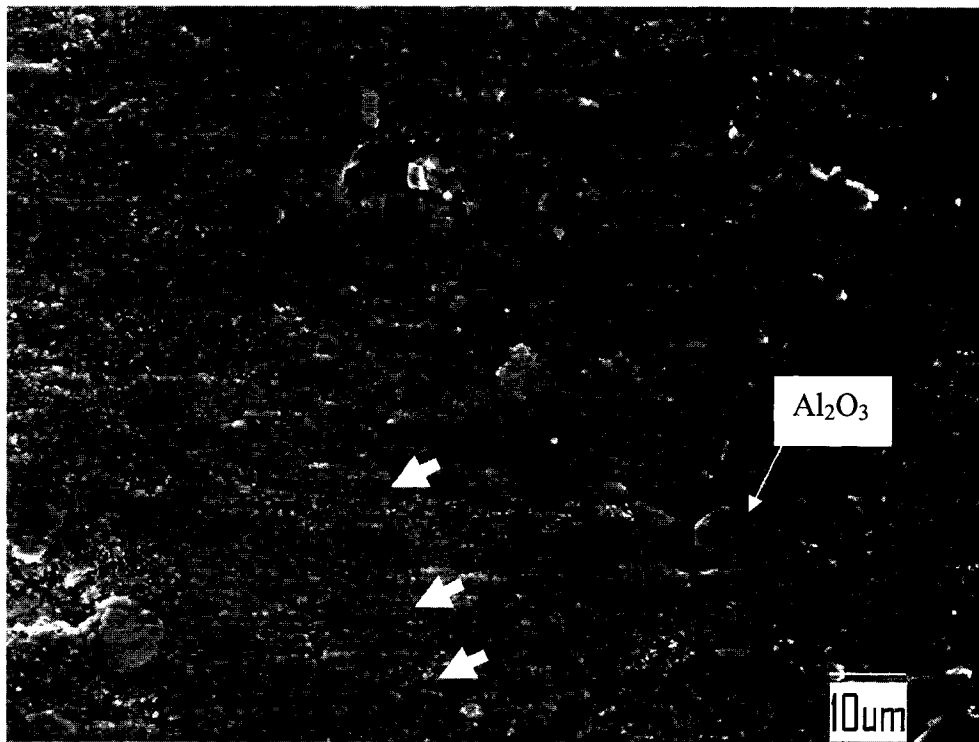
Figure 5.3 Topography of 5A3G(C) in high magnification from A in Figure 5.2 (350N). Arrows showed the deformation zone in the dark area marked A.

150
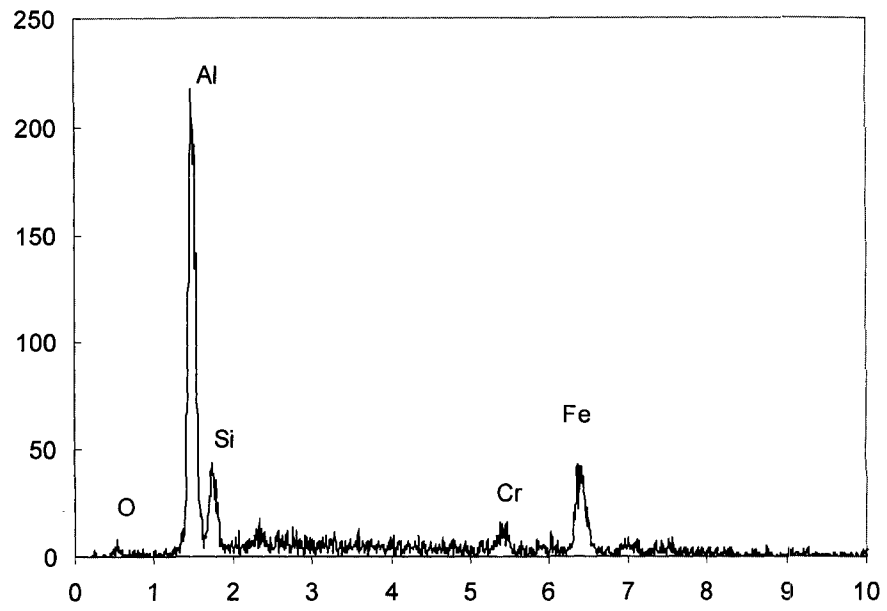
Figure 5.4 EDS from the 5A3G (C) worn surface.

151
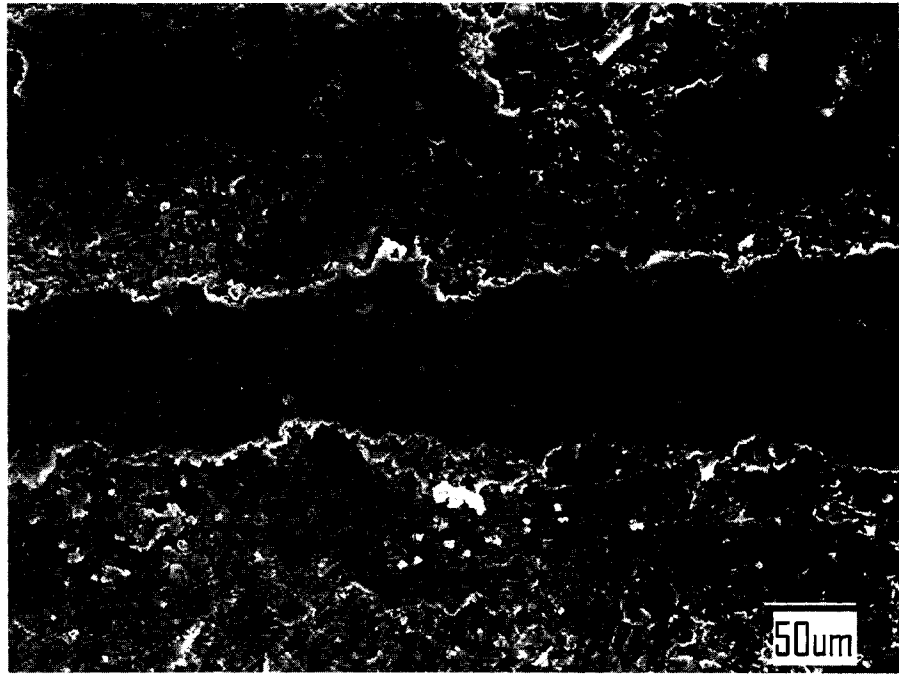
Figure 5.5 Compacted smeared layer from A in Figure 5.2 (350N)

152
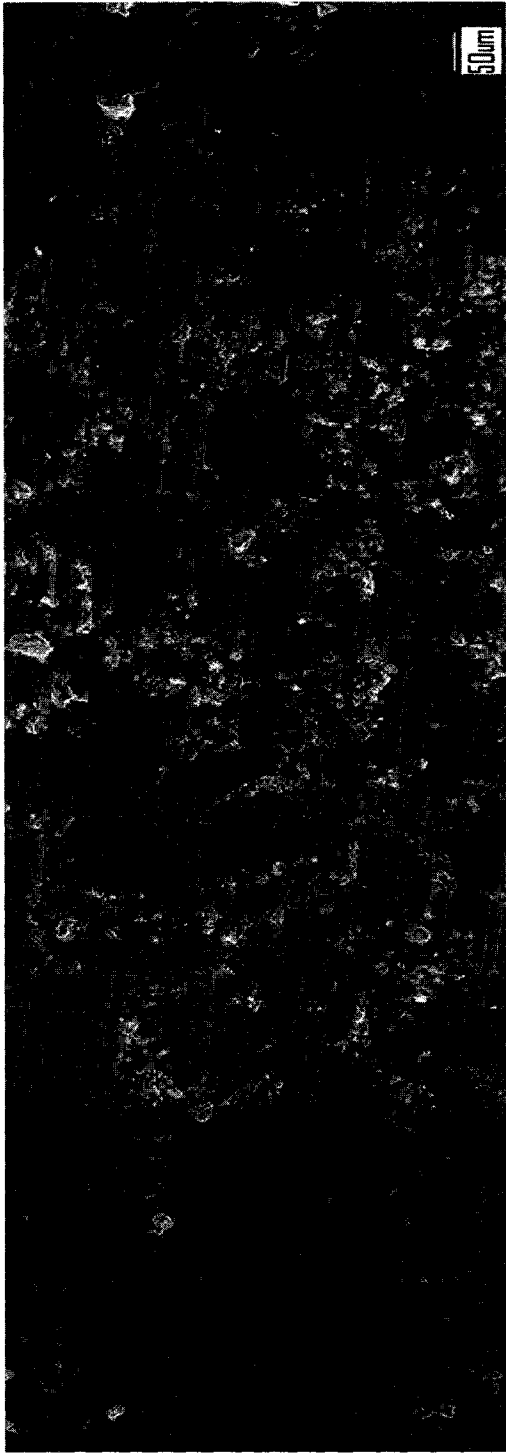
Figure 5.6 High magnification topography of B in Figure 5.2 (350N)

153
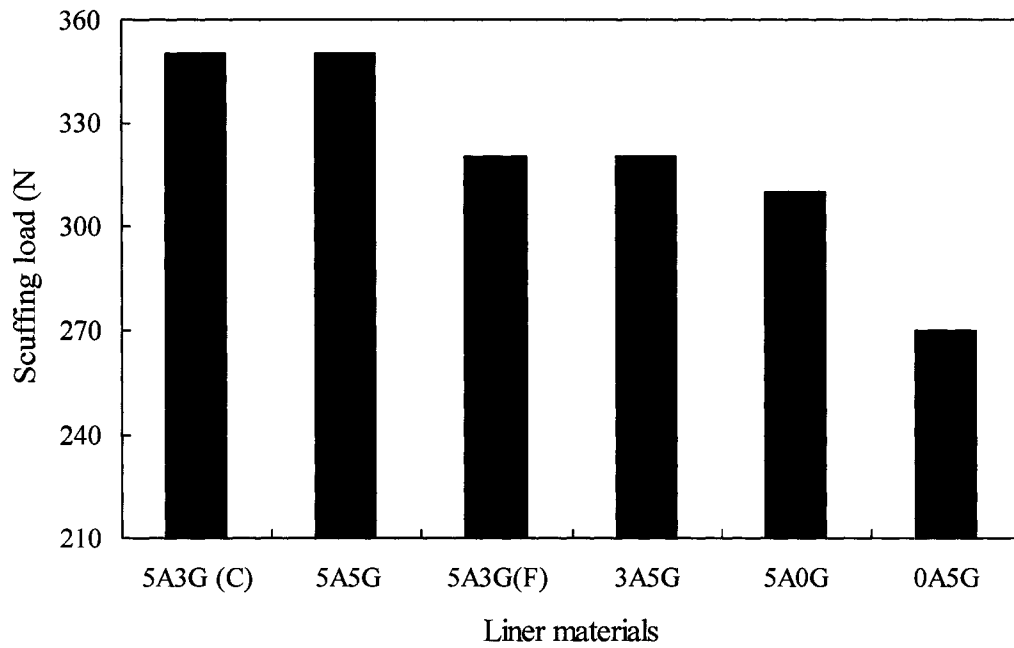
Figure 5.7. Scuffing loads of Al-Si composites
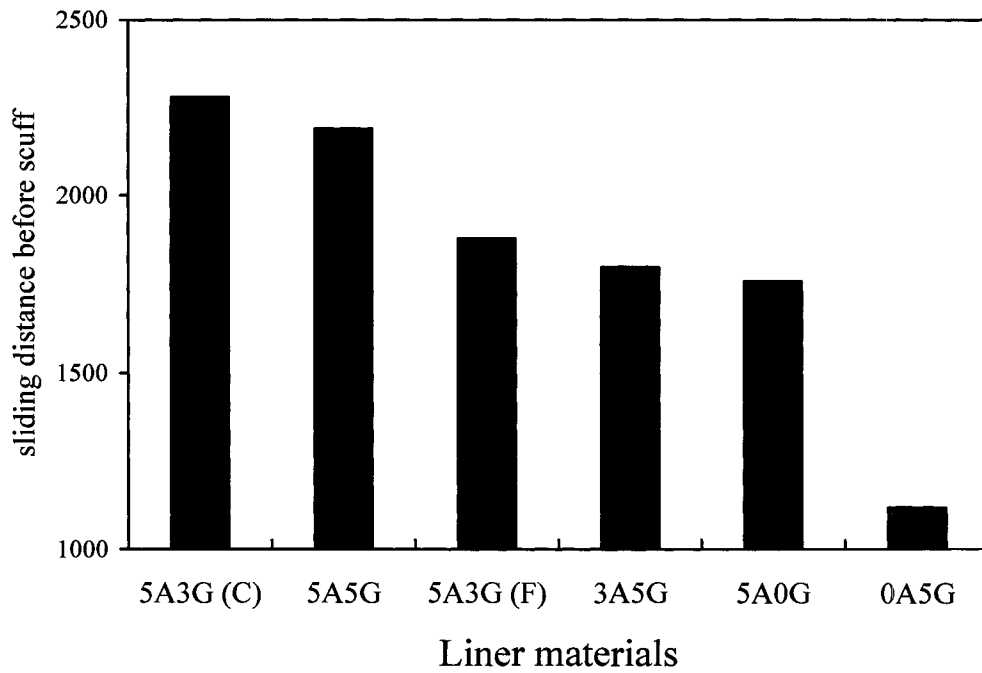
Figure 5.8 Scuff sliding distances at the scuffing loads shown in Figure 5.7.

154
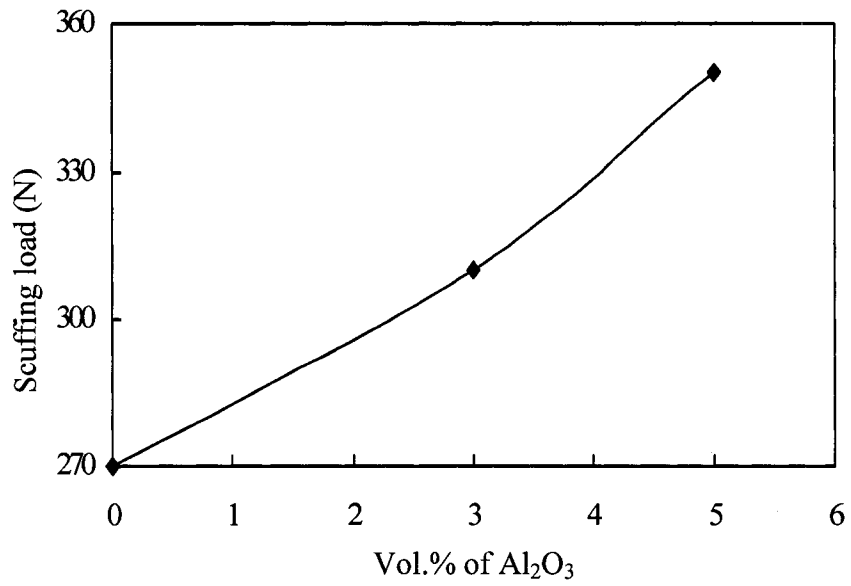
Figure 5.9 Correlation of scuffing load and vol.% of Al2O3.
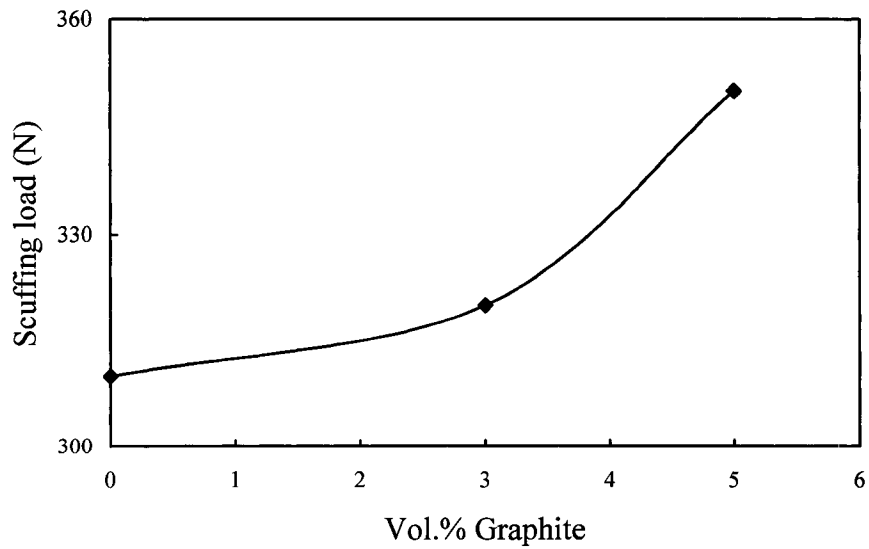
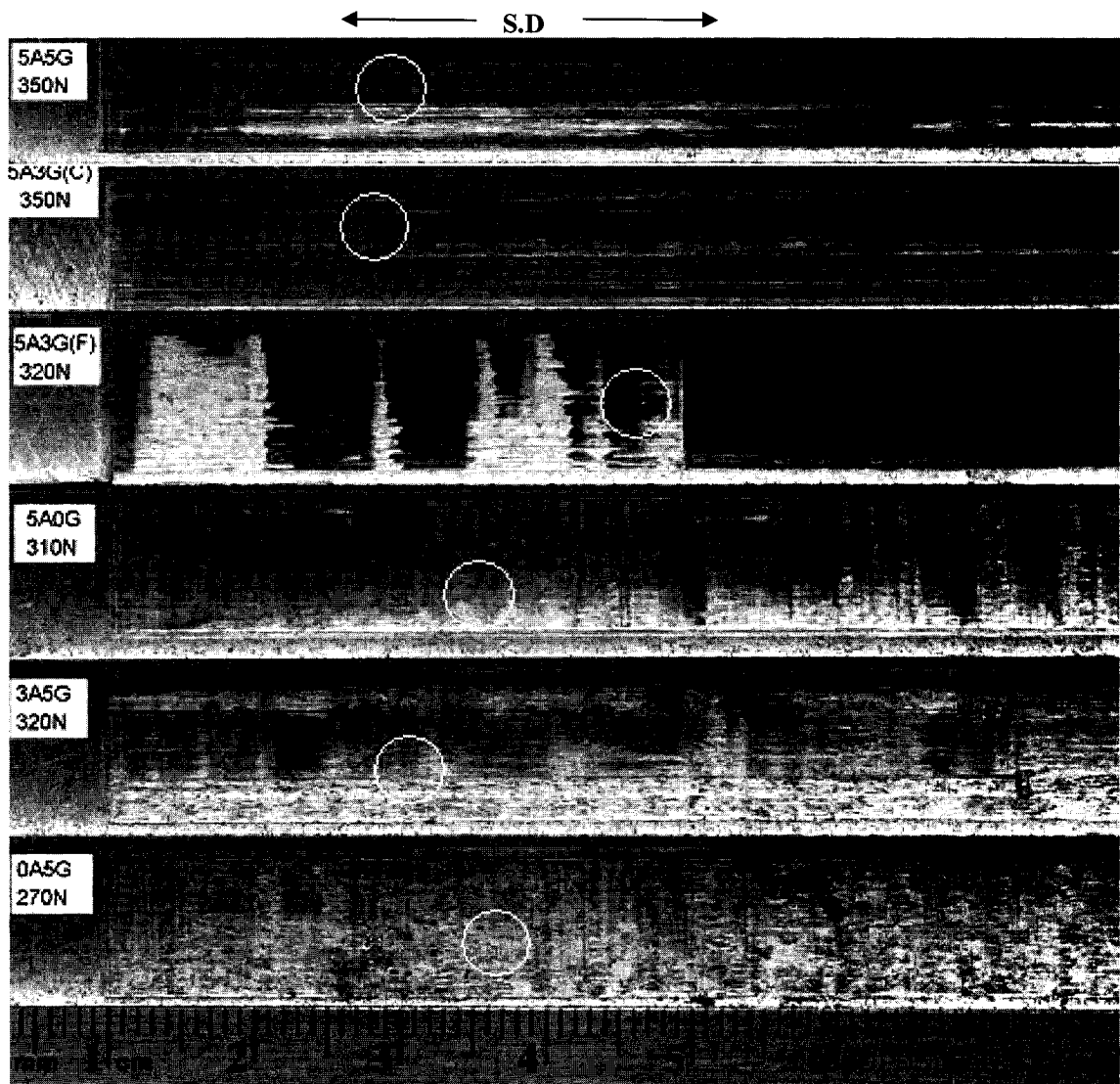Figure 5.10 Correlation of scuffing load and vol.% of Graphite in the composites.

155

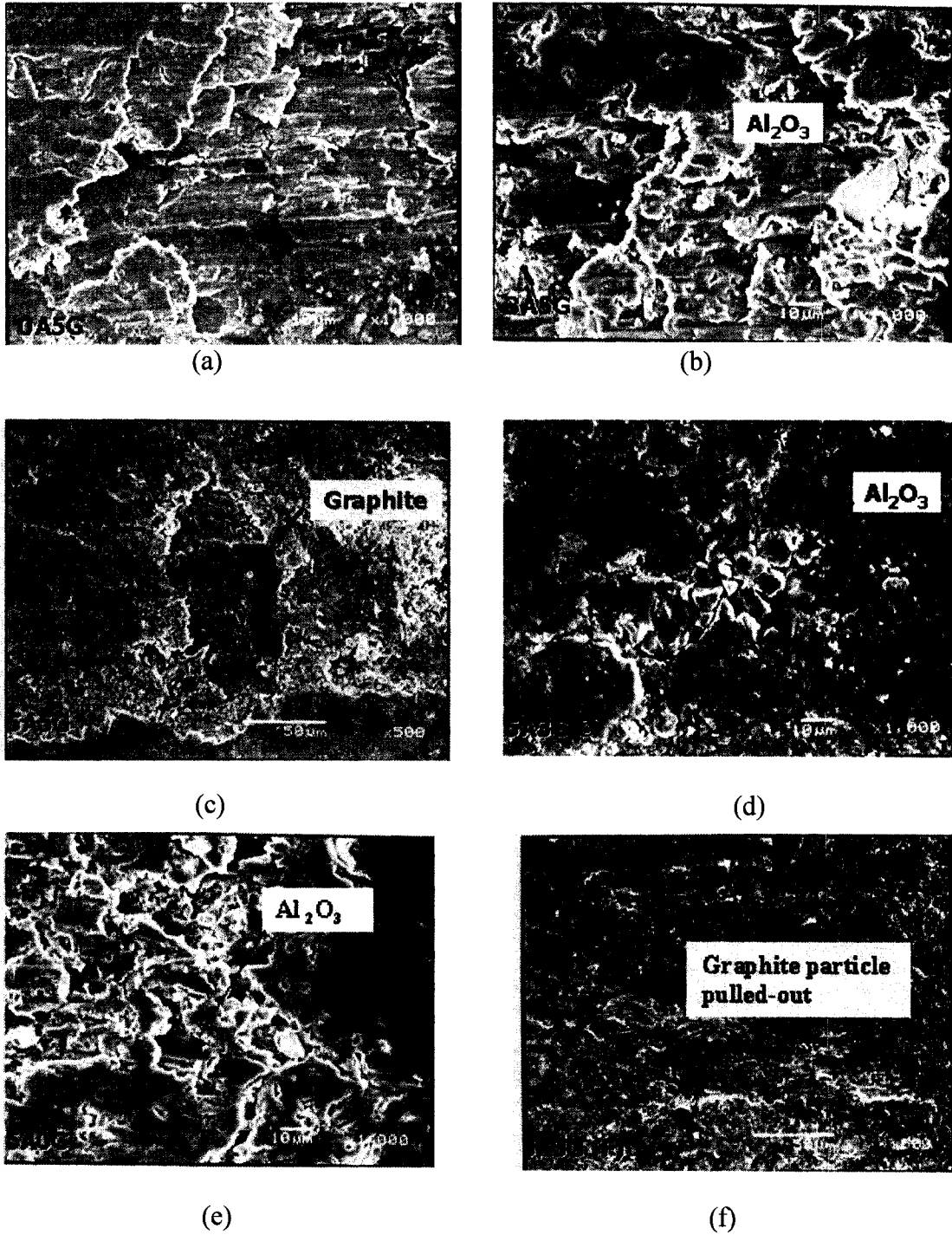Figure 5.11 Surface topographies of A356 Al-graphite composites scuffed at the corresponding scuffing load and 0.72m/s sliding speed.

156

(a)   (b)

(c)   (d)

(e)   (f)

Figure 5.12 SEM surface morphologies of A356 Al-graphite composite after-scuffed surface (from the circle areas in Fig.5.10).
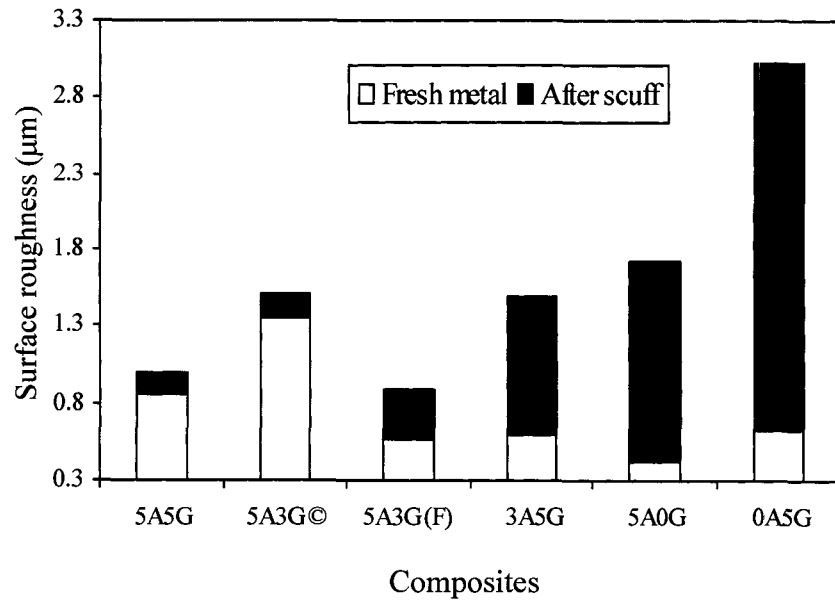
157

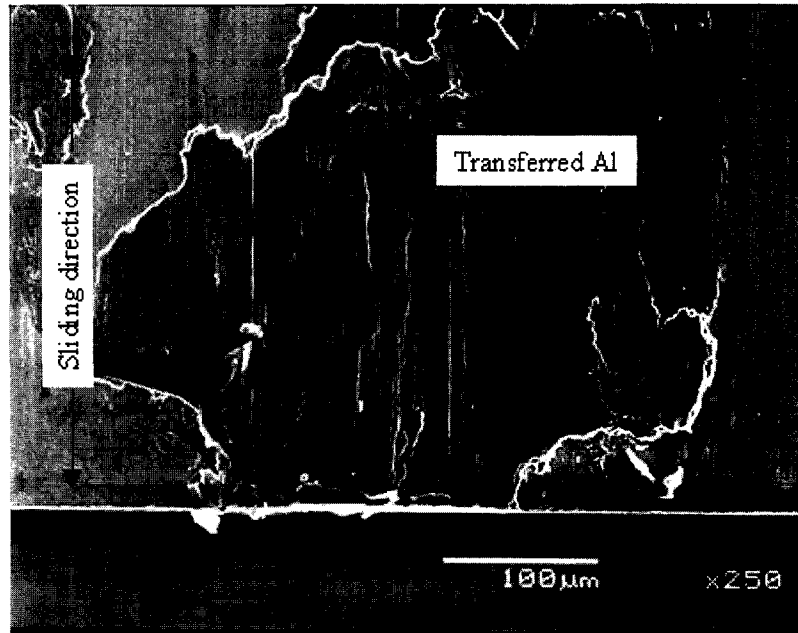Figure 5.13 Surface roughness of fresh samples and scuffed samples.

158

Figure 5.14 Al transferred to the ring surface against the 5A5G after scuffing.
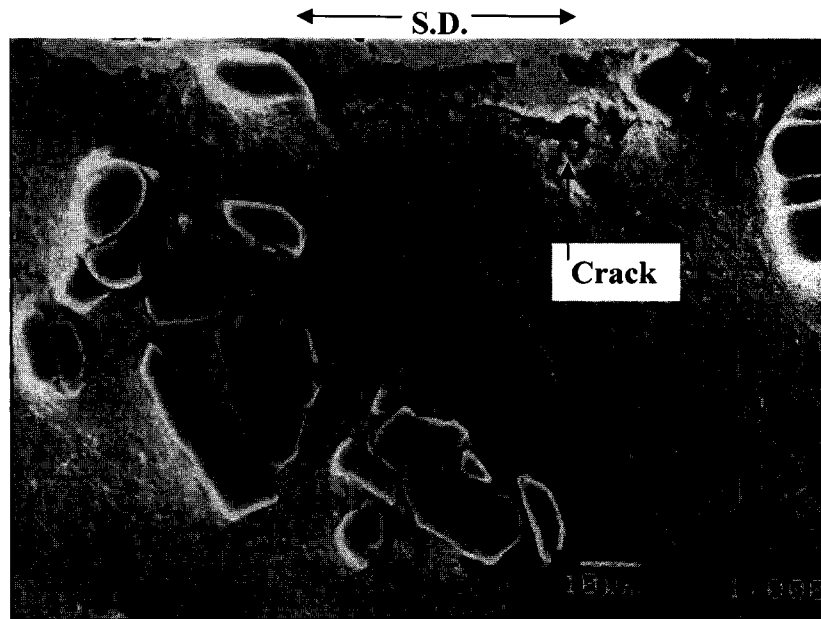
159

Figure 5.15 Cross section of worn surface: crack under 5A3G (C) scuffed surface.
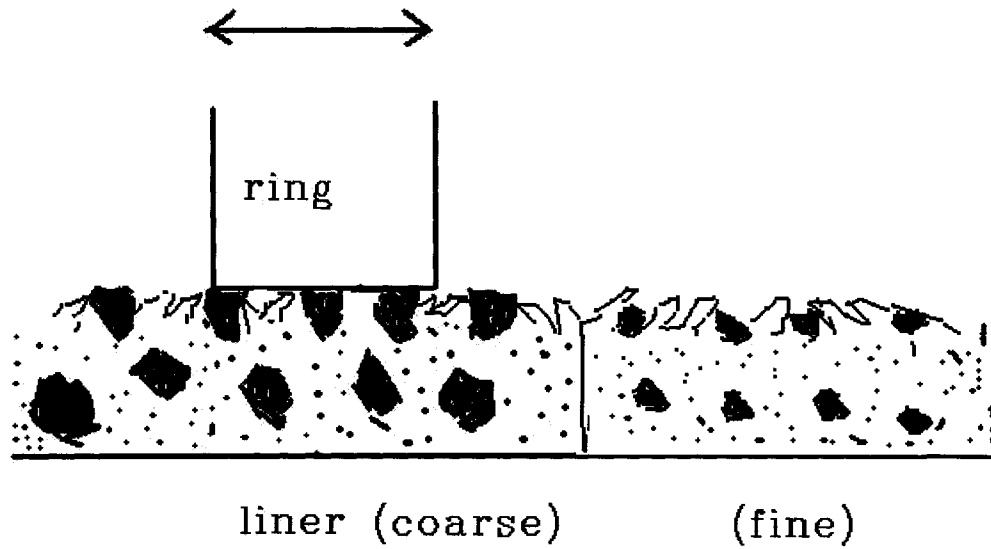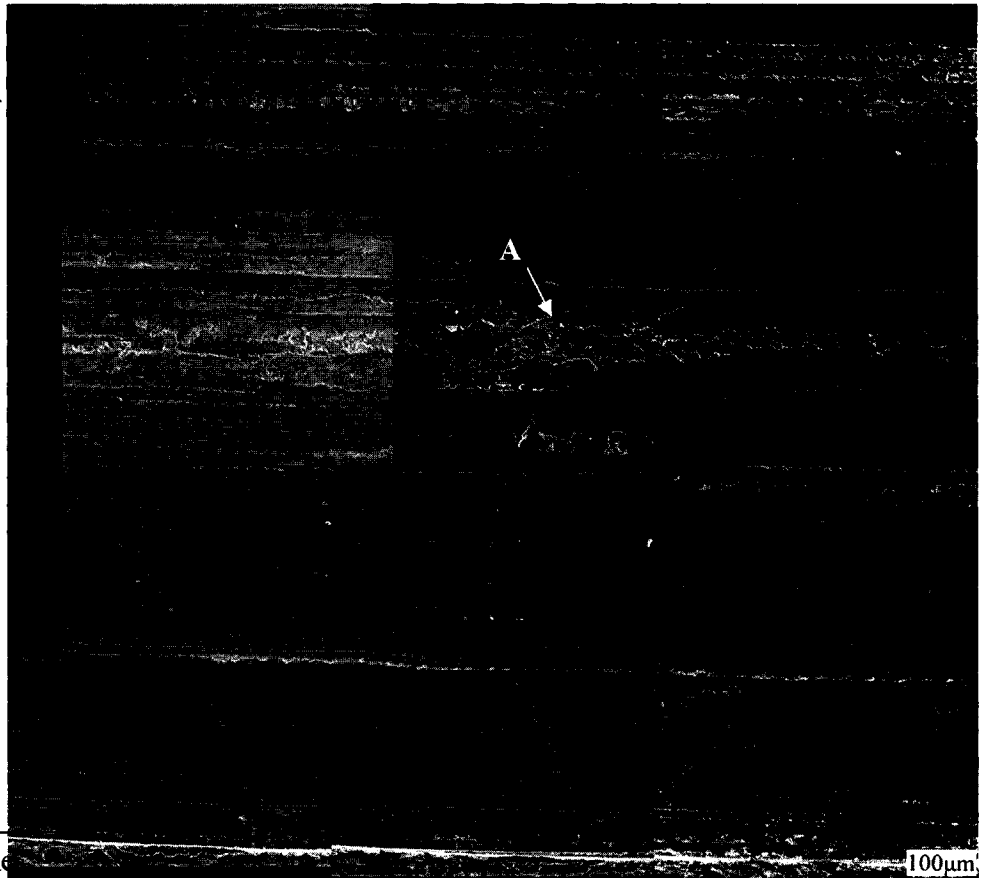
Figure 5.16 Illustration of influence of particle size on scuffing.

Outside the
worn track

Outside the
track

Figure 5.17 Scuffed surface of A13-S specimen. Area marked A shows aluminum plastic deformation and smearing on the surface, which indicates welding occurred between the counterface and the specimen.
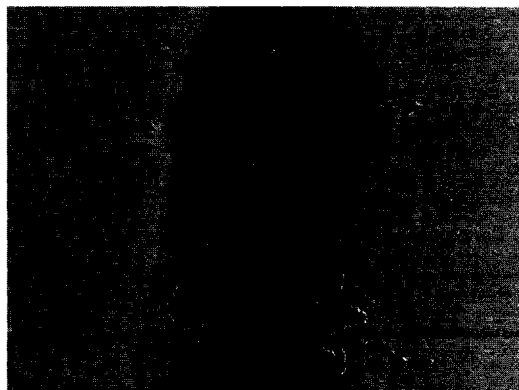

Figure 5.18 M2 counterface against the A13-S specimen (x100). Large amount of transferred aluminum was welded on the top of the counterface area.

162

Figure 5.19 Scuffed surface of the A13-C-T6 specimen. Area marked A shows deep galling occurred on the surface.

Figure 5.20 Worn surface of the M2 counterface against A13-C-T6 specimen (x100). Small amount of transferred aluminum and debris attached on the scuffed counterface.

163

VITA AUCTORIS

Hongbo Wang was born in 1967 in Liaoning, China. He graduated from Yingkou High School in 1987. Then he went on to the Northeastern University in China. After the graduation he worked 8 years as a metallurgical engineer. He is currently a candidate for the Master's degree in Engineering Materials at the University of Windsor and hopes to graduate in summer 2005.